Tampere University

Rosanna Silén

NANOHYDROXYAPATITE-SUPPLEMENTED METHACRYLATED GELATIN BIOINKS FOR THREE-DIMENSIONAL BIOPRINTING OF BONE

Faculty of Medicine and Health
Technology
Master's Thesis
October 2021

ABSTRACT

Rosanna Silén: Nanohydroxyapatite-supplemented methacrylated gelatin bioinks for three-dimensional bioprinting of bone
Master's Thesis
Tampere University
Master's Programme in Biomedical Technology
Supervisors: Professor Susanna Miettinen, Postdoctoral Fellow Ahmad Rashad Saad Mohamed Elsebahy, and MSc, PhD Candidate Jannika Paulamäki
Examiners: Professor Susanna Miettinen and Professor Heli Skottman
October 2021

Background and aims of the study: Bones have a regeneration capacity to a certain point, but critical-sized bone defects require treatment to heal the tissue. The increasing incidence of bone defects in the world has led to the need of more effective treatment strategies. Traditional treatment methods for bone defects are grafts or synthetic materials, but various limitations are related to their use. For instance, with grafts, high costs, risk for infections, and minor availability are issues related to their use. Tissue engineering focuses on approaches to replace or recover biological tissue. However, in the field of bone tissue engineering (BTE), the available artificial scaffolds do not mimic the natural bone and they usually have nonordered distribution of cells. Three-dimensional (3D) bioprinting is seen as a potential new solution in BTE to create personalized, organized, and bone-like constructs. However, lack of ideal bioinks is a considerable issue in 3D bioprinting, as various requirements related to cell function and printability of the bioinks exist. In this thesis, the aim was to develop a multicomponent bioink for extrusion-based 3D bioprinting for bone applications and to investigate the effect of nanohydroxyapatite (nHA) on printability and biological performance of the bioink. Great part of a natural bone tissue consists of nHA.

Materials and methods: The nHA concentrations in the bioinks were 0.0, 1.0, 3.0, and 5.0 % (weight/volume). First, the biomaterial inks, printing conditions, and ultraviolet (UV) light induced crosslinking were optimized by conducting a casting pilot and 3D printing pilots. The biomaterial inks were characterized for their material properties in terms of rheology, stability, and printability. Biological characterization composed of 3D bioprinting pilot, where human bone marrow derived mesenchymal stem cells (hBMSCs) were bioprinted in one bioink to optimize the crosslinking conditions in terms of cell viability and proliferation. After that, bioinks with different concentrations of nHA were 3D bioprinted and the viability, proliferation, morphology, and osteogenic differentiation of hBMSCs were examined with live/dead staining, proliferation assay, and immunostainings. Cytotoxicity of the materials and bioprinting process was evaluated by examining lactate dehydrogenase production by cells.

Results and conclusions: Longer UV exposure times tested in crosslinking decreased the cell viability and with all tested UV exposure times, the cell viability was decreased in first printed layers of the constructs. However, 45 second UV exposure time for each printed layer was found to be most functional and having minimal negative impact for the cells. In case of the bioink with 1 % nHA, enhanced cell viability and proliferation of hBMSCs was observed when compared to the other bioinks. This group had also excellent properties in terms of rheology, printability, and stability. Additionally, the bioink with 5 % nHA was found to have higher viscosity than with other bioinks, which had a negative impact on printability and biological responses of hBMSCs. Further studies are required, as, from made immunostainings, it was not possible to verify osteogenic differentiation of hBMSCs. In the future, the developed bioink with 1 % nHA together with UV crosslinking can potentially be used in 3D bioprinting for bone applications.

Keywords: bone, bone tissue engineering, human mesenchymal stem cell, 3D bioprinting, bioink, nanohydroxyapatite

TIIVISTELMÄ

Rosanna Silén: Nanohydroksiapatiitti-täydennetyt metakryloitu gelatiini -biomusteet luun kolmiulotteiseen biotulostukseen
Pro Gradu -tutkielma
Tampereen yliopisto
Biolääketieteen tekniikan maisteriohjelma
Ohjaajat: Professori Susanna Miettinen, tutkijatohtori Ahmad Rashad Saad Mohamed Elsebahy ja maisteri, tutkijatohtori kandidaatti Jannika Paulamäki
Tarkastajat: Professori Heli Skottman ja professori Susanna Miettinen
Lokakuu 2021

Tutkimuksen tausta ja tavoitteet: Luut pystyvät uusiutumaan tiettyyn pisteeseen asti, mutta suuremmat luuvammat vaativat hoitoa kudoksen parantamiseksi. Luuvammojen lisääntynyt määrä maailmassa on johtanut tehokkaampien hoitomenetelmien tarpeeseen. Luusiirteet tai synteettiset materiaalit ovat perinteisiä hoitomenetelmiä luuvammoihin, mutta niiden käyttöön liittyy monia rajoituksia. Esimerkiksi luusiirteisiin liittyvät kustannukset, infektioriski ja heikko saatavuus ovat ongelmallisia. Kudosteknologia keskittyy lähestymistapoihin, jotka tähtäävät korvaamaan tai palauttamaan biologisen kudoksen. Luukudosteknologian alalla saatavilla olevat keinotekoiset skaffoldit eivät kuitenkaan vastaa luonnollista luuta, ja solujen jakautuminen niissä on tavallisesti järjestäytymätöntä. Kolmiulotteinen (3D) biotulostus nähdään lupaavana uutena ratkaisuna luukudosteknologiassa luoda yksilöllisiä, järjestäytyneitä ja luukudosta vastaavia rakenteita. Optimaalisten biomusteiden puute on kuitenkin suuri haaste 3D-biotulostuksessa, koska solujen toimintaan ja biomusteiden tulostettavuuteen liittyy monenlaisia vaatimuksia. Tässä opinnäytetyössä tavoitteena oli kehittää monikomponenttinen biomuste ekstruusioon perustuvalle 3D-biotulostukselle luusovelluksiin ja tutkia nanohydroksiapatiitin (nHA) vaikutusta biomusteen tulostettavuuteen ja biologiseen toimivuuteen. Suuri osa luonnollisesta luukudoksesta koostuu nanohydroksiapatiitista.

Materiaalit ja menetelmät: Biomusteiden nHA-pitoisuudet olivat 0.0, 1.0, 3.0 ja 5.0 % (paino/tilavuus). Ensiksi biomateriaalimusteet, tulostusolosuhteet ja materiaalin ristisilloittaminen ultravioletti (UV) -valolla optimoitiin tekemällä valantakokeilu ja 3D-tulostuspilotit. Biomateriaalimusteet karakterisoitiin keskittyen musteiden reologiaan, stabiilisuuteen ja tulostettavuuden. Biologisessa karakterisoinnissa, joka koostui 3D-biotulostuspilotista, ihmisen luuytimestä peräisin olevat mesenkymaaliset kantasolut biotulostettiin yhdessä biomusteista, ristisilloitusolosuhteiden optimoimiseksi solujen elinkelpoisuuden ja lisääntymisen kannalta. Sen jälkeen biomusteet eri nHA-pitoisuuksilla 3D-biotulostettiin ja solujen elinkelpoisuutta, jakaantumista, morfologiaa ja erilaistumista tutkittiin elävyys/kuolleisuus analyysilla, solujen jakaantumismäärityksellä ja immunofluoresenssivärjäyksillä. Materiaalien ja biotulostusprosessin sytotoksisuus arvioitiin tutkimalla solujen laktaattidehydrogenaasi-tuotantoa.

Tulokset ja johtopäätökset: Ristisilloituksessa testatut pidemmät UV-altistumisajat heikensivät solujen elinkelpoisuutta ja kaikilla testatuilla altistumisajoilla solujen elinkelpoisuus oli alhaisempi rakenteiden ensimmäiseksi tulostetuissa kerroksissa. Kuitenkin 45 sekunnin UV-altistumisaika kullekin tulostetulle kerrokselle osoittautui toimivimmaksi ja vaikutti mahdollisimman vähän soluihin. Biomusteessa, jossa nHA pitoisuus oli 1 %, solujen elinkyky ja jakaantuminen oli parempi verrattuna muihin biomusteisiin. Tällä ryhmällä oli myös erinomaiset ominaisuudet reologian, tulostettavuuden ja stabiilisuuden suhteen. Lisäksi 5 % nHA biomusteen viskositeetin todettiin olevan korkeampi kuin muissa biomusteissa, mikä vaikutti negatiivisesti musteen tulostettavuuteen ja solujen biologisiin vasteisiin. Lisätutkimuksia tarvitaan, koska tehdyistä immunofluoresenssivärjäyksistä ei ollut mahdollista todeta solujen erilaistumista. Kehitettyä 1 % nHA biomustetta ja UV-ristisilloitusta voidaan mahdollisesti tulevaisuudessa hyödyntää luusovelluksiin tähtäävässä 3D-biotulostuksessa.

Avainsanat: luu, luun kudosteknologia, ihmisen mesenkymaalinen kantasolu, 3D-biotulostus, biomuste, nanohydroksiapatiitti

PREFACE

This Master's Thesis was done in the Adult Stem Cell group at the Faculty of Medicine and Health Technology at Tampere University. First, I would like to thank the group leader and my supervisor Professor Susanna Miettinen, for giving me this opportunity to work with such a fascinating subject handling 3D bioprinting and tissue engineering. I would also like to thank all my supervisors, Professor Susanna Miettinen, MSc Jannika Paulamäki, and Postdoctoral Fellow Ahmad Rashad Saad Mohamed Elsebahy, for giving guidance and excellent supervision throughout the thesis project. Special thanks to Jannika, who familiarized me to the field of 3D bioprinting for bone tissue applications and has been always available for questions throughout the project. Furthermore, I would like to thank all other group members of the Adult Stem Cell group for support and advice.

Finally, I would like to thank my family and friends, who have supported me during this project and always throughout my studies. Miikka deserves special thanks, as he has been constant support for me and made this project much easier.

Tampere, October 2021

Rosanna Silén

CONTENTS

LIST OF TABLES

LIST OF FIGURES

LIST OF SYMBOLS AND ABBREVIATIONS

2D	Two-dimensional
3D	Three-dimensional
BaG	Bioactive glass
BCA	Bicinchoninic acid
BM	Basic medium
BPL	Bordland Package Library
BSA	Bovine serum albumin
BTE	Bone tissue engineering
Calcein-AM	Calcein acetoxymethyl
CCK-8	Cell Counting Kit-8
Cell stack	2-chamber CellSTACK® culture chamber
CNFs	Cellulose nanofibers
CT	Computed tomography
DAPI	4′,6-Diamidino-2-phenylindole dihydrochloride
DLP	Digital light processing
DNA	Deoxyribonucleic acid
DOD	Drop-on-demand
DPBS	Distilled phosphate-buffered saline
ECM	Extracellular matrix
EthD-1	Ethidium homodimer-1
GelMA	Gelatin methacryloyl
GelNB	Gelatin−norbornene
hBMSCs	Human bone marrow derived mesenchymal stem cells
hFGF-2	Human fibroblast growth factor 2
hMSCs	Human mesenchymal stem cells
HS	Human serum
IC	2-Hydroxy-4'-(2-hydroxyethoxy)-2-methylpropiophenone, Irgacure 2959
iPSCs	Induced pluripotent stem cells
LAP	Lithium phenyl-2,4,6-trimethylbenzoylphosphinate
LDH	Lactate dehydrogenase
LIFT	Laser-induced forward transfer
NDS	Normal donkey serum
nHA	Nanohydroxyapatite
OM	Osteogenic medium

P	Passage
PEG	Polyethylene glycol
PEGDA	Polyethylene glycol diacrylate
PEGDMA	Poly(ethylene glycol)dimethacrylate
PFA	Paraformaldehyde
Phalloidin-TRITC	Phalloidin–tetramethylrhodamine B isothiocyanate
P/S	Penicillin-streptomycin
qPCR	Quantitative polymerase chain reaction
RT	Room temperature
Ru	Tris(2,2- bipyridyl) dichlororuthenium (II) hexahydrate
RUNX2	Runt-related transcription factor 2
SLA	Stereolithography
SPS	Sodium persulfate
TE	Tissue engineering
TEMPO	2,2,6,6-tetramethylpiperidine-1-oxyl
T 175 flask	Cell culture T175 cm^2 flask
UV	Ultraviolet
VEGF	Vascular endothelial growth factor
w/v	Weight by volume
αMEM	Alpha minimum essential medium

1. INTRODUCTION

Bones form the main part of the human skeletal system and have various essential functions, such as structural supporting, protection of organs, and production of blood cells (Qu et al., 2019; Tozzi et al., 2016; Pawlina and Ross 2016). Bone tissue has hierarchical structural organisation and multiple cell types, which are mainly derived from human mesenchymal stem cells (hMSCs). Human MSCs are multipotent adult stem cells located mainly in the bone marrow (Tozzi et al., 2016). Main part of the bone tissue consists of mineralized extracellular matrix (ECM), secreted by cells, and formed from hydroxyapatite, providing hardness of bone (Pawlina and Ross 2016). The incidence of bone defects, like bone diseases and traumas, is continuously increasing, which increases the need for effective treatment strategies (Pawlina and Ross 2016; Warriner et al., 2011; Office of the Surgeon General (US), 2004). Traditional way to treat bone defects are bone autografts and allografts taken from the donor site and moved to the injury site of a patient. Grafts are usually biocompatible, osteoconductive, and osteoinductive but various challenges such as high costs, risk for infections, minor availability, secondary damages, morbidity in donor site, and limited possibilities to obtain certain shape and sufficient volume are related to their use. (Qu et al., 2019; Tozzi et al., 2016; Amini et al., 2012) Synthetic materials, for instance inert metals, ceramics, and some polymers, are also used to treat bone defects but certain limitations are also related to their use (Sheikh et al., 2017; Tozzi et al., 2016; Basha et al., 2015).

Tissue engineering (TE) refers to versatile approaches, which focus on regeneration of tissues (Qu *et al.*, 2019). Bone tissue engineering (BTE) is seen as a promising way to solve the problems related to the traditional treatments of bone defects (Midha et al., 2019; Tozzi et al., 2016; Amini et al., 2012). In BTE, scaffolds, with ECM mimicking three-dimensional (3D) environment, are used to deliver cells and/or growth factors to treat bone defects (Qu et al., 2019). Still, the available engineered bone scaffolds do not completely mimic the hierarchical anatomy of natural bone. In addition, establishment of the vasculature and the communication between different cell types in the constructs is lacking. (Midha et al., 2019; Leberfinger et al., 2017) 3D bioprinting is seen as a potential new solution in BTE to create personalized, organized, and biomimetic large constructs with high precision, vascularization, and desired porosity (Vijayavenkataraman et al., 2018; Jungst et al., 2016). In 3D bioprinting, 3D structures are fabricated layer-by-layer by placing cells, with or without ECM mimicking biomaterials, using a computer-controlled dispensing system (O'Connell et al., 2018; Dababneh and Ozbolat 2014). Printable materials or formulations consisting of cells with or without biomaterials are called bioinks (Groll et al., 2019).

The aim of this thesis was to develop a multicomponent bioink for extrusion-based 3D bioprinting and to evaluate the effect of different concentrations of nanohydroxyapatite (nHA) particles on the printability and biological properties of the developed bioink. It was hypothesized that high concentration of nHA will increase the viscosity of the bioink, which may cause high shear stress on cells while 3D bioprinting, causing decreased cell viability. On the other hand, the increased concentration of nHA was expected to induce osteogenic differentiation of human bone marrow-derived mesenchymal stem cells (hBMSCs), as nHA is osteoconductive and a natural component of the bone. The nHA concentrations were chosen to be 1.0, 3.0, and 5.0 % w/v (weight by volume). Additionally, the biological responses of hBMSCs embedded in the developed bioinks were investigated. The base components for the bioinks were gelatin methacryloyl (GelMA), gelatin, and wood-derived cellulose nanofibers (CNFs). Light induced crosslinking with ultraviolet (UV) light and the photoinitiator 2-Hydroxy-4'-(2-hydroxyethoxy)-2-methylpropiophenone, known as Irgacure 2959 (IC), was used for crosslinking.

The project began by optimizing the base components and the mixing protocol of the biomaterial inks by conducting a casting pilot and 3D printing pilots with the biomaterial inks. Optimization of the printing conditions and crosslinking was also done simultaneously. Material characterizations in terms of rheological properties, stability, and printability of the biomaterial inks were conducted. Next, biological characterization was executed. It composed of a 3D bioprinting pilot, where hBMSCs were bioprinted in one bioink to optimize the crosslinking conditions in terms of cell viability and proliferation. After the 3D bioprinting pilot, bioinks with different concentrations of nHA were 3D bioprinted and the viability, proliferation, morphology, and osteogenic differentiation of the hBMSCs were examined with live/dead staining, lactate dehydrogenase (LDH) assay, proliferation assay, and immunostainings.

2. LITERATURE REVIEW

2.1 Human bone tissue

Bones form the main part of the human skeletal system and they have various functions in the body. For instance, bones provide structural and mechanical support, protect organs, and act as a storage site for calcium and phosphate. Blood cells are both produced and hosted in a bone marrow. (Qu *et al.*, 2019; Tozzi *et al.*, 2016; Pawlina and Ross 2016) Bones are formed from connective tissue which consist of cells and mineralized ECM (Pawlina and Ross 2016). The mineralized part of the bone ECM, hydroxyapatite crystals, provide hardness of bone (Pawlina and Ross 2016; Amini *et al.*, 2012). Type 1 collagen and other collagen types are also important structural components providing elasticity and improving mechanical properties of bone (Pawlina and Ross 2016; Amini *et al.*, 2012). The bone ECM also contains other noncollageous proteins like proteoglycan macromolecules, multiadhesive glycoproteins, and bone-specific vitamin K-dependent proteins, such as osteocalcin. Hemopoietic tissue, fat tissue, nerves, and blood vessels are other tissue types found in bone. In joint areas, hyaline cartilage and ligaments are often present and supporting bone function. (Pawlina and Ross 2016)

Bone tissue has multiple cell types which are presented in Figure 1. Bone cells, except osteoclasts are originated from human mesenchymal stem cells (MSCs) (Pawlina and Ross 2016). Human MSCs are multipotent adult stem cells located mainly in the bone marrow but also in other parts of the body, such as in adipose tissue and umbilical cord (Wehrle *et al.*, 2019; Tozzi *et al.*, 2016). Osteoprogenitor cells, derived from MSCs, form periosteum and endosteum together with fibrous connective tissue. Periosteum covers the bone surface, and endosteum is the tissue lining between compact and cancellous bone. Osteoblasts are derived from osteoprogenitor cells and their main function is to secrete the ECM of bone. Once they have been surrounded by the secreted ECM, they will become osteocytes with several processes to communicate with each other through canaliculi. (Pawlina and Ross 2016) Osteoblasts also form bone-lining cells to the bone surface, which release enzymes that help osteoclasts to attach and start bone resorption (Pawlina and Ross 2016; Tozzi *et al.*, 2016). Bone formation or ossification, where osteoblasts are differentiated from osteoprogenitor cells, is called intramembraneous bone formation. The other type of bone formation is called endochondral ossification, where osteoprogenitor cells are first differentiated into chondrocytes which further are mineralized and replaced by bone tissue. (Amini *et al.*, 2012) Osteoclasts, differentiated from hemopoietic progenitor cells, are also located on bone surface and their function is to resorb bone when it is removed or remodeled (Pawlina and Ross 2016). Bone is very dynamic and complicated tissue which constantly undergoes the cycle of resorption and renewal called remodeling process of the bone (Pawlina and Ross 2016; Amini *et al.*, 2012).

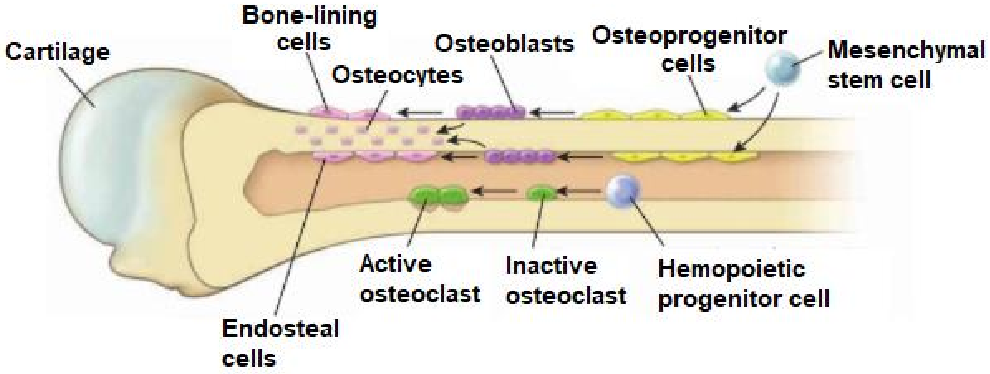

Figure 1. *Cell types of the human bone tissue. All bone cells are derived from mesenchymal stem cells, except osteoclasts which are derived from hemopoietic progenitor cells. Modified from: (Pawlina and Ross 2016)*

General structure of a long bone and its regions are presented in Figure 2 (A). Long bones can be named based on the region in question to diaphysis (midsection) and epiphysis (ends of a long bone). Metaphysis contains growth plate and is located between diaphysis and epiphysis. Main parts of all bones in human body are compact and hard cortical bone forming the outer layer of the bones and the inner porous cancellous bone, which forms a meshwork with spaces for bone marrow and blood vessels. (Pawlina and Ross 2016) The marrow cavity inside bones contains red bone marrow consisting of blood cells and yellow marrow consisting of fat cells. Hematopoiesis happens in red bone marrow whereas yellow bone marrow acts as an energy storage in adults. (Tozzi *et al.*, 2016; Pawlina and Ross 2016) Mature bone´s compact part is organized structurally to cylindrical units called osteons. Osteons consist of bone matrix organized to concentric lamellae, osteocytes located in spaces called lacunae, and central osteonal canal with blood vessels and nerves. (Pawlina and Ross 2016) Structure of osteons in compact bone is illustrated in Figure 2 (B). Based on bone tissue type, bones can be classified to mature bone having osteons and to less organized immature bone of a developing fetus (Pawlina and Ross 2016).

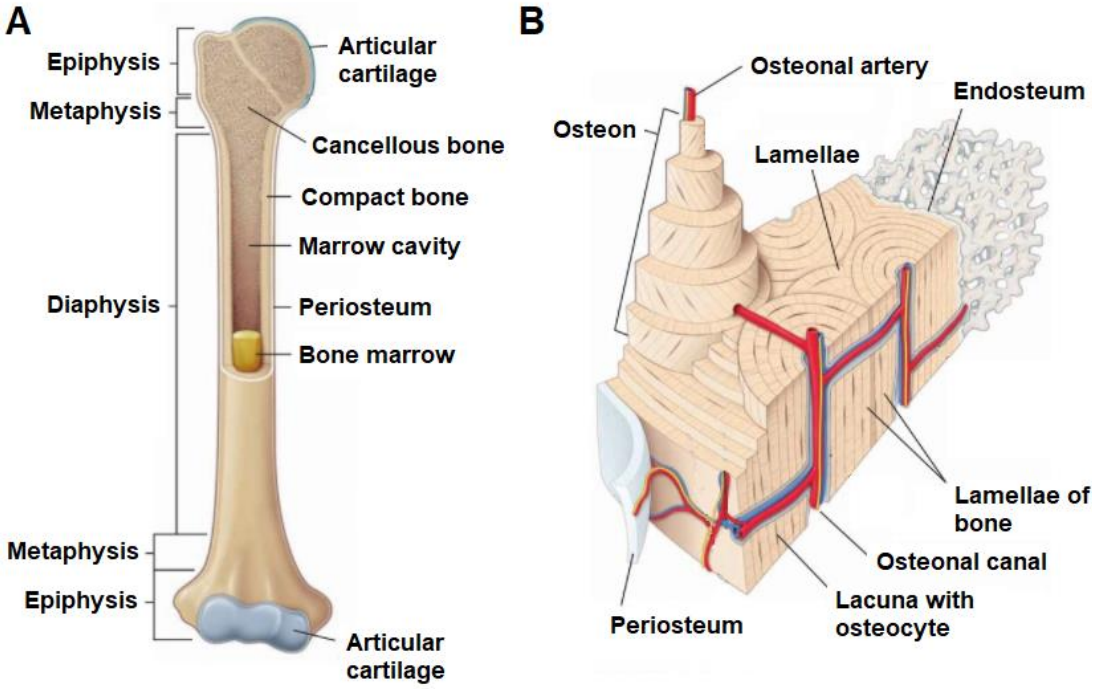

Figure 2. *General structure of a long bone and its regions (A). Organization of a compact bone into osteons (B). Modified from: (Pawlina and Ross 2016)*

Bone defects caused by bone diseases and bone traumas are continuously increasing mostly because of aging population (Office of the Surgeon General (US), 2004). Bone defects are mostly caused by trauma or tumor removal by surgery (Leberfinger *et al.*, 2017). Osteoporosis, which is a disease where the density of the bone decreases and the bone becomes more fragile due to bone tissue loss, is evaluated to become more common and it is one of the main reasons behind bone fractures (Pawlina and Ross 2016; Warriner *et al.*, 2011; Office of the Surgeon General (US), 2004). Bones can heal and they have a regeneration capacity to a certain point, but critical-sized bone defects require treatment to heal the tissue (Qu *et al.*, 2019; Tozzi *et al.*, 2016).

Autologous bone graft is the golden standard treatment for bone defects where a graft is taken from a donor site and moved to the injury site of the same patient (Qu *et al.*, 2019; Tozzi *et al.*, 2016; Amini *et al.*, 2012). Another method is to take the graft from a different donor to the patient which is called an allograft. By using autografts or allografts, biocompatibility, osteoconductivity, and osteoinductivity of the grafts is usually ensured, but problems such as secondary damages, morbidity in donor site, and limited possibilities to obtain certain shape and sufficient volume are related to their use (Qu *et al.*, 2019; Tozzi *et al.*, 2016; Amini *et al.*, 2012). In case of allografts, problems such as higher costs and risk for infections and immunoreactions are encountered when compared to use of autografts (Amini *et al.*, 2012). Xenografts, meaning graft material taken from another species, are third treatment option used for replacement of hard tissue (Sheikh *et al.*, 2017). Especially limited availability of the grafts is becoming more problematic since the need of functional bone grafts is growing all over the world (Amini *et al.*, 2012).

In addition to bone grafts, synthetic materials called alloplasts are also currently used to treat bone defects (Sheikh *et al.*, 2017; Basha *et al.*, 2015). For instance, inert metallic implants, ceramics, and some polymers are considered as alloplasts (Sheikh *et al.*, 2017; Tozzi *et al.*, 2016; Basha *et al.*, 2015). Inert metallic implants such as screws, rods, or plates have good mechanical properties but, on the other hand, can cause problems, such as corrosion, bone resorption, and implant loosening (Tozzi *et al.*, 2016; Basha *et al.*, 2015). Inert metallic implants also lack bioactivity, and they are not bioresorbable (Basha *et al.*, 2015). Ceramic implants, which are adaptive to wide scale of applications and have similar chemical and functional properties as bone, have weaknesses in low tensile strength, low fracture toughness, and brittleness, especially when it comes to porous ceramics (Tozzi *et al.*, 2016; Rezwan *et al.*, 2006).

2.1.1 Bone tissue engineering

Bone defects have become more common which increases the need for more effective treatment strategy options, such as for engineered bone tissue (Midha *et al.*, 2019; Tozzi *et al.*, 2016; Amini *et al.*, 2012). BTE searches approaches to cure bone defects and to solve problems related to currently used treatments (Qu *et al.*, 2019; Amini *et al.*, 2012). Key elements to consider in BTE are scaffolds (engineered biomaterials that mimic bone ECM), osteogenic cells, signaling molecules (growth factors), to stimulate cell proliferation and differentiation, and finally, vascularization of the tissue (Amini *et al.*, 2012).

Bone scaffolds with or without additives like growth factors or cells are commonly investigated treatment solutions in BTE field (Qu *et al.*, 2019). Scaffolds are usually made from one or more biomaterial and ideally, they should be biodegradable, biocompatible, bioactive, osteoconductive, and osteoinductive *in vivo* (Qu *et al.*, 2019; Turnbull *et al.*, 2018). Additionally, mechanical properties of the scaffold should represent the tissue type where the scaffold is implanted. An ideal scaffold should have surface and porosity suitable for cells to attach, migrate, proliferate, and differentiate. (Turnbull *et al.*, 2018)

Various materials such as natural and synthetic polymers, metals, and ceramics can be used for scaffold fabrication in BTE (Qu *et al.*, 2019; Turnbull *et al.*, 2018; Basha *et al.*, 2015). Scaffolds designed for BTE often include a ceramic phase such as calcium phosphate or bioactive glass (BaG) (Qu *et al.*, 2019). Bone morphogenic protein is one typical growth factor used in scaffolds to enhance bone formation (Turnbull *et al.*, 2018). Other potential and widely studied BTE application is the use of hydrogels as scaffold materials. Hydrogels are hydrophilic 3D polymer networks capable to swell and store significant volumes of water to their structure. (Turnbull *et al.*, 2018; Deligkaris *et al.*, 2010) Hydrogels can mimic the ECM well and are often injectable, biodegradable, biocompatible, and easily modifiable to support bone regeneration (Tozzi *et al.*, 2016). Limitation with hydrogels is that often their weak mechanical properties prevent their use in load bearing applications. Scaffolds are fabricated by conventional methods such as solvent casting-particulate leaching, phase separation, freeze-drying, and electrospinning. With these fabrication methods, precise control over the porosity and microarchitecture is usually lacking and the produced scaffolds might have incorrect anatomical shapes. (Turnbull *et al.*, 2018)

Classical cell-based approach in TE is to seed cells onto earlier fabricated scaffold, which is then implanted after *in vitro* maturation (Matai *et al.*, 2020; Groll *et al.*, 2016). Cell-based approaches have been examined in the field of BTE and their main benefit is more rapid bone regeneration and better vascularization when compared to scaffolds without cells (Amini *et al.*, 2012). Still, engineered bone scaffolds currently available do not completely mimic the hierarchy and anatomy of natural bone. In addition, the establishment of vasculature and the communication between different cell types in the construct is lacking and challenging to create. (Midha *et al.*, 2019; Leberfinger *et al.*, 2017) One of the challenges with cell-based approaches is to find the most effective cell source in order to establish vascularization and osteogenic differentiation (Amini *et al.*, 2012). Cell seeding on top of the scaffolds creates a nonordered and variating distribution of cells and, thus, natural tissue is not represented (Jungst *et al.*, 2016). Cell types used in BTE are for instance MSCs derived from adipose tissue, bone marrow, or human exfoliated deciduous teeth. Additionally, pluripotent stem cells are also used. As hBMSCs form bone in the natural bone development process, their potential in the field of BTE is considerable. Pre-differentiation of MSCs into the osteogenic lineage before implantation, has also been studied to further enhance bone formation and injury repair. However, the effect of donor characteristics, long culture times, and expansion periods before use in treatments are examples of the challenges related to MSCs. (Amini *et al.*, 2012)

2.2 3D bioprinting

Recently, biofabrication technologies have been introduced to the TE field to overcome the limitations with scaffolds and their conventional fabrication methods presented in chapter 2.1.1. Biofabrication, in the field of TE and regenerative medicine, uses automated processes that aim to generate cell-biomaterial constructs which finally are matured into functional target tissues. Biofabrication includes two main strategies which are 3D bioprinting and bioassembly. Bioassembly can be defined as "the fabrication of hierarchical constructs with a prescribed 2D" (two-dimensional) "or 3D organization through automated assembly of pre-formed cell-containing fabrication units generated via cell-driven self-organization or through preparation of hybrid cell-material building blocks, typically by applying enabling technologies, including microfabricated molds or microfluidics". (Groll *et al.*, 2016) The second main strategy in biofabrication, 3D printing, also known as additive manufacturing, is a technology where materials are placed to precise points in 3D space by using computer-controlled dispensing system (Li *et al.*, 2015). In 3D bioprinting, cells at high density are used in layer-by-layer printing to fabricate desired structures (O'Connell *et al.*, 2018; Dababneh and Ozbolat 2014). These printable mixtures consisting of cells with or without biomaterials are called bioinks (Groll *et al.*, 2019) and they are further discussed in chapter 2.3. In this thesis, the term "3D bioprinting" is used when the cells are included to the printable material, otherwise just "3D printing" is used. To summarize, main difference between bioassembly and 3D bioprinting is the length scale of the minimum fabrication unit, with 3D bioprinting being down to molecular level. With bioassembly, bigger building blocks with cells are used. (Groll *et al.*, 2016)

2.2.1 3D bioprinting for bone applications

3D printing enables the manufacturing of customized and anatomically correct tissue scaffolds, faster than before with desired porosity and structure (Ojansivu *et al.*, 2019; Ozbolat *et al.*, 2017; Li *et al.*, 2015). When compared to conventional fabrication methods presented in chapter 2.1.1, 3D printing enables more precise and repeatable manufacturing of scaffolds (Turnbull *et al.*, 2018). In addition to structural properties, mechanical properties of the printed product can also be modified easily, and better cellular response can be obtained by loading drug or protein molecules into the scaffolds. However, limitations such as lack of precision in cell seeding on top of the 3D printed scaffold and insufficient cell penetration into the scaffold matrix, exists. This causes difficulties to produce vascularized and hierarchical natural tissue resembling constructs in 3D printing for TE. (Ozbolat *et al.*, 2017) In BTE, 3D printed constructs without cells are already used in patient treatments with clinical trials in orthopedic surgery, maxillofacial surgery, and dentistry (Matai *et al.*, 2020).

3D bioprinting, the use of cells with biomaterials, has the potential to solve the limitations of 3D printing and implement the fabrication of complex tissues and organs for TE applications or for research purposes (Levato *et al.*, 2017; Ozbolat *et al.*, 2017). When compared to traditional TE approaches, 3D bioprinting is seen as a potential solution to create organized, natural tissue resembling large constructs with vascularization and/or porosity to enable exchange of gas and nutrients (Vijayavenkataraman *et al.*, 2018; Jungst *et al.*, 2016). In the field of BTE, 3D bioprinting is widely studied and a promising method to engineer complex patient specific bone grafts (Matai *et al.*, 2020; Midha *et al.*, 2019). Moreover, the approach is easily customizable and has a good reproducibility (Matai *et al.*, 2020). 3D bioprinting targets to clinical translations but at this point it´s mainly been used in basic science, *in vitro* models for drug testing, material testing, disease modelling, and in pre-clinical studies (Matai *et al.*, 2020; Vijayavenkataraman *et al.*, 2018; Ozbolat *et al.*, 2017; Zhang, Y. S. *et al.*, 2017). In case of BTE, clinical trials of 3D bioprinted cell embedded bone constructs are yet to come and only couple of studies are found where bone formation of bioprinted constructs is studied *in vivo* (Loai *et al.*, 2019; Ashammakhi *et al.*, 2019). As 3D bioprinting can offer functional and accurate models for a wide field of pre-clinical testing, it can also reduce the use of animal tests (Matai *et al.*, 2020).

The cell distribution and construct fabrication can be precisely controlled in 3D bioprinting (Matai *et al.*, 2020; Derakhshanfar *et al.*, 2018). In 3D bioprinting either already differentiated cells or stem cells can be used, and the cell type chosen depends on the target tissue. For 3D bioprinting of complex tissues like bone, use of stem cells is more beneficial and makes the fabrication process easier. Already differentiated cells in turn are good choice for 3D bioprinting of more simple single tissues. (Matai *et al.*, 2020) In 3D bioprinting of bone, patient specificity can be achieved by using adult MSCs isolated from dental pulp, adipose tissue, or bone marrow of a patient (Midha *et al.*, 2019). Several studies have used hBMSCs in 3D bioprinting of bone (Cidonio *et al.*, 2019; Ojansivu *et al.*, 2019; Byambaa *et al.*, 2017; Gao *et al.*, 2014). Other potential cell source in the future for personalized bone 3D bioprinting can be the use of MSCs derived from iPSCs (Ashammakhi *et al.*, 2019). In order to fabricate natural bone -like construct, both osteogenic and angiogenic cell types can be combined to the same bioink used in 3D bioprinting (Ashammakhi *et al.*, 2019). By using more than one printhead, several bioinks with different cell types can be utilized in a fabrication of a single construct (Gungor-Ozkerim *et al.*, 2018). Cell density in the bioink depends on what is the target tissue in bioprinting (Matai *et al.*, 2020), for instance for bone tissue, recommended cell density in a bioink is 5 to 10 million cells per milliliter of the bioink (Fedorovich *et al.*, 2011).

One of the main challenges in 3D bioprinting is the development and optimization of the bioinks as various requirements related to cell function and printability of the bioinks exist (Morgan *et al.*, 2020; Gungor-Ozkerim *et al.*, 2018; Ozbolat *et al.*, 2017; Jungst *et al.*, 2016). Bioinks and their optimization is further discussed in chapter 2.3. Other considerable limitations with 3D bioprinting also exist outside the challenges related to bioinks. For example, the size of the bioprinters and the working space required is still relatively large with some 3D bioprinter models, which complicates sterile printing (Ozbolat *et al.*, 2017). 3D bioprinting of clinically relevant large constructs is also challenging because the speed of the bioprinting is still relatively slow and the printing resolution of the most used modalities still needs improvements (Cui *et al.*, 2020; Ozbolat *et al.*, 2017; Murphy and Atala 2014). Commercial bioprinters are also limited in variety, motion capability, and automation. In addition, the costs are relatively high. Extrusion-based 3D bioprinting technologies are currently the most available ones, compared to laser-based and droplet-based bioprinters. (Ozbolat *et al.*, 2017)

When considering 3D bioprinted constructs and their implantation, the establishment of vasculature to enable nutrient, growth factor, waste product, and oxygen change is a challenge to be addressed (Derakhshanfar *et al.*, 2018). For instance, in 3D bioprinting of bone, one major challenge is to create the complex structure of the natural bone with vascularization and successfully 3D bioprint larger human-scale bone constructs with functional nutrient and oxygen supply (Midha *et al.*, 2019). As bone tissue is commonly load-bearing, insufficient mechanical properties of the 3D bioprinted hydrogel constructs must be solved. Combination of hard 3D printed scaffold and soft 3D bioprinted bioink fabricated simultaneously with multi-head printer could be one solution for this issue. (Ashammakhi *et al.*, 2019) In order to achieve clinical translation in the bioprinting field, challenges mentioned should be solved (Cui *et al.*, 2020). However, these issues are continuously handled and solutions for those are found when 3D bioprinting technologies are developed further, new bioinks studied, and the field grows (Derakhshanfar *et al.*, 2018).

Typical workflow for 3D bioprinting includes preprocessing or reconstitution of a 3D model, actual 3D bioprinting, and postprocessing of the bioprinted construct. 3D model or design for the bioprinter is made by using Computer-aided design and manufacturing. The model can be based on real organ or tissue of a patient imaged by using modalities, such as computed tomography (CT) and magnetic resonance imaging. By this way patient-specific data can be achieved. Preprocessing before 3D bioprinting also includes validation and optimization of the bioink to be used. After 3D bioprinting, postprocessing includes crosslinking of the construct, if it is not done simultaneously with 3D bioprinting, and a maturation phase of the construct. (Vijayavenkataraman *et al.*, 2018)

2.2.2 3D bioprinting modalities

Several types of 3D bioprinters with different fundamental working principles exist, but main technologies currently available are droplet-, laser-, and extrusion-based bioprinters (Figure 3) (Ozbolat *et al.*, 2017). Lithography-based bioprinting is the fourth newer modality (Figure 4) (Vijayavenkataraman *et al.*, 2018). In addition to these, modalities such as magnetic and acoustic bioprinters exist (Matai *et al.*, 2020).

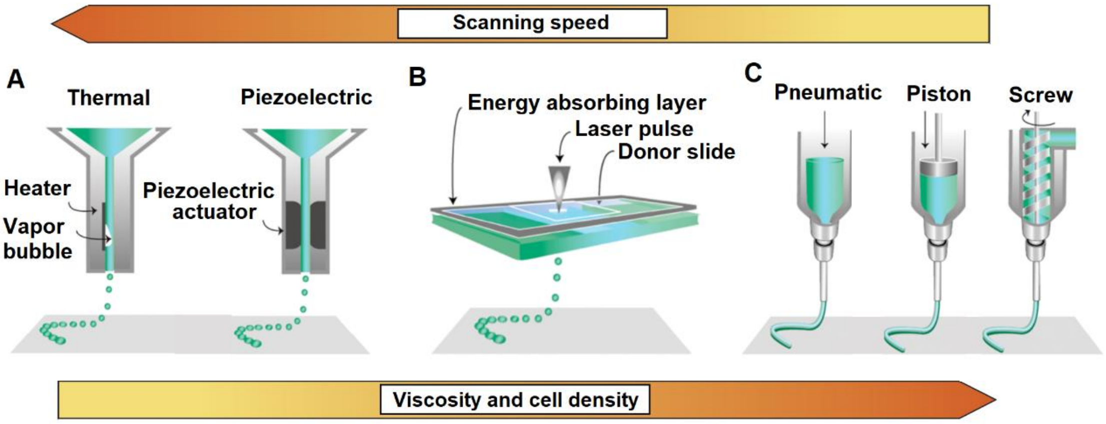

Figure 3. *Droplet- (A), laser- (B), and extrusion-based (C) 3D bioprinting modalities and their working principles. With extrusion-based bioprinter more viscous bioinks with higher cell densities can be printed when compared to other modalities. Faster speed of the printing process in turn is achieved with laser- and droplet-based bioprinters. Modified from:* (Hölzl *et al.*, 2016; Jungst *et al.*, 2016)

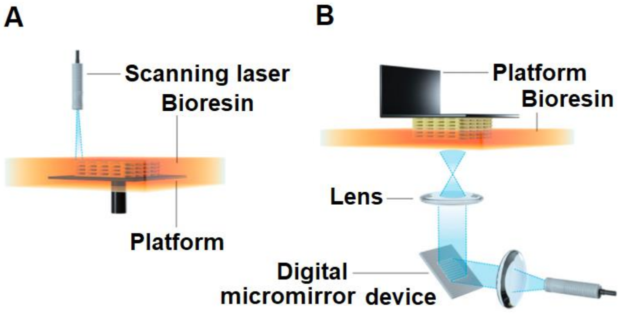

Figure 4. *Lithography-based 3D bioprinting modalities stereolithography (A) and digital light processing (B) and their working principle. Modified from:* (Lim et al., 2020)

Droplet-based 3D bioprinting is a discontinuous method, where a bioink comes out of the nozzle in droplets onto a substrate (Morgan *et al.*, 2020; Vijayavenkataraman *et al.*, 2018). Droplet-based inkjet 3D bioprinting is a fast method to fabricate constructs with high resolution (50 µm) and by using less viscous bioinks (Derakhshanfar *et al.*, 2018). In drop-on-demand (DOD) inkjet 3D bioprinting (Figure 3 (A)), thermal, piezoelectric, or electrostatic trigger generates bioink droplets (Vijayavenkataraman *et al.*, 2018). DOD inkjet 3D bioprinting is economical, simple, and efficient bioprinting modality. Problems in DOD inkjet 3D bioprinting exist, such as needle clogging and when droplets are created, thermal and shear forces may decrease cell viability. (Matai *et al.*, 2020) Cell density in inkjet 3D bioprinting is lower than with other technologies and the ability of vertical bioprinting with this modality is poor (Derakhshanfar *et al.*, 2018).

In laser-based 3D bioprinting, bioinks are patterned by using laser energy (Vijayavenkataraman *et al.*, 2018). Laser-induced forward transfer (LIFT) technology (Figure 3 (B)) is one laser-based 3D bioprinting technique. In LIFT, laser energy absorbed to absorbing layer in the laser transparent print ribbon, coated with bioink, generates pressure, which causes bioink droplet movement to collector or substrate layer (Matai *et al.*, 2020; Vijayavenkataraman *et al.*, 2018). Laser-based 3D bioprinting is a nozzle free technique which solves the problem with nozzle clogging and enables 3D bioprinting of bioinks with different viscosities (Vijayavenkataraman *et al.*, 2018). Challenges in laser-based 3D bioprinters are the high costs of the systems, slow fabrication speed, and the possible difficulties in laser control (Matai *et al.*, 2020; Vijayavenkataraman *et al.*, 2018). When thinking of the cells, lasers used may damage them, even if the technique tries to minimize the laser exposure to cells by using low energy lasers and thick sacrificial layers (Vijayavenkataraman *et al.*, 2018).

Lithography 3D bioprinting includes bioprinting modalities such as stereolithography (SLA) (Figure 4, (A)) and digital light processing (DLP) (Figure 4, (B)) (Lim *et al.*, 2020; Vijayavenkataraman *et al.*, 2018). In lithography 3D bioprinting, specifically targeted and controlled light causes polymerization of light sensitive polymers in a bioink creating a construct (Derakhshanfar *et al.*, 2018). In SLA, focused laser light, and in DLP, digital micromirror devices are used in 3D bioprinting to crosslink specific areas in a bioresin bath. Bioresins are bioinks specially designed for lithography 3D bioprinting. (Lim *et al.*, 2018) Lithography 3D bioprinting offers a nozzle free bioprinting approach with relatively high accuracy, speed, and cell viability (Derakhshanfar *et al.*, 2018). Stereolithography 3D bioprinting and laser-based 3D bioprinting have the best resolution when compared to other modalities. Very limiting factor in stereolithography 3D bioprinting is that only bioinks crosslinked by light can be used with the modality. (Vijayavenkataraman *et al.*, 2018)

2.2.2.1 Extrusion-based 3D bioprinting

Extrusion-based 3D bioprinting technology is the most popular adopted approach to create large cellular structures (Figure 3 (C)) (Matai *et al.*, 2020; Vijayavenkataraman *et al.*, 2018). In extrusion-based 3D bioprinting, a viscous bioink is placed on to a sterile syringe barrel and extruded as a continuous filament through a micro-nozzle tip, by using pneumatic- or mechanical-driven extrusion (Matai *et al.*, 2020; Ozbolat *et al.*, 2017). After printing the structure can be crosslinked by using different crosslinking strategies such as light, chemicals, heat, or enzymes (Matai *et al.*, 2020). The greatest benefit in extrusion 3D bioprinting is the scalability, as the well-controlled flow rate and continuous flow of the bioink enable construction of large tissue-like structures (Vijayavenkataraman *et al.*, 2018). Usually in extrusion bioprinters, pressure, syringe barrel temperature, platform position, and platform temperature can be strictly controlled to enable better accuracy and reproducibility of the process (Matai *et al.*, 2020). Extrusion-based bioprinters are also capable to print more viscous bioinks up to 300 000 Pa s with high cell densities, than for example droplet 3D bioprinting is capable to use (Matai *et al.*, 2020; Derakhshanfar *et al.*, 2018; Hölzl *et al.*, 2016). Extrusion 3D bioprinting is considered to be simple and various biomaterials can be used with the modality (Derakhshanfar *et al.*, 2018). New trend in extrusion 3D bioprinting is the use of coaxial nozzle which enables fabrication of either hollow or bulk hydrogel fibers crosslinked already in the nozzle (Costantini *et al.*, 2019; Derakhshanfar *et al.*, 2018). In this technology, bioink and crosslinker solution are 3D printed through a separate co-axial arrangement of assembled nozzles. Coaxial extrusion 3D bioprinting can be the solution for establishment of vasculature and bioprinting of multicellular constructs. (Costantini *et al.*, 2019)

Challenges in extrusion-based bioprinters are nozzle clogging and specific shear-thinning properties required for the bioink (Matai *et al.*, 2020; Vijayavenkataraman *et al.*, 2018). Possibility to 3D bioprint only more viscous bioinks can also be considered as disadvantage (Derakhshanfar *et al.*, 2018). Printing resolution, usually over 100 µm, in extrusion bioprinting is lower than in other bioprinting modalities (Zhang, B. *et al.*, 2017; Dababneh and Ozbolat 2014). The diameter of the used nozzle tip affects printing resolution and, hence, by decreasing the nozzle tip diameter a better resolution can be achieved (Morgan *et al.*, 2020). However, a decrease in nozzle diameter causes increase in printing pressure which can affect negatively on cell viability, as the cells experience higher shear stress (Matai *et al.*, 2020). With a careful optimization of the bioinks and printing parameters, the challenges related to extrusion 3D bioprinting can be minimized (Dababneh and Ozbolat 2014).

2.3 Bioinks

In the field of 3D bioprinting, a lot of diversity exists in the use of the word “bioink”. When 3D bioprinting has become more known and new techniques for it are adapted, the word bioink has started to refer more to the dispensed material used in 3D bioprinting. In this thesis the word bioink is used as Groll *et al.* describes it: “a formulation of cells suitable for processing by an automated biofabrication technology that may also contain biologically active components and biomaterials”. Different materials can be used as an additional component with cells in the bioink but they are not mandatory like cells are. Groll *et al.* also describes biomaterial inks as “aqueous formulations of polymers or hydrogel precursors that contain biological factors”, which can become bioinks if cells are added. For example, materials that are 3D printed and afterwards seeded with cells, or sacrificial materials dissolving away after 3D printing are biomaterial inks, not bioinks. The term “biomaterial ink” is used in this thesis as Groll *et al.* describes it. (Groll *et al.*, 2019)

2.3.1 Optimization of bioinks

The essential part of the 3D bioprinting process is optimization of a bioink so that the printability, crosslinking, biocompatibility, and degradation of the used bioink is optimal for the application. Optimization process depends on the printing modality, cell type, and target tissue (Gungor-Ozkerim *et al.*, 2018; Ozbolat *et al.*, 2017). Cell viability, bioink´s effect on cell behaviour and printability of the bioink are three main aspects to consider in the optimization (Parak *et al.*, 2019). When bioinks are designed, clinical translation should also be considered, for example the sterility of the fabrication process and the materials, including that they are endotoxin free (Jungst *et al.*, 2016).

Other important aspects to take into account in the bioink development are viscosity, shear thinning, viscoelasticity, gelation kinetics, and biodegradation (Cui *et al.*, 2020; Matai *et al.*, 2020). Viscosity means the resistance of flow when pressure or stress is applied to a fluid (Cui *et al.*, 2020). It is one of the main aspects to be consider in the bioink optimization, since it should be ideal to enable smooth printing process and after that stabilization of a bioprinted construct through gelation or shear thinning properties (Matai *et al.*, 2020). In hydrogels polymer concentration and molecular weights affect viscosity (Cui *et al.*, 2020). Too high viscosity affects negatively cell viability, spreading, and activity as high polymer content in the bioink causes high stress to encapsulated cells (Matai *et al.*, 2020; Morgan *et al.*, 2020). Viscosity of the bioink can be adjusted through the composition of the bioink, by changing the concentration of a chosen polymer, or in use by manipulating the bioink’s temperature (Cui *et al.*, 2020). With additives such as nanocellulose, nHA, or sacrificial materials, like hyaluronic acid or gelatin, the rheological properties of the bioink can also be modified (Lim *et al.*, 2020). For instance, by adding a ceramic phase, such as nHA, to the bioink increases the vicosity (Wüst *et al.*, 2014).

Shear-thinning behaviour describes material´s ability to decrease viscosity by reorganization of the polymer chains when it´s exposed to shear stress and afterwards recover its viscosity (Morgan *et al.*, 2020; Cui *et al.*, 2020). Optimal shear-thinning characteristics of the bioink are crucial, especially in extrusion 3D bioprinting, since a bioink must have a smooth flow with a relatively low viscosity from the nozzle followed by stabilization (Cui *et al.*, 2020; Groll *et al.*, 2019). Better structural integrity of the bioink is achieved if the bioink has fast shear recovery from low to high viscosity after bioprinting (Cui *et al.*, 2020).

At the same time with viscosity and shear-thinning properties, used temperature range, and mechanical shear forces must be considered so that the condition remains compatible for the cells (Jungst *et al.*, 2016). Bioinks also need to have optimal mechanical properties for printing (Derakhshanfar *et al.*, 2018). Adjusting all these parameters is one of the major challenges in extrusion 3D bioprinting (Groll *et al.*, 2019) and as these various requirements exist related to the bioink development, there is a lack of standardized bioinks for 3D bioprinting (Gungor-Ozkerim *et al.*, 2018).

2.3.2 Crosslinking of bioinks

Crosslinking of a bioink during or after 3D bioprinting process is a way to ensure long-term stability of the construct. Crosslinking method for the bioink should be carefully designed so that cell viability and functionality are not violated. If crosslinking of the bioink is not successful and remains uncompleted, it can cause more rapid degradation and collapse of the construct and loss of its shape. (Cui *et al.*, 2020) Hydrogel precursors most used in bioinks can be divided into chemically and physically crosslinkable ones (Jungst *et al.*, 2016). With multicomponent bioinks, more than one crosslinking strategies can be used (Cui *et al.*, 2020; Lim *et al.*, 2020).

Physically crosslinked hydrogels form reversible crosslinking by noncovalent bonds, and they are considered especially potential ones for bioinks. This is because of their reversibility and shear thinning behavior, which leads to ability to retain their shape after 3D bioprinting. (Jungst *et al.*, 2016) Noncovalent bond formation can result for instance by electrostatic or hydrophobic interactions or by hydrogen bond interaction (Cui *et al.*, 2020). For example, many bioinks are crosslinked by calcium ion crosslinking of alginate, which is commonly used in 3D bioprinting (Morgan *et al.*, 2020; Cui *et al.*, 2020). This method is based on electrostatic interactions, as calcium ions change the pH value of the bioink causing protonation of charged functional groups (Cui *et al.*, 2020).

Chemically crosslinked hydrogels are less dynamic and more stable than physically crosslinked hydrogels, as they form covalent bonds to create 3D networks (Jungst *et al.*, 2016). When compared to physically crosslinked bioinks, better mechanical properties can be achieved by using chemical crosslinking. In order to form covalent bonds between polymers in the bioink, multifunctional monomers called crosslinkers are used in chemical crosslinking. Functionality of crosslinkers can be based on for instance, radical polymerization, Schiff's-based reaction, or enzymatic reaction. Radical polymerization is currently the most used chemical crosslinking method from these. (Cui *et al.*, 2020)

2.3.2.1 Light induced crosslinking

Light induced crosslinking, including UV light crosslinking, is a chemical crosslinking strategy caused by photo-initiated free-radical polymerization in a bioink (Pahoff *et al.*, 2019; O'Connell *et al.*, 2018). Photoinitiators are molecules used as crosslinkers in light-based crosslinking, which absorb photons and form radical species when exposed to UV light. After this, free radicals form covalent bonds between polymer chains functional groups causing propagation of radical species. Propagation of radical species can especially happen through unreacted double bonds such as methacrylates, acrylates, or acrylamides. Finally, kinetic chains between polymers are formed. (Lim *et al.*, 2020) Existing photoinitiators are for example IC, tris(2,2- bipyridyl) dichlororuthenium (II) hexahydrate (Ru) together with sodium persulfate (SPS), lithium phenyl-2,4,6-trimethylbenzoylphosphinate (LAP), and eosin Y (Pahoff *et al.,* 2019; Lim *et al.,* 2018; Lim *et al.,* 2016). As an example, UV light induced crosslinking of GelMA with IC by photo-initiated free-radical polymerization is presented in Figure 5. Other two possible reactions to cause photo-crosslinking of a bioink are thiol−ene photo-crosslinking and photomediated redox crosslinking (Lim *et al.*, 2020).

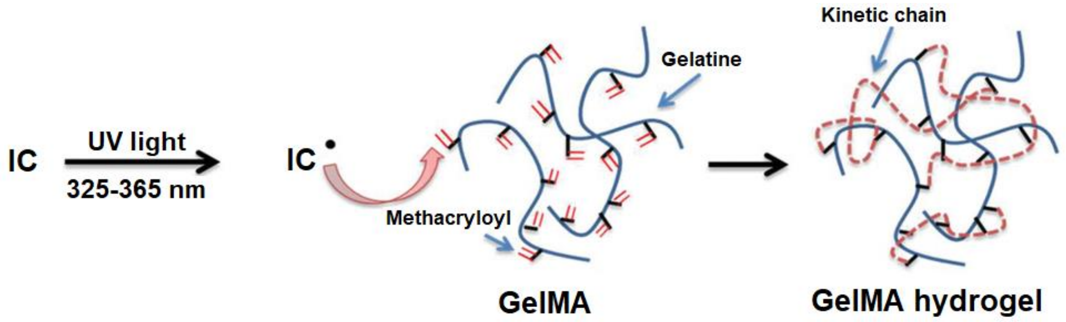

Figure 5. *UV light induced crosslinking of GelMA with photoinitiator IC. UV light exposure causes IC to form radical species, which form covalent bonds between polymer chains functional groups causing propagation of radical species and finally kinetic chains between polymers are formed. Modified from:* (Lim *et al.*, 2019)

Many bioinks are crosslinked by using light and photo-crosslinkable materials, such as GelMA or polyethylene glycol diacrylate (PEGDA) (Morgan *et al.*, 2020). Light induced crosslinking is considered especially suitable for extrusion and stereolithography 3D bioprinting and it can be used either continuously during the printing process, after it, or after each printed layer (Lim *et al.*, 2020). In light induced crosslinking, both properties of a hydrogel precursor (reactive group concentration) and photo-crosslinking conditions, such as photoinitiator concentration, light intensity and light wavelength, affect the result (Lim *et al.*, 2020; Pahoff *et al.*, 2019; O'Connell *et al.*, 2018). The photoinitiator chosen for crosslinking also influences light intensity and exposure time needed for crosslinking. Successful light induced crosslinking also depends on the transparency of the bioink, and because of that, for example additives used in the bioink should be transparent. (Lim *et al.*, 2020) Light induced photo-crosslinking is seen very promising for TE, since issues related to crosslinking methods currently available, such as cytotoxicity, inflammatory responses *in vivo*, and difficulties in crosslinking reaction managing, can possibly be solved with it (Cui *et al.*, 2020; Pahoff *et al.*, 2019). Still, more studies are needed for the evaluation of the biocompatibility of the photoinitiators and crosslinking process (Cui *et al.*, 2020).

2.3.3 Common biomaterials in bioinks

One of the main challenges in 3D bioprinting is to find cytocompatible and suitable materials to prepare a bioink (Gungor-Ozkerim *et al.*, 2018; Ozbolat *et al.*, 2017; Jungst *et al.*, 2016). Hydrophilic polymer precursors crosslinked post-fabrication into hydrogels, are materials which are often used in the bioink since they enable homogenous cell seeding, support for the cells, and hydrated ECM resembling 3D environment (Cui *et al.*, 2020; Groll *et al.*, 2019; Jungst *et al.*, 2016; Dababneh and Ozbolat 2014). Additionally, hydrogel precursors in the bioink protect the cells during printing process. They can also enhance cell growth and functionality through physical and chemical stimulation. (Cui *et al.*, 2020)

The used polymers in bioinks can be either synthetic, natural, or a combination of several polymers can be used (Matai *et al.*, 2020). Natural polymers are beneficial in bioinks since they are biocompatible, usually biodegradable, bioactive, and have good viscosity for bioinks. However, issues like patch variation, poor mechanical properties and insufficient tailorability limit their use. (Morgan *et al.*, 2020; Lim *et al.*, 2020; Parak *et al.*, 2019) For instance, alginate, collagen, and gelatin are natural polymers used in bioinks. Collagen is a protein which is widely used in many biomedical applications, as it is biocompatible and in human it forms a major part of the ECM of tissues. It is used for instance in 3D bioprinting for bone and skin applications. (Gungor-Ozkerim *et al.*, 2018) Gelatin is made from denatured collagen, which supports cell attachment and spreading through its adhesive peptide sequences (Lim *et al.*, 2020). It is relatively cheap biomaterial, easy to process, and has thermoresponsive characteristics, which means that it can be reversibly crosslinked by thermal gelation. Alginate in turn is a polysaccharide which resembles glycosaminoglycans of human body and can be processed from brown seaweed. (Gungor-Ozkerim *et al.*, 2018) It is also cheap and biocompatible material, which has relatively high viscosity and fast gelation kinetics suitable for 3D bioprinting (Ashammakhi *et al.*, 2019). Bioinks based on alginate and gelatin are very common hydrogel systems used in 3D bioprinting and biofabrication studies (Gungor-Ozkerim *et al.*, 2018; Jungst *et al.*, 2016). Other natural biomaterials used in bioinks are for instance fibrinogen and fibrin, silk, hyaluronic acid, and different decellularized ECM-based biomaterials (Gungor-Ozkerim *et al.*, 2018).

Synthetic polymers do not resemble the natural ECM as much as natural polymers and usually without modification they lack cell binding sites. However, they are more scalable and can be better tailored, controlled, and reproduced. (Morgan *et al.*, 2020; Lim *et al.*, 2020) For instance, polyethylene glycol (PEG) is a bioinert synthetic polymer, which can be easily tailored, is non-cytotoxic, and has good mechanical properties for 3D bioprinting. PEG can be modified, for instance to photo-crosslinkable PEGDA or it can be combined with biologically active materials. Another synthetic polymer used in 3D bioprinting is poloxamer pluronic. (Gungor-Ozkerim *et al.*, 2018)

Rapid development of 3D bioprinting technologies has led to development of multicomponent bioinks, which are bioinks composed of more than one hydrogel precursors or other components. For instance, the use of a one or more base polymer together with printability and biofunctionality improving nanoparticles, is a common strategy to develop a multicomponent bioink. Multicomponent bioinks are potential for

3D bioprinting, since the combination can result in a more preferable shear thinning behaviour for bioprinting process and increased biofunctionality, in comparison to single component bioinks. (Cui *et al.*, 2020) Many biomaterials commonly used in bioinks, such as collagen, gelatin and alginate presented earlier, are also used in multicomponent bioink applications for 3D bioprinting (Gungor-Ozkerim *et al.*, 2018).

2.3.3.1 Gelatin methacryloyl and photoinitiator Irgacure 2959

Modified natural polymer GelMA is potential for 3D bioprinting as it mimics well the natural ECM of various cell types (Lim *et al.*, 2020; O'Connell *et al.*, 2018). For instance, photo-crosslinked GelMA-based hydrogels have been reported to support cell viability of encapsulated hMSCs after printing and crosslinking with UV (O'Connell *et al.*, 2018; Levato *et al.*, 2017). GelMA is made from engineered gelatin by esterification with methacrylic anhydride. This forms methacryloyl groups, which can be photo-crosslinked by free-radical chain polymerization. (Lim *et al.*, 2020) Modified forms of gelatin are used in the bioinks since crosslinking of the gelatin by thermal gelation is an unstable and slow process (Gungor-Ozkerim *et al.*, 2018). GelMA also has preferable properties when considering printability, as it has good mechanical stability, fast gelation, and it is thermosensitive (Cui *et al.*, 2020). Mechanical properties of the final construct can be easily modified by adjusting photocrosslinking conditions of the GelMA bioink (Gungor-Ozkerim *et al.*, 2018). Photoinitiator IC is most commonly used for crosslinking of photo-crosslinkable hydrogel precursors like GelMA (Figure 5) as it is more cytocompatible and minimally toxic for mammalian cells when compared to other existing photoinitiators (Pahoff *et al.*, 2019; Ashammakhi *et al.*, 2019; O'Connell *et al.*, 2018; Levato *et al.*, 2017). Other existing photoinitiators such as Ru together with SPS, LAP, and eosin Y, have also been used in photo-crosslinking of GelMA (Pahoff *et al.*, 2019; Lim *et al.*, 2018; Lim *et al.*, 2016).

GelMA and photo-crosslinking with UV light and IC are studied for various 3D bioprinting applications. However, a lot of variation exists in the literature regarding concentrations, UV exposure times, and other crosslinking parameters. (Lim *et al.*, 2020) Low concentration of GelMA (<5 w/v %) in the bioink is considered to cause poor printability because of too low viscosity for printing process. GelMA concentrations higher than 15 w/v % can enhance printability without affecting shear-thinning properties of the bioink but on the other hand, might decrease cell viability, function, and growth. (Yin *et al.*, 2018) It has been studied that higher IC concentrations, UV intensities, and UV exposure times have a negative effect on cell viability (Stratesteffen *et al.*, 2017; Lim *et al.*, 2016). On the other hand, lower values can lead insufficient crosslinking, degradation, and collapse of the construct. UV intensities used in photo-crosslinking vary a lot from 1.2 to 850 mW/cm^2 (Lim *et al.*, 2020). Recent 3D bioprinting studies made in the field, used GelMA and IC concentration, and used UV exposure times for crosslinking are presented in Table 1. In the found literature, it must be noted that the intensity, distance, and type of the UV light used vary between studies made. Degree of functionalization of GelMA, size of the bioprinted construct, and the used cell types also differ between studies. Wavelength of 365 nm is usually used in crosslinking, even if IC has a low molar absorptivity in that wavelength, since more low-wavelength UV light is reported to be more cytotoxic and genotoxic (Lim *et al.*, 2020).

Table 1. *Concentrations of GelMA and IC with used UV exposure times in earlier 3D bioprinting studies.*

GelMA (% w/v)	IC (% w/v)	UV exposure time	Target tissue	Reference
10	0.1	10 s/layer and 300 s after bioprinting	Cartilage	(Levato *et al.*, 2017)
10	0.025–0.1	300 s after bioprinting	Heart	(Kang *et al.*, 2017)
10	0.05	900 s after bioprinting	Cartilage, bone	(Lim *et al.*, 2016)
10	0.1	Continuous, 30 s after bioprinting	-	(Tigner *et al.*, 2020)
10	0.1	300 s after bioprinting	Cartilage, bone	(Levato *et al.*, 2014)
10	0.2	20 s before bioprinting for each filament	Bone	(Byambaa *et al.*, 2017)
5	0.5	20 s/layer	Vasculature	(Krishnamoorthy *et al.*, 2020)

Both Tigner *et al.* and Krishnamoorthy *et al.* used GelMA-based bioink in 3D bioprinting with embedded fibroblasts to examine the effects of crosslinking conditions and used materials (Krishnamoorthy *et al.*, 2020; Tigner *et al.*, 2020). Krishnamoorthy *et al.* focused to the optical properties of GelMA and found that increased degree of functionalization of GelMA, polymer concentration, or photoinitiator concentration significantly decreased UV penetration depth. Increase in polymer or photoinitiator concentration also increased UV energy required for the initiation of crosslinking. On the contrary, increase in degree of functionalization of GelMA decreased significantly required UV energy. Additionally, Krishnamoorthy *et al.* fabricated vascular-like construct by using their GelMA-based bioink with fibroblasts and stereolithography 3D bioprinting. Cell survival was followed over 48 hours after fabrication and was found to be good. (Krishnamoorthy *et al.*, 2020) Tigner *et al.* compared gelatin derivatives gelatin−norbornene (GelNB) and GelMA with each other by using photocrosslinking, with either IC or LAP, and extrusion 3D bioprinting. The stability of GelNB after printing was found to be better than with GelMA, however GelMA was more easily printable with lower stress. With both derivatives and photoinitiators cell viability of the fibroblasts was high after 3D bioprinting process. (Tigner *et al.*, 2020)

In addition to 3D bioprinting, GelMA, as a base component with photoinitiator IC and embedded cells, is also widely used in other forms, such as in castings. Concentrations of GelMA and IC with used UV exposure times in studies where they are used in castings or in other forms are collected on Table 2. Pahoff *et al.* fabricated chondrocyte-laden hydrogel constructs reinforced with medical grade polycaprolactone microfibre scaffolds and compared the effect of gelatin source and photoinitiator type on cell differentiation. IC crosslinked constructs resembled more native articular cartilage when compared to LAP crosslinked constructs. Cytotoxicity of the photoinitiators or generation of free radicals in the crosslinking process was estimated to be the reason why cell viability was decreased in all groups on day 28. (Pahoff *et al.*, 2019)

Table 2. *Concentrations of GelMA and IC with UV exposure times in castings or other forms.*

GelMA (% w/v)	IC (% w/v)	UV exposure time (s)	Target tissue	Reference
15	0.25	80	Bone	(Sawyer *et al.*, 2018)
15	0.5	40	Vascularization	(Eke *et al.*, 2017)
10	0.05	900	Cartilage	(Lim *et al.*, 2019)
10	0.25	900	Cartilage	(Pahoff *et al.*, 2019)
10	0.1	5–20	Bone (Endodontics)	(Monteiro *et al.*, 2018)
10	0.5	37–316	-	(O'Connell *et al.*, 2018)
10	0.75	120	Cartilage, bone	(Barati *et al.*, 2017)
10	0.05–0.2	900	Cartilage	(Bartnikowski *et al.*, 2015)
5	0.5	60	-	(Choi *et al.*, 2019)
5	0.5	10	-	(Wang, H. *et al.*, 2014)
5	0.2–1.0	300	-	(Jung and Oh 2014)
5	0.5	30	-	(Ramón-Azcón *et al.*, 2012)
3–5	0.2–0.5	129-720	Vasculature	(Stratesteffen *et al.*, 2017)

In another study, Sawyer *et al.* combined casting of Saos-2 cells (human osteosarcoma cell line) embedded in GelMA together with 3D printed sacrificial polyvinyl alcohol filaments to create bone construct with perfused channels. Constructs having osteogenic media perfused channels had high cell viability and the cells surrounding the channels were observed to produce more mineralized matrix. The importance of functional oxygen and nutrient supply to create natural tissue resembling constructs with cells was demonstrated in this study. (Sawyer *et al.*, 2018) Stratesteffen *et al.* did a comprehensive study handling the effect of UV exposure time and photoinitiator IC concentration on crosslinking, printability, and rheological properties of the GelMA-collagen I blends. Additionally, cell viability of embedded hMSCs and endothelial cells was observed. Range of UV light exposure times (2–12 min) and IC concentrations (0.2–0.5 % w/v) were tested and, as a result, highest exposure times and IC concentrations were found to affect negatively on cell viability. The cells embedded in GelMA-collagen I hydrogels were also reported to have capillary-like structures formation and, hence, being potential for fabrication of vascularized constructs. (Stratesteffen *et al.*, 2017)

2.3.3.2 Cellulose nanofibers

Nanocellulose materials, like CNFs, are polysaccharide biopolymers derived from wood, cotton, hemp, sugar beet, or from various similar kind of sources. CNFs (Figure 6) are produced from native cellulose by top-down methods involving enzymatic, chemical, and/or physical methodologies. (Lin, N. and Dufresne 2014) To prepare completely individualized cellulose nanofibers, 2,2,6,6-tetramethylpiperidine-1-oxyl (TEMPO) radical -mediated oxidation step is combined with the homogenization process (Saito *et al.*, 2007).

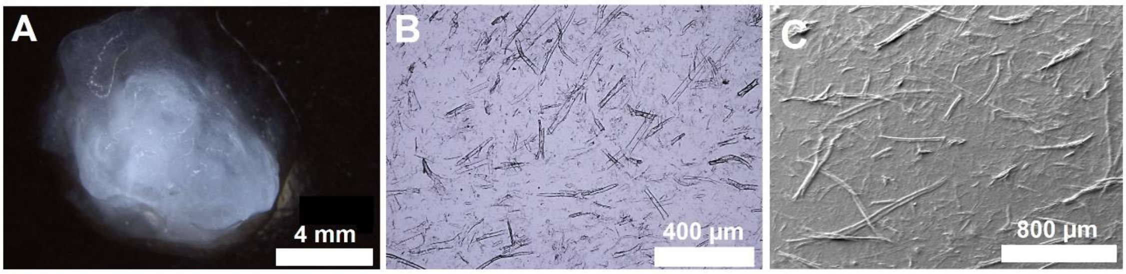

Figure 6. *Structure of cellulose nanofibers. Macroscopic image from CNFs (A), light microscope image (B) where the CNFs are stained by crystal violet for better visualization and scanning electron microscope image (C) from CNFs after coating with gold. Provided and modified from: Ahmad Rashad Saad Mohamed Elsebahy, Department of Clinical Dentistry, University of Bergen.*

CNFs have gained much attention for their use in tissue engineering applications, because of their suitable characteristics, such as fiber morphology, high specific surface area, rheological shear-thinning properties, alignment and orientation, mechanical reinforcement, surface chemical reactivity, and lack of toxicity (Lin, N. and Dufresne 2014). As a result, CNFs have emerged as an important component in several bioink formulations for 3D bioprinting (Ojansivu *et al.*, 2019; Müller *et al.*, 2017; Wang, K. *et al.*, 2016; Markstedt *et al.*, 2015; Lou *et al.*, 2014). In 3D bioprinting, CNFs can improve the printability and flow of the bioink by modifying viscosity (Wang, K. *et al.*, 2016; Markstedt *et al.*, 2015). This is advantageous when working with high viscosity bioinks, which have for instance high dry matter compositions. Mechanical properties, biodegradability, and cytocompatibility of CNFs have also been examined to be suitable for 3D bioprinting and cell culture (Ojansivu *et al.*, 2019; Markstedt *et al.*, 2015; Lou *et al.*, 2014).

CNFs have been used in multiple alginate-based bioinks designed for bone or cartilage applications (Ojansivu *et al.*, 2019; Müller *et al.*, 2017; Nguyen *et al.*, 2017; Markstedt *et al.*, 2015). Ojansivu *et al.* used alginate and gelatin -based bioink with CNFs and BaG for bioprinting of bone cells. CNFs were found to improve the rheological properties and printability of the bioink when extrusion 3D bioprinting was used. (Ojansivu *et al.*, 2019) Müller *et al.*, Nguyen *et al.*, and Marksted *et al*. all used nanocellulose-alginate bioink in 3D bioprinting for cartilage applications. All three studies found printing properties and shear-thinning behaviour of the nanocellulose beneficial in their bioink composition. (Müller *et al.*, 2017; Nguyen *et al.*, 2017; Markstedt *et al.*, 2015)

2.3.4 Bioinks for 3D bioprinting of bone

An ideal bioink in BTE should be osteoconductive, osteoinductive, and the cells embedded to the ink should have osteogenic potential (Tozzi *et al.*, 2016). Osteoconductivity and osteoinductivity are usually ensured in bone 3D bioprinting by using bioactive additives in the bioink, such as nHA, bone morphogenetic protein 2, or vascular endothelial growth factor (VEGF) (Ashammakhi *et al.*, 2019). As with other bioinks, the viscosity, shear-thinning properties, and crosslinking method of the bioinks for bone tissue applications should be optimal, to ensure good printability with the printing modality in use and optimal mechanical properties for the construct.

Great part of the bone tissue consists of hard mineralized matrix which can be mimicked by using harder polymers and ceramics together with cells in the bioinks (Matai *et al.*, 2020). Generallly ceramic phase, like nHA particles, is added to the multicomponent bioink, as ceramics are biocompatible materials and mimic the natural bone (Midha *et al.*, 2019; Zhou *et al.*, 2016; Wüst *et al.*, 2014). Adding ceramic phase like nHA particles to the hydrogels provides nucleation sites in the bioinks, which is beneficial, as the hydrogels alone are not able to form mineralized matrix typical for bone (Gkioni *et al.*, 2010). In other words, nHA supports bone growth and osseointegration in the bioink and can also increase osteogenic differentiation of the used cells (Gungor-Ozkerim *et al.*, 2018; Wang, Xiao-Fei *et al.*, 2016). High viability and proliferation of hMSCs has been reported when nHA was used in bioinks or in biomaterial inks seeded afterwards with cells (Zhou *et al.*, 2016; Wang, Xiao-Fei *et al.*, 2016; Wüst *et al.*, 2014). Ceramic phase in a bioink also modifies the stiffness and mechanical strength of the soft hydrogel precursors usually used in bioinks closer to the natural bone (Midha *et al.*, 2019). Concentrations of nHA from 1.0 to 8.0 % (w/v) have been reported in bioinks developed for 3D bioprinting for bone applications (Wang, Xiao-Fei *et al.*, 2016; Wüst *et al.*, 2014; Gao *et al.*, 2014).

Besides nHA, other mineral components used in 3D bioprinting targeted to bone tissue, are for instance nanoclay and BaG (Cidonio *et al.*, 2020; Cidonio *et al.*, 2019; Ojansivu *et al.*, 2019; Ahlfeld *et al.*, 2017; Gao *et al.*, 2014; Wang, Xiaohong *et al.*, 2014). Ojansivu *et al.* used alginate and gelatin based bioink in a study where the effect of CNFs and BaG to rheological properties of the bioink and for bone cells were studied. Osteoblast-like cells and hBMSCs were extrusion bioprinted, and BaG was found to induce osteogenic differentiation of the cells based on alkaline phosphatase -activity measurements. Interestingly, Saos-2 cells were more vulnerable to the bioprinting process in the presence of viscosity increasing BaG and had lower cell viability after 3D bioprinting than hBMSCs had. (Ojansivu *et al.*, 2019) Wang *et al.* also studied the effect of BaG on cell growth and mineralization of Saos-2 cells on alginate/gelatin bioink and found that BaG increased the proliferation and mineralization of the 3D bioprinted cells (Wang, Xiaohong *et al.*, 2014). Gao *et al.* used poly(ethylene glycol)dimethacrylate (PEGDMA) based bioink together with BaG or nHA and compared these nanoparticles and their effect on hBMSCs. Higher cell viability and osteogenesis was observed in hBMSCs 3D bioprinted with PEGDMA-nHA than in BEGDMA-BaG 3D bioprinted hBMSCs. (Gao *et al.*, 2014)

Bioinks having GelMA as a backbone with mineral components are also used in 3D bioprinting for bone applications (Cidonio *et al.*, 2019; Byambaa *et al.*, 2017). Cidonio *et al.* observed that use of synthetic nanoclay Laponite® in GelMA-based bioink significantly enhanced bioprinted hBMSCs viability, proliferation and osteogenic capacity when compared to bioink without it. 3D bioprinting was done with extrusion-based bioprinter and crosslinking with UV light, together with photoinitiators Ru and SPS. (Cidonio *et al.*, 2019) Byambaa *et al.* used silicate nanoparticles in GelMA bioink together with hBMSCs and blood-derived human umbilical vein endothelial cells, to create osteon resembling bone construct with perfusable vascular lumen. Additionally, VEGF gradient was added to support angiogenesis. Extrusion 3D bioprinting and photo-crosslinking with UV light and IC were used to fabricate the construct, which held a stable structure for 21 days *in vitro*. Silicate nanoparticles in the construct supported osteogenesis, and VEGF in turn supported the formation vasculature. (Byambaa *et al.*, 2017) Couple of studies have also utilized GelMA bioinks for 3D bioprinting of bone applications without ceramics (Lim *et al.*, 2016; Levato *et al.*, 2014).

3. AIMS OF THE THESIS

In this thesis, the aim was to develop a multicomponent bioink for extrusion-based 3D bioprinting for bone applications and to investigate the effect of nHA in the composition. The base components of the bioinks were GelMA, gelatin, and wood-derived CNFs. The nHA concentrations were chosen to be 1.0, 3.0 and 5.0 % (w/v) based on earlier studies and literature search (Wang, Xiao-Fei et al., 2016; Wüst et al., 2014; Gao et al., 2014). Additionally, the range of nHA concentrations was chosen to represent both a low (1.0 % w/v) and a high (5.0 % w/v) nHA compositions. To demonstrate possible trends in material behavior, a 3.0 % w/v nHA concentration was also investigated in the material characterization studies.

Different concentrations of nHA having biomaterial inks were characterized for their printability and the biological responses of hBMSCs embedded in the developed bioinks were evaluated. It was hypothesized that high concentration of nHA would increase the viscosity of the bioink, affecting negatively on the printability. High viscosity was also expected to cause high shear stress on cells while 3D bioprinting leading to decrease in cell viability. On the other hand, the increased concentration of nHA was expected to induce proliferation and osteogenic differentiation of hBMSCs as nHA has been studied to support bone growth and osseointegration in the bioink and increase osteogenic differentiation of the used cells (Gungor-Ozkerim *et al.*, 2018; Wang, Xiao-Fei *et al.*, 2016).

4. MATERIALS AND METHODS

The workflow of the project is illustrated in Figure 7. First, the biomaterial inks, IC concentration, 3D printing process, and crosslinking were optimized. The optimized biomaterial inks were characterized for their material properties. Next, the biological characterization was done. It composed of 3D bioprinting pilot, where hBMSCs were bioprinted in one bioink to optimize the crosslinking conditions in terms of cell viability and proliferation. After 3D bioprinting pilot, actual 3D bioprinting of nHA bioink groups was done and the effect of nHA on hBMSCs was evaluated.

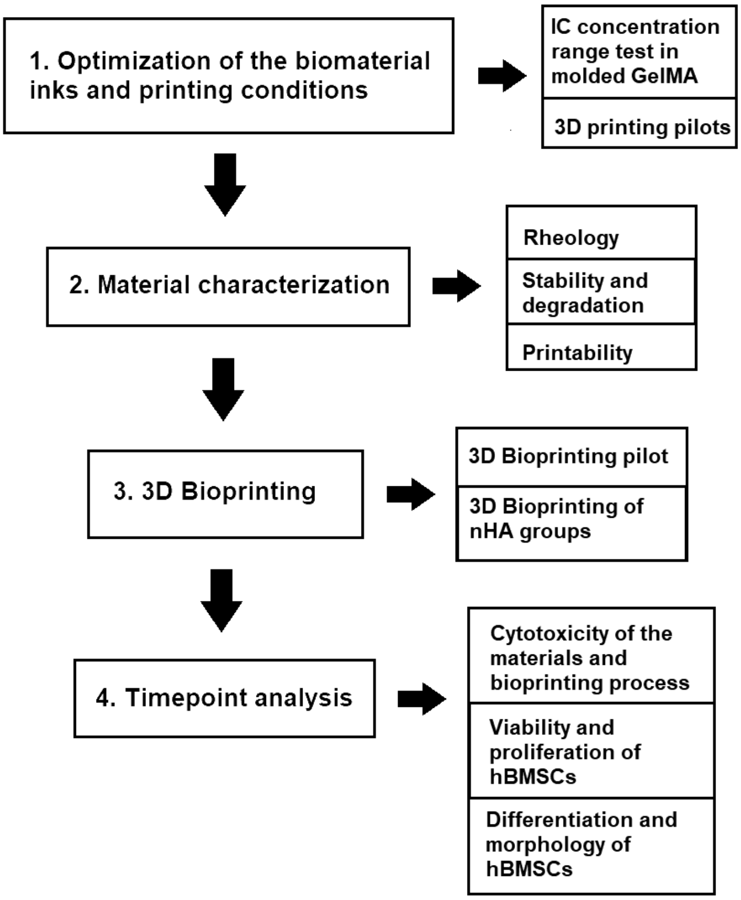

Figure 7. *Workflow of the project.*

The biomaterial ink groups and their component concentrations before the optimization are presented in Table 3. The base components of the biomaterial inks were GelMA (60 % degree of substitution, Sigma Aldrich, USA), gelatin (porcine skin, Sigma Aldrich, USA), and wood-derived CNFs (gel stock, 1 % solid content, TEMPO-oxidized, RISE PFI, Norway). In order to utilize the photo-crosslinking properties of GelMA, photoinitiator IC (TCI Chemicals, China) was chosen for initiation of crosslinking of the inks with UV light. The base component concentrations, as presented in Table 3, were chosen based on earlier studies and literature review (chapter 2.3.3.1, Tables 1 and 2).

Table 3. *The biomaterial ink groups and their component concentrations (% w/v) before the optimization.*

Group name	Biomaterial ink components (% w/v)				
	CNFs	GelMA	Gelatin	nHA	IC
0% nHA	0.5	4.0	4.0	0.0	0.05 – 0.3
1% nHA	0.5	4.0	4.0	1.0	0.05 – 0.3
3% nHA	0.5	4.0	4.0	3.0	0.05 – 0.3
5% nHA	0.5	4.0	4.0	5.0	0.05 – 0.3

For mineralization and to support osteogenic differentiation of hBMSCs, a range of nanohydroxyapatite powder (Sigma Aldrich, USA, <200 nm particle size) concentrations were chosen to be tested. The nHA concentrations were chosen to be 1.0, 3.0 and 5.0 % (w/v). In addition, a biomaterial ink without nHA was utilized as control. Total of 4 groups were formed and named based on the nHA concentration of the group (Table 3).

4.1 3D bioprinter, loading of the bioinks, and 3D designs

The 3D bioprinter used in this project was 3D-Bioplotter Manufacturer Series from EnvisionTEC GmbH (Germany), which is an extrusion-based 3D bioprinter (Figure 8). 3D-Bioplotter has a motor head with built-in camera and platform height control. Building platform temperature of the device can also be controlled. Five materials can be utilized in a single structure, since the device has 5 slots for printing heads (Figure 9 (A)). In this project, low-temperature print head (0 °C – 70 °C) was used for printing of the bioinks. In addition to low-temperature dispensing head, 3D-Bioplotter has high-temperature (30 °C – 250 °C) print heads available for 3D bioprinting. 3D-Bioplotter is connected to a computer (Figure 9 (B)) by which it can be controlled, and to a temperature controller of the printing platform (Minichiller 300, Huber, USA) (Figure 9 (C)). The controlling software for 3D-Bioplotter is VisualMachines, which is used during printing to set material and UV program parameters and to define inner pattern design, for example. Perfactory RP software is used to prepare and convert *STL* files for VisualMachines.

Figure 8. *3D-Bioplotter Manufacturer Series. The printing platform can be seen at the center of the device and the motor head with the camera and platform height control above it.*

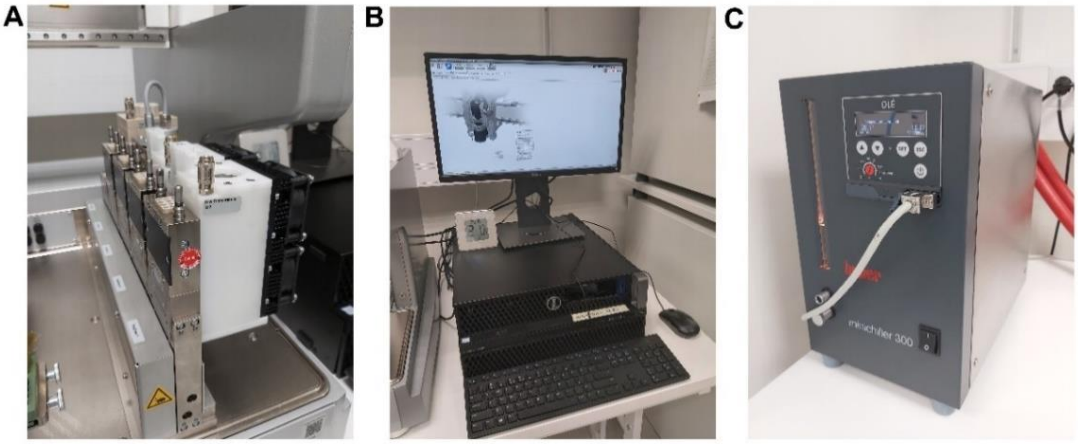

Figure 9. *Additional printing equipment of Envisiontec 3D-Bioplotter. Different printing heads of the 3D-Bioplotter (A). The 3D bioprinter was connected to computer (B) from where it was controlled. The temperature controller of the printing platform (C).*

UV curing head (365 nm) of the 3D-Bioplotter was used for UV crosslinking of the biomaterial inks and bioinks (Figure 10). Starting parameters for UV crosslinking programs were set on VisualMachines UV programs tab. UV program of the 3D-Bioplotter can use either continuous or single projection UV light. In both cases, the UV light exposure comes after each printed layer. With single projection, UV light is placed on center top of the structure. With continuous projection UV head moves over the structure and speed of the movement can be adjusted. In addition to projection type, for example UV light exposure time can be adjusted. The intensity of the UV light can be adjusted by changing the height of the UV head. If UV program is selected to the project on VisualMachines, the dispensing head is changed automatically to UV head after printing each layer. Used UV program parameters in each experiment are described more detailed in later chapters.

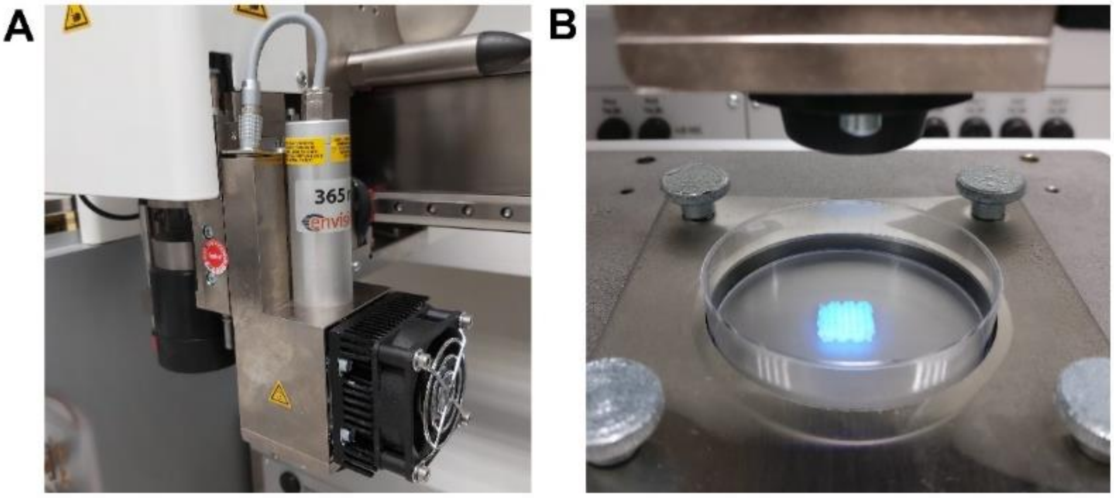

Figure 10. *The UV head of the printer (A) was used as a UV light source in crosslinking of the hydrogels. Structures were printed onto sterile Petri dishes and UV crosslinked after each layer (B).*

In this study, the preparations, mixing and handling of biomaterial inks and bioinks was kept constant throughout the experiments unless otherwise stated. Figure 11 illustrates the workflow from the biomaterial ink mixing to the ink transfer to the 3D-Bioplotter. Mixing of the biomaterial inks (Figure 11 (A)), addition of the photoinitiator and addition of the hBMSCs (if applicable) (Figure 11, (B)), is described later in chapter 4.3. After these work phases, the biomaterial ink or bioink was moved to sterile syringe barrel (Optimum® Syringe Barrels, clear, 30cc: Nordson EFD, USA) provided with 21G blunt needle (Optimum® 21G blunt needle 12.7 mm, 0.5": Nordson EFD, USA) (Figure 11 (C)). Syringe barrel piston (Optimum® Pistons, red: Nordson EFD, USA) was carefully put on its place and all air from the syringe barrel was extruded. The loaded syringe barrel was transferred to 4 °C for 18 minutes and then placed into the low-temperature dispensing head of the bioprinter with air lock adapter (Optimum® Adapter (air lock adapter), Nordson EFD, USA) to reach desired temperature (Figure 11 (D)). The material parameters were set in the VisualMachines Material Editor tab and the material was assigned for the low-temperature head of the printer. Before starting the printing process, the biomaterial ink or bionk was always stabilized at the printer for 30 minutes.

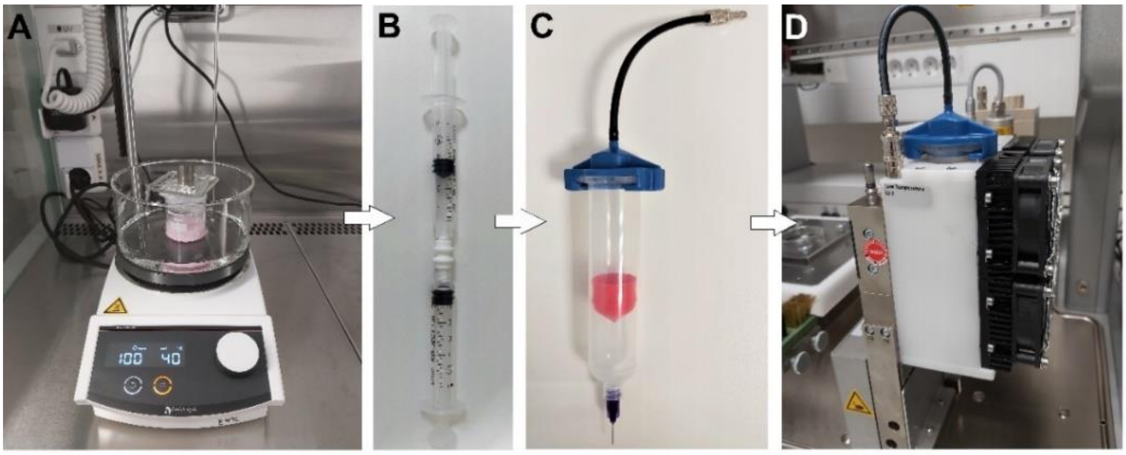

Figure 11. *Work phases before 3D bioprinting or printing. Mixing of the biomaterial inks (A). Mixing of the photoinitiator and the hBMSCs (if applicable) to the biomaterial inks (B). The loading of the ink into a printing barrel syringe, with a piston (red part) and printing needle (purple) (C). Air lock adapter (blue) was connected with syringe barrel when it was transferred into the dispensing head of the bioprinter (D).*

The 3D designs used in this project are presented in Figure 12. The most used design was a cuboid structure, made, modified, and translated into printable file by using Perfactory RP -software of the printer. In Perfactory RP, first, the dimensions of the 3D design were set to 10x10x1.56 mm (width x length x height). The 3D design was then set to zero level and centered on the printing platform. As per the 3D Bioplotter’s manual, the optimal slicing of an object is approximately 80 % of the inner diameter of the printing needle, and as the 21G printing needle with 510 µm inner diameter was used, the cubic design was sliced by using 400 µm slicing. Next, the design was saved as *Bordland Package Library (BPL)* -file in order to open it in VisualMachines. The inner pattern of the structure was designed at VisualMachines’ pattern design tab as a lattice structure with 1.4 mm distance between strands without contour (Figure 13). This cuboid design was used in all experiments unless otherwise stated.

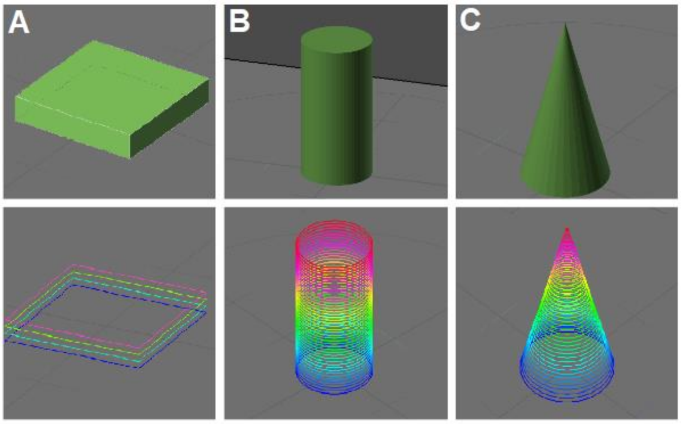

Figure 12. *3D designs (upper row) and their slicing (lower row). 10 x 10 x 1.56 mm cuboid structure mainly used in the project (A). 10 x 10 x 20 mm cylinder and cone structures used in printability studies (B, C). Images captured from Perfactory RP software*

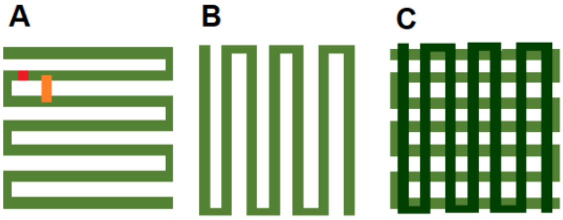

Figure 13. *Schematic presentation of the inner pattern design of the 10 x 10 mm lattice structure. First layer of the structure (A). Designed filament thickness is marked as red and distance between strands as orange. Second layer (B) and lattice structure after two or more layers are printed (C).*

In printability studies the used 3D designs were cuboid, cylinder, and cone structures (Figure 12 (B and C)). Table 4 presents the dimensions of the 3D designs used in printability studies and whether they included inner pattern design or contour or not. Same 3D design handling process, described in previous paragraph, was made except 450 µm slicing was used. The inner pattern of the cuboid structure was the same one presented in previous paragraph. With cylinder and cone structures, inner pattern was not used, only contour was assigned to the projects, since the plan was to print hollow structures.

Table 4. *Dimensions of the 3D designs used in printability studies.*

Design	**width (mm)**	**length (mm)**	**height (mm)**	**inner pattern**	**contour**
cuboid	30.0	30.0	1.56	yes	no
cylinder	10.0	10.0	20.0	no	yes
cone	10.0	10.0	20.0	no	yes

Finally, before starting a printing procedure, the created material program, pattern design, and UV program were combined into project in VisualMachines. All 3D bioprinting in this project was done with a cooled 4 °C platform and on to a sterile 60 mm diameter Petri dishes (60 x 15 mm Dish, Nunclon™ Delta, Thermo Fisher Scientific, USA). To minimize contaminations the printing platform and its surrounding area were cleaned with 70 % ethanol before and after each printing session. The printing needle was always calibrated before the printing process was started, and the purging protocol was used to ensure that the needle was not clogged. Purging was done above the purge station of the 3D Bioplotter by applying pressure to test whether the material came out from the nozzle.

4.2 Optimization of the biomaterial inks and printing conditions

In order to develop a stable bioink with efficient crosslinking properties the biomaterial inks were optimized on three fronts: ink composition, crosslinking, and printing parameters. The biomaterial ink groups and the component concentrations, presented in Table 3, were used as a starting point. The optimization phase started with a simple GelMA casting pilot with different concentrations of IC. After that, 3D printing pilots with 1 % and 5 % (w/v) nHA biomaterial ink groups were executed. Casting pilot and 3D printing pilots with 1 % and 5 % nHA biomaterial inks were made once. All concentrations are presented as weight by volume percentage.

4.2.1 Optimization of the IC concentration in molded GelMA

In pursuit of finding the correct IC concentration, the aim was to find the lowest functional IC concentration for crosslinking of the biomaterial inks, as excess IC is cytotoxic to cells (Stratesteffen *et al.*, 2017; Lim *et al.*, 2016). 4 % GelMA concentration was used in IC concentration range tests and IC concentrations of 0.05 %, 0.10 %, 0.15 %, 0.2 %, and 0.3 % were chosen to be evaluated (Table 5).

Table 5. *IC concentration range in the optimization experiment.*

	IC (w/v %)	IC (g)
4 % GelMA solution, 1ml	0.3	0.003
	0.2	0.002
	0.15	0.0015
	0.1	0.001
	0.05	0.0005

First, gelatin mold for castings was prepared. A gel of 5 % gelatin dissolved in distilled phosphate-buffered saline (DPBS) was cast into a petri dish with a diameter of 60 mm and gelated on ice. After gelation, small round holes were punched in the gelatin mold. 4 % GelMA in DPBS was prepared in water bath (50 °C) with a magnetic stirrer for 30 minutes. GelMA solution was then divided into 5 samples and stained with crystal violet (Merck, Germany) for visibility. Next, IC stock solutions of 0.1 g/ml were prepared. Two different stocks were prepared, one by dissolving IC into DPBS and the other by using 99.5 % ethanol (Altia Oyj, Finland) as a solvent. In both cases, IC was added to solvents and heated to 50 °C in a water bath and vortexed. As per quick comparison and based on a literature review (Tables 1 and 2), ethanol was the best at dissolving IC and was therefore used in IC stock solution preparations onwards. Different volumes of IC stock solution were added to 4 % GelMA samples to create IC concentration range from 0.05 % to 0.3 %. Since IC is light sensitive, both the stock solution and 4 % GelMA with IC were protected from light.

Total of four different experiments were conducted with 4 % GelMA with different concentrations of IC (Table 6). In general, 4 % GelMA samples with different concentrations of IC were cast into the gelatin mold on ice (~100 µl / cast). From each IC concentration, three replicates were cast (Figure 14). After that, the mold was either kept on ice or in room temperature (RT) and exposed to UV light (UVL-54 All-In, Promed, Germany). UV distance from samples was approximately 6.5 cm. All variations in temperatures and exposure times are listed in Table 6.

Table 6. *Overview of the IC concentration range experiments.*

Experiment	IC (% w/v) in sample(s)	UV exposure (min)	Environment
1	0.05	1.5	On ice
	0.10	3.5	RT
	0.15	4.5	
	0.2	5.5	
	0.3		
2	0.3	6	On ice
3	0.3	5	On ice, after UV exposure moved to heat plate at 35°C
4	0.2 0.3	6	On ice, after UV exposure moved to heat plate at 35°C

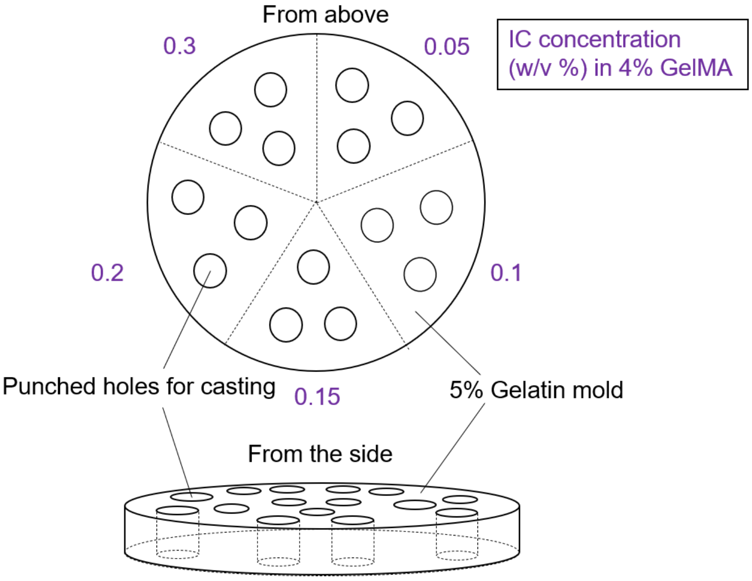

Figure 14. *The IC concentration range test setup in the casting.*

In last three experiments (Table 6) only 0.3 % and 0.2 % IC concentration having 4 % GelMA were examined. In experiments 3 and 4, after the UV exposure the samples were lifted from the gelatin mold and moved to heat plate at 35 °C to see if the samples were permanently crosslinked. In addition to cast samples, droplets of 4 % GelMA with different concentrations of IC were also pipetted to a plastic plate which were then exposed to UV light at RT (280 seconds) and at the other experiment, on ice (5 minutes).

4.2.2 Optimization of 3D printing and crosslinking parameters

To find the optimal printing and crosslinking parameters, 3D printing pilots were conducted with both 1 % and 5 % nHA containing biomaterial inks (Table 3). Based on the results obtained from the previous optimization steps, 0.3% IC concentration was chosen for 3D printing pilots. First 3D printing pilot was done with 1 % nHA biomaterial ink. Mixing the components of the biomaterial inks was done in a water bath using heating Heidolph™ MR Hei-Tec magnetic stirrer (Germany). Before use in each experiment, CNFs were sterilized by autoclaving and the loss of water during the sterilization was compensated with ultra-pure water. Sterilized 1.01 % CNFs were mixed (1.5 h, 200 rpm, 60 °C) and water was slowly added to CNFs in mixing. Next, Alpha Minimum Essential Medium (αMEM) (1X) (Gibco, Thermo Fisher Scientific, USA) supplemented with 1 % Penicillin-Streptomycin (P/S) (Lonza / Biowhittaker, Thermo Fisher Scientific, USA) and prewarmed to 37 °C, was added slowly drop by drop while mixing. GelMA, gelatin and nHA were always UV purified in the laminar hood for 1 hour before use. Sterilized GelMA was added while mixing and water bath temperature was decreased to 40 °C. The biomaterial ink was mixed for 2 hours at 100 rpm at 40 °C. After that, sterilized nHA was added while mixing at 200-300 rpm. The biomaterial ink was further mixed for 1 hour, 100 rpm at 40 °C and after that stored up to 48 hours at 4 °C.

Before 3D printing, the 1% nHA biomaterial ink was first prewarmed up to 37 °C while mixing at 100 rpm and then cooled down to 27 °C, to find the suitable printing temperature. At 27 °C the biomaterial ink was still presenting a very low viscosity or watery consistency making it non-printable. To enhance the printability of the biomaterial ink, 4 % of gelatin was mixed into the biomaterial ink at 37 °C, 100 rpm for 1 hour. Next, IC stock solution of 0.12 g/ml was prepared in 99.5 % ethanol and sterile filtered (Acrodisc® PF Syringe Filters with Supor® Membrane, Sterile - 0.8/0.2 µm, 32 mm, Pall corporation, USA). Adequate volume of stock solution was moved to the 1 % nHA biomaterial ink to achieve IC concentration of 0.3 %. IC was mixed to the biomaterial ink for 1 minute at 100 rpm.

Second 3D printing pilot was executed with 5 % nHA biomaterial ink and based on described pilots, with alterations in the procedure. First, the mixing order of the components was changed. Next, a 32 % stock gelatin solution was prepared in DPBS for 2 hours at 100 – 300 rpm at 70 °C. At the same time with mixing, one hour UV exposure was provided. The 32 % gelatin stock was stored at 4 °C up to three weeks.

The biomaterial ink with 5 % nHA was prepared by first mixing sterilized CNFs as with the 1 % nHA biomaterial ink. Then ultrapure compensation water was added while mixing and CNFs were further mixed (30 min, 100 rpm, 40 °C). Adequate volume of 32 % (prewarmed at 37 °C) gelatin stock was added to the biomaterial ink and mixed (1 h, 100 rpm, 40 °C). Next, sterilized GelMA was added to the biomaterial ink and mixed (10 min, 100 rpm, 40 °C). Sterilized nHA was mixed first with 1 ml of prewarmed αMEM with 1 % P/S and then the mixture was added slowly drop by drop to the biomaterial ink while mixing. The 5 % nHA biomaterial ink was further mixed 2.5 hours at 100 rpm at 40 °C and then stored at 4 °C.

IC stock solution of 0.12 g/ml was prepared as described earlier, but this time in 75 % ethanol as it worked as well as 90.5 % ethanol as a solvent. The project was continued with the sterile filtered IC stock dissolved in 75 % ethanol. IC was added to the 5 % nHA biomaterial ink and mixed the same way as with the 1 % nHA biomaterial ink. Before actual 3D printing, same temperature treatment was provided to the 5 % nHA biomaterial ink as with the 1 % nHA biomaterial ink.

3D printing of 1 % nHA and 5 % nHA biomaterial inks with 0.3 % IC was done as presented in chapter 4.1. Shortly, the biomaterial inks were transferred into a printing syringe barrel, kept at 4 °C for 18 min and at 27 °C for 30 min in the low-temperature dispensing head of the printer. All biomaterial ink transfer was done by using

MICROMAN® E M1000E positive displacement pipette, along with disposable capillary piston (CP) tips (Gilson, USA). 3D printing with the 1 % nHA biomaterial ink was done by using various speeds (around 9 – 10 mm/s) and pressures (from 1.0 to 1.3 bar). For UV crosslinking, both single and continuous projections were attempted. Continuous projection was tested by 3D printing couple 30 x 30 mm three layers having cuboid lattice structures. UV light beam distance and intensity in single projection were either 30.2 mm with 64 mW/cm^2 or 44.5 mm with 40 mW/cm^2. Exposure times ranging from 10 s to 105 s per layer were tested for crosslinking of the printed structures. In Table 7, all combinations for single projection UV crosslinking are summarized. After 3D printing and crosslinking, the structures were moved from petri dishes to 12-well plates (Nunc™, Thermo Fisher Scientific, USA) with DPBS. After that DPBS was changed to αMEM with 1 % P/S (1 ml / well) and the structures were incubated at 37 °C.

Table 7. *Combinations for single projection UV crosslinking in 3D printing pilots.*

Group	UV distance from last layer (mm)	UV beam intensity (mW / cm^2)	UV exposure times (s)
1 % nHA	30.2	64	45, 60, 75, 90, 105
	44.5	40	10, 20, 30, 45, 60
5 % nHA	30.2	64	45, 60, 75, 90

With the 5 % nHA biomaterial ink, 9.5 mm/s speed and pressures from 1.1 bar to 1.4 bar were used. UV light distance and intensity in single projection program were 64 mW / cm^2 and 30.2 mm and UV exposure times for crosslinking varied from 45 s to 90 s per layer (Table 7). UV exposure times from 45 to 90 s after each printed layer were chosen for further studies, since 45 s UV exposure time was the shortest working one in pilots. UV beam intensity and distance were chosen to be 64 mW / cm^2 and 30.2 mm in all coming 3D printing and bioprinting experiments. Printing temperature was constantly changed during printing process, ranging from 23 to 26 °C. As with the 1 % nHA 3D printing pilot, the printed structures were moved to 12-well plates and kept at 37 °C in αMEM with 1 % P/S (1ml / well). 3D printed structures from both printing pilots were incubated for 2 weeks and imaged at several timepoints to follow the stability of the printed structures. This was done for 3D printed structures which were crosslinked by using 45 to 105 s UV exposure time with 30.2 mm distance and 64 mW / cm^2 intensity. Imaging of the structures was always done with Galaxy A70 android phone (Samsung, South Korea).

4.3 Preparation of the biomaterial inks and bioinks

After 3D printing pilots, final concentrations of the developed biomaterial ink components were decided. The concentration of CNFs was kept at 0.5 % in all groups. The concentrations of gelatin and GelMA were raised from 4.0 % to 5.0 % to improve the printability of the biomaterial inks and to stabilize the printing temperature. 0.3 % IC concentration was chosen to be adequate for crosslinking with UV light. Table 8 presents the optimized biomaterial ink groups and their component concentrations.

Table 8. *The developed biomaterial inks and their component concentrations (% w/v).*

Group name	**Biomaterial ink components (% w/v)**				
	CNF	**GelMA**	**Gelatin**	**nHA**	**IC**
0 % nHA	0.5	5.0	5.0	0.0	0.3
1 % nHA	0.5	5.0	5.0	1.0	0.3
3 % nHA	0.5	5.0	5.0	3.0	0.3
5 % nHA	0.5	5.0	5.0	5.0	0.3

Based on optimization of the biomaterial inks and printing conditions, final mixing protocol of the biomaterial inks was specified. Figure 15 presents the optimized mixing protocol of the biomaterial inks. The presented stirring times for each component are averages from all mixings. In earlier chapter 4.1, mixing setting is presented in Figure 11 (A). From now on, all biomaterial inks or bioinks were prepared the same way either for material characterization studies or for 3D bioprinting. Autoclaved CNFs were moved to sterilized 50 ml beaker glass and mixed for 1 hour at 60°C. Adequate volume of ultrapure compensation water was slowly added after CNFs had been mixed for about 15 minutes. After CNFs were mixed, adequate volume of earlier prepared 32 % (prewarmed to 37 °C in water bath) gelatin stock in DPBS was added to achieve 5 % gelatin concentration in the biomaterial ink. CNFs and gelatin were mixed for 1 hour and 15 minutes at 40°C. Next, GelMA was added, and the biomaterial ink was mixed for 1 hour at 40°C. After GelMA addition, nHA was mixed in αMEM with 1 % P/S (prewarmed to 37 °C in water bath) and the solution was added slowly, drop by drop, to the biomaterial ink while mixing at 100 rpm. In case of 0 % nHA biomaterial ink, only warm αMEM with 1 % P/S was added without nHA. After medium and nHA addition, the biomaterial inks were always mixed at least for 1 hour at 40°C. Readymade biomaterial inks were stored at 4 °C up to 3 days before they were used either for material characterization or for 3D bioprinting.

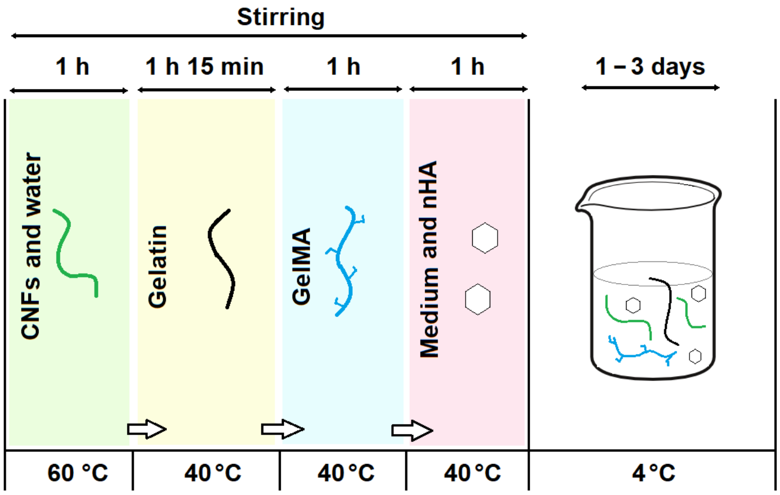

Figure 15. *Schematic representation of preparation and mixing ptotocol of the biomaterial inks. Only medium without nHA was added in the last phase to the 0% nHA biomaterial ink.*

Figure 11 in chapter 4.1. presents the workflow after mixing of the biomaterial inks. Before printing, the biomaterial inks were first prewarmed at 37°C water bath with constant stirring for at least 1 hour. IC stock solution (0.12 g/ml) was prepared in 75 % ethanol. Adequate volume of prewarmed biomaterial ink was moved to 5 ml KD-JECT® III syringe (KDM® KD Medical GmbH, Germany) which was connected with female-female luer lock (Health Care Logistics, USA) to another similar syringe (Figure 11 (B)). Adequate volume of prepared IC stock solution was added to the same syringe with the biomaterial ink so that 0.3 % IC concentration was achieved in the ink. When bioink was prepared for 3D bioprinting, the cell suspension was also added to the syringe. The volume of cell suspension added to the syringe was proportioned to the volume of the bioink to be printed (50 µl cell suspension / 1 ml of the bioink). After all components were added to 5 ml syringe, excess air was removed from the syringes and the biomaterial ink or bioink was carefully mixed by moving the pistons in and out for 1 minute. After mixing, the biomaterial ink or bioink was moved to sterile printing syringe barrel with 21G blunt needle as described in chapter 4.1 (Figure 11 (C)). The biomaterial inks prepared for rheological measurements or printability studies were not syringe mixed with IC, as presented in this chapter, since there was no need to crosslink them.

4.4 Characterization of the biomaterial inks

After optimization of the biomaterial inks and printing conditions, characterization of the biomaterial inks was done. In characterization rheological properties, stability, and printability of the biomaterial inks was studied. Characterization was done for all four biomaterial inks (Table 3).

4.4.1 Rheological characterization of the biomaterial inks

Rheological measurements focused on the viscosity, temperature dependency, and shear thinning properties of the developed biomaterial inks. Rheological characterization was done using Discovery HR-2 hybrid rheometer (TA Instruments, USA) with 20 mm parallel geometry plate (Figure 16). Figure 17 illustrates the sample setup at the rheometer.

Figure 16. *Discovery HR-2 hybrid rheometer.*

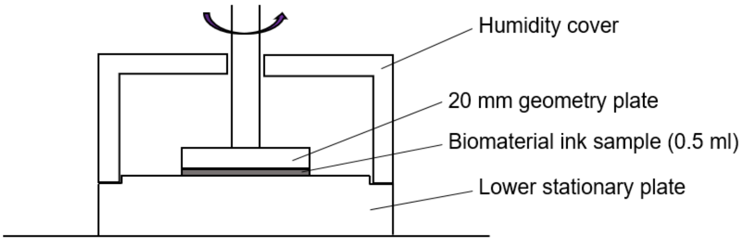

Figure 17. *Schematic illustration of the sample setup at the rheometer. Adapted from:* (Meakin *et al.*, 2003).

For each biomaterial ink group, a “temperature ramp” from 37 to 20 °C with shear rate 1.0 1/s and a “flow sweep” at 26 °C with shear rate from 0.01 to 300.0 1/s were executed. With all groups, the sample size was 500 µl of the biomaterial ink and the measurement was repeated 4 times. The biomaterial inks were always prewarmed at 37 °C before rheology measurements for at least 45 minutes. During the rheological measurements, a humidity cover was used, and water droplets were pipetted around the sample to prevent drying of the samples during the measurements.

4.4.2 Stability of the biomaterial inks

Stability of the biomaterial inks in incubation after 3D printing and crosslinking was estimated by incubating printed structures of all groups in DPBS with 1 % P/S at 37 °C. Study included imaging of the structures and the release rate of gelatin from the structures was studied by analyzing collected DPBS 1 % P/S samples with colorimetric Bicinchoninic Acid (BCA) assay. Degradation study was made once.

The biomaterial inks were handled, and 3D printing was done as described in earlier chapters of the materials and methods. 3D printing was done at 26 °C and for crosslinking, 45 s UV exposure time was used after each printed layer. Printed structures were moved into 12-well plates and provided with DPBS. The samples were incubated at 37 °C and followed for 14 days. During that time images were taken and DPBS 1 % P/S samples (1 ml) collected on days 1, 3, 7, 10, and 14. On each timepoint day, five replicates were collected and stored to -80 °C. After imaging of the structures and collecting samples, new DPBS 1 % P/S was changed to the wells.

The release of gelatin from printed structures was studied by analyzing collected DBPS 1 % P/S samples. Commercial Pierce^{TM} BCA Protein Assay Kit (Thermo Fisher Scientific, USA) was used. Before pipetting the samples on 96-well plates (Nunc™ MicroWell™ 96-Well, Thermo Fisher Scientific, USA), they were thawed on ice, incubated for 15 minutes at 37 °C, vortexed, and finally spun shortly to flush down the released nHA. Standard curve was prepared in triplicate for each plate and DPBS 1% P/S was used as a diluent. All samples were analyzed in technical replicates. Wallac Victor^2 1420 Multilabel counter (PerkinElmer, USA) was used for absorbance measurement (544 nm) of the reaction plates.

4.4.3 Printability studies for the biomaterial inks

The printability studies of the biomaterial inks included imaging of the structures and evaluation in a filament formation test, filament spreading, and buildability. Instead of IC, filtrated 0.1 % crystal violet in ultrapure water was mixed to the biomaterial inks for better visualization (5.7 µl / 1 ml of the biomaterial ink). 3D printing was done at 26 °C and the structures were used without crosslinking. Table 9 summarizes used printing pressures and speeds in printability studies. Three different 3D designs, presented in chapter 4.1, were used in printability studies. The results were recorded with a Canon EOS 550D camera (Japan) and the most representative ones are presented in the results.

Table 9. *3D printing pressures and speeds used in printability studies of the biomaterial inks.*

Group	0% nHA	1% nHA	3% nHA	5% nHA
Pressure (bar)	0.8 – 1.0	1.3 – 1.4	1.5 – 1.6	2.1
Speed (mm/s)	11.5	11.5	10.3	13.3

The filament formation was studied by extruding stable filaments with all biomaterial ink groups at 26 °C. For this, purge protocol described in chapter 4.1 was used. Several replicates were conducted to confirm results. Filament spreading was studied by 3D printing three layers of 30 x 30 mm lattice structures from all biomaterial ink groups and imaging them. The aim was to print as accurate and stable filaments as possible so that the best possible printing accuracy was achieved without filament spreading. From all groups, at least two lattice structures were printed and imaged. The most representative structures are presented in the results. After imaging of each group, the pore areas of the lattice structures were calculated and compared to the theoretical pore area of the 3D design. From each group´s lattice structure, areas of the 36 pores were calculated and their mean value was used for comparison.

Buildability of the biomaterial ink groups was studied by printing higher hollow geometrical structures and imaging them. The chosen 3D designs were a cone and a cylinder as presented in chapter 4.1. From each biomaterial ink group, at least two cone and cylinder structures were printed and imaged. The most representative images of the cylinder and cone structures from each group are presented in the results.

4.5 Biological characterization

Biological characterization of the bioinks included biological optimization of the 3D bioprinting and UV crosslinking, and after that, 0 %, 1 %, and 5 % nHA bioinks were 3D bioprinted. Biological optimization was done by conducting a 3D bioprinting pilot with 1% nHA bioink. In this 3D bioprinting pilot, the effects of different UV exposure times used in crosslinking were examined and the most suitable one was chosen for next 3D bioprinting rounds. The aim of the biological optimization was to ensure cell viability when the photoinitiator IC and UV light were used for crosslinking. After 3D bioprinting, the samples were cultured for 14 days and followed for cell viability, proliferation, morphology, and osteogenic differentiation. Cytotoxicity of the used biomaterial inks and printing process was also evaluated, and printed structures were imaged. The 3D bioprinting pilot with the 1 % nHA bioink was performed once.

After 3D bioprinting pilot, 0 %, 1 %, and 5 % nHA bioink groups were 3D bioprinted by using optimized UV exposure time for crosslinking. In this 3D bioprinting experiment, the aim was to characterize the short- and long-term effect of the different concentrations of nHA and 3D bioprinting process for hBMSCs. After 3D bioprinting the samples were cultured for 21 days and followed as in 3D bioprinting pilot. Additionally, hBMSCs 2D control for immunostainings was prepared and cultured similarly for 21 days. The 3D bioprinting of 0 %, 1 %, and 5 % nHA bioink groups and 2D control were performed once.

The bioinks were handled, and 3D bioprinting was done as described in earlier chapters of the materials and methods. Printing temperature was 26 °C in all 3D bioprinting experiments. The cell density in bioinks was 5 million hBMSCs / ml in all experiments. In each 3D bioprinting experiment, control structures without cells were also 3D printed.

4.5.1 Cell culture for 3D bioprinting

Earlier isolated human bone marrow stem cells (hBMSCs) from an anonymous female donor (referred to as “4/16”) born in 1936, were used in all 3D bioprinting experiments and in the 2D control. At the time of sample collection and isolation of the hBMSCs the donor was 80 years old, was 169 cm tall, and weighed 78 kg. The donor had no signs of osteoporosis or diabetes type I or II. Osteogenic and adipogenic differentiation capability of the cell line was characterized and verified earlier by fluorescence-activated cell sorting, Alizarin Red S staining, and Oil Red O staining.

Frozen hBMSCs were thawed at passage (P) 2, 3, or 4 depending on an experiment in question. Table 10 summarizes the starting passage of the cells in each cell culture round, culturing platform and the experiment where the cells were used. After thawing of the hBMSCs they were plated to either Nunc™ EasYFlask™ Cell Culture T175 cm^2 flasks (T175 flask) (~ 2800 cells/cm^2) (Thermo Fisher Scientific, USA) or directly to 2-chamber CellSTACK® culture chamber (cell stack) (~ 2000 cells/cm^2) (Corning, USA). In case of cells thawed in P 2 the cells were cultured first in T175 flasks until at P 3 they were moved to cell stacks. The cells for 0% nHA bioink 3D bioprinting were cultured only at T175 flasks and cell stacks were not used at all. In all other experiments the last passage culturing was done in cell stacks. In all experiments, the cells were expanded until P 5 and then used for 3D bioprinting or for the 2D control.

Table 10. *Cell culture before 3D bioprinting.*

hBMSCs cell culture starting passage (P)	Cell culture platform	Experiment(s) done
2 and 4	P2 in T175 flasks, in P3 moved to cell stacks.	3D bioprinting pilot with 1 % nHA bioink.
2 and 3	P2 and P3 in T175 flasks, in P4 moved to cell stacks.	3D bioprinting of 1 % and 5 % nHA bioinks.
3	T175 flasks in all passages.	3D bioprinting of 0 % nHA bioink and 2D control.

The cells were cultured in a 5 % CO_2 incubator at 37 °C, and the used culture medium was basic medium (BM), αMEM with sterile filtered 5 % human serum (HS) (Human Serum AB Male, Biowest, France) and 1 % P/S. The medium was changed at least twice a week. For T175 flasks 20 ml and for cell stacks 170 ml of BM was always used. For the duration of cell expansion, human fibroblast growth factor 2 (hFGF-2) 10 µg/ml stock solution (Miltenyi Biotec, Germany) was added directly to the cell culture flask or to the culture chamber with the BM, to achieve hFGF-2 concentration of 5 ng/ml in the cell culture. The cell growth and confluency were followed twice a week.

When the hBMSCs were expanded they were first washed twice with DPBS (10 ml / T175 flask and 30 ml / cell stack) and after that the cells were detached with TrypLE™ Select Enzyme (1X, Gibco^{TM}, Thermo Fisher Scientific, USA) (6 ml / T175 flask and 40 ml / cell stack). The cells with TrypLE™ were kept in the incubator for 5 minutes and the cells were released into suspension by slapping the flask or cells tack on its side. When the cells were detached, BM was added to quench the TrypLE™ (10 ml / T175 flask and 50 ml / cell stack). The cell suspension was moved to Falcon tubes and centrifuged. The supernatant was aspirated away, and the cell pellet was resuspended into an appropriate volume of medium. The cells were counted with TC20 Automated Cell Counter (Biorad, USA) and passaged either to T175 flasks, cell tacks, or used for 3D bioprinting at P 5.

4.5.2 3D bioprinting pilot

3D bioprinting pilot with 1 % nHA bioink was done by using 9.8 mm/s speed and 0.7–0.9 bar pressure. 3D printing with 1 % nHA biomaterial ink, to prepare blank structures, was done by using 9.8 mm/s speed and 1.0–1.2 bar pressure. UV exposure times 45, 60, 75, and 90 seconds per layer were tested for crosslinking of the bioink and biomaterial ink. After printing and crosslinking, the samples were moved from Petri dishes to 12-well plates and moved at 37 °C incubation (5 % CO_2 incubator) in BM (1 ml / well for blanks, 1.5 ml / well for bioprints). Printed structures were cultured for 14 days in BM with additional antimicrobial reagent Normocin^{TM} (1:500, InvivoGen, USA). The medium was changed twice a week. During this time, cell viability and proliferation were evaluated after 1, 3, 7, and 14 days. Cell morphology and osteogenic differentiation of the samples were assessed on day 7, when 3D immunostaining was done. Cytotoxicity of the used bioink and printing process was also evaluated, and printed structures were imaged on each timepoint days to evaluate stability of the structures.

The viability of the hBMSCs was followed by doing live/dead staining. From both blank structures and bioprints and from all UV exposure groups, a half of a printed structure was used. Samples were first washed with DPBS for five minutes and then stained with green-fluorescent having calcein acetoxymethyl (Calcein-AM) and red-fluorescent ethidium homodimer-1 (EthD-1) from the commercial LIVE/DEAD® Viability/Cytotoxicity Kit (Invitrogen, Thermo Fisher Scientific, USA). Calcein-AM and EthD-1 were mixed to DPBS (0.15 µl / ml of DBPS) and applied to samples (2 ml/sample). The samples were protected from light and incubated for 45 minutes at RT. After incubation, the samples were washed with DPBS and imaged with the fluorescence microscope Olympus IX51 (Japan).

The metabolic activity or proliferation of the hBMSCs in samples was studied using commercial Cell Counting Kit-8 (CCK-8) (Dojindo Laboratories, Japan). The dehydrogenase activity in cells generates formazan dye from water-soluble tetrazolium salt of the kit, which is directly proportional to the number of living cells. From both blank structures and bioprints and from all UV exposure groups, four 1/8th samples were collected with a scalpel and moved to 96-well plate. CCK-8 reagent was mixed with the same medium used in culture in ratio 1:10, as stated by the manufacturer. 110 µl of the solution was pipetted to each well with print piece and then the plate was incubated at dark and 37 °C for 2 hours. After incubation, 100 µl of the solution was moved from each well to new 96-well plate. Wallac Victor^2 1420 Multilabel counter was used for absorbance measurement (450 nm) of the reaction plate.

Cytotoxicity of the used bioink and printing process was studied by examining lactate dehydrogenase (LDH) production by cells on days 1, 3, and 7. On each timepoint day, triplicates of culture medium samples from each UV exposure time group were collected. Samples were always collected from three different wells, 1.0 ml from each and they were stored to -80 °C. Commercial colorimetric LDH assay kit (Abcam, United States) was used following the protocol provided by the manufacturer. Before pipetting the samples in 96-well plates, they were thawed on ice, vortexed shortly and then centrifuged at 4 °C 11 000 rpm for 5 minutes, to flush down the released nHA. 10 µl of each sample was used and the volume was then adjusted to 50 µl, by adding 40 µl of the reaction buffer. Standards were prepared in duplicates for each plate and assay buffer was used as a diluent. All samples were analyzed in technical replicates. After reaction mix was added, the output was measured in a kinetic mode at 37 °C protected from light after 5, 15, and 30 minutes from the start of the reaction. Wallac Victor2 1420 Multilabel counter was used for absorbance measurement (490 nm) of the reaction plates. The results from the measurement taken after 15 minutes of starting the reaction is presented in the results.

Cell morphology and osteogenic differentiation of the samples were followed on day 7, by immunostaining. From both blank structures and bioprints and from all UV exposure groups, a half of a printed structure was used and cut with a scalpel. In all stages of 3D immunostaining sufficient volumes to properly cover the samples were used. The samples were washed once with DPBS and fixed with 4 % paraformaldehyde (PFA) (Sigma Aldrich, USA) in DPBS for 1 hour at RT. After fixing the samples were washed twice with DPBS for 10 minutes and then stored at 4 °C until the staining was continued. The samples were permeabilized with 0.3 % Triton-X-100 (Sigma Aldrich, USA) in DPBS for 10 minutes at RT and then blocking was kept overnight on shaker at 4 °C with 10 % normal donkey serum (NDS) (Millipore, USA) 0.1 % Triton-X-100 1 % bovine serum albumin (BSA) (Sigma Aldrich, USA) in DPBS.

Next day the samples were washed with 1 % NDS 0.1 % Triton-X-100 1 % BSA in DPBS on shaker for 3 hours at 4 °C and after that mixture of primary antibody was prepared to the same solution as used in washing and added to the 45 s and 60 s UV exposure samples. Polyclonal rabbit runt-related transcription factor 2 (RUNX2) / CBFA1 antibody (Novusbio, USA) was used as a primary antibody (1:200). For 75 s and 90 s UV exposure samples only 1 % NDS 0.1 % Triton-X-100 1 % BSA in DPBS was used without primary antibody. The samples were kept on shaker for 2 days at 4 °C. After that they were washed with 0.1 % Triton-X-100 1 % BSA in DPBS several times on shaker for 1 day and the last wash was left overnight at 4 °C. Next day the samples were washed once with 1 % BSA in DPBS for 5 minutes and after that mixture of secondary antibody and Phalloidin–Tetramethylrhodamine B isothiocyanate (Phalloidin-TRITC) (1:750, Sigma Aldrich, USA) was prepared to the same solution as used in washing and added to the 45 s and 60 s UV exposure samples. Donkey anti-Rabbit IgG (H+L) Highly Cross-Adsorbed Secondary Antibody, Alexa Fluor 488 (Thermo Fisher Scientific, USA) was used as a secondary antibody (1:400). For 75 s and 90 s UV exposure samples only 1 % NDS 0.1 % Triton-X-100 1 % BSA in DPBS with Phalloidin-TRITC was used without secondary antibody. From secondary antibody addition forward, samples were protected from light. The samples were kept on shaker overnight at 4 °C.

Next day, the samples were washed two times with DPBS for 5 minutes at RT and after that 4′,6-Diamidino-2-phenylindole dihydrochloride (DAPI) (Sigma Aldrich, USA) for nucleic acid staining was added 1:3000 in DPBS for 30 minutes at RT. After DAPI, the samples were washed with DPBS several times for rest of the day on shaker and the last wash was left overnight at 4 °C. Next day the samples were imaged with the fluorescence microscope Olympus IX51.

4.5.3 Final optimized 3D bioprinting

After optimizing material concentrations, IC concentration, and UV exposure time, the final 3D bioprinting with 0 %, 1 %, and 5 % nHA bioinks was done. Printing pressures and speeds are presented in Table 11 separately for the bioinks and biomaterial inks of each group. For UV crosslinking, 45 seconds UV exposure time per layer was used. The 3D printing of blanks and 3D bioprinting were done on consecutive days with each group. After 3D printing or 3D bioprinting and crosslinking, the samples were moved to incubation as in 3D bioprinting pilot.

Table 11. *Printing pressures and speeds of the biomaterial inks and bioinks.*

	0% nHA		**1% nHA**		**5% nHA**	
	No cells	**hBMSCs**	**No cells**	**hBMSCs**	**No cells**	**hBMSCs**
Pressure (bar)	0.8	0.6–0.7	0.6–0.8	0.4–0.6	0.9–1.1	0.6–0.9
Speed (mm/s)	10.0	9.6–10.0	9.8–10.5	9.8	9.8	9.8

Printed structures (with or without cells) were cultured for 21 days and the medium was changed twice a week. On day 1, culturing medium was changed from BM to osteogenic medium (OM). The OM contained αMEM with sterile filtered 5 % HS, 1 % P/S, 250 µM Ascorbic Acid (Sigma Aldrich, USA) and 10 mM β Glycerophosphate disodium salt hydrate (Sigma Aldrich, USA). Additionally, Dexamethasone (Sigma Aldrich, USA) was added directly to the flask, to achieve Dexamethasone concentration of 5 nM in the cell culture, always when OM was changed. As with 3D bioprinting pilot, Normocin^{TM} (1:500) was used in OM and BM.

During culture, cell viability and proliferation were followed on days 1, 3, 7, 14, and 21. The cell viability was followed similarly by doing live/dead staining as in 3D bioprinting pilot (chapter 4.5.2). The metabolic activity or proliferation of the hBMSCs was measured similarly as in 3D bioprinting pilot with CCK-8 (chapter 4.5.2), except this time eight 1/8ths were collected from both blank prints and bioprints of all nHA groups. After day 1, the CCK-8 reagent was mixed with OM instead of BM. LDH production by cells of each nHA bioink group was studied and printed structures were imaged on each timepoint day as in 3D bioprinting pilot (chapter 4.5.2). On day 21 the cell leakage from the bioprints was studied by imaging the well plate bottoms of the bioprints with Zeiss Axio Vert.A1 microscope (Germany).

Cell morphology and osteogenic differentiation of the samples were followed on days 7 and 21 when 3D immunostainings were done. Collecting the samples for staining and 3D immunostainings were done for all nHA groups similarly as in 3D bioprinting pilot (chapter 4.5.2). The same primary antibody and secondary antibody with Phalloidin-TRITC were used for samples collected on day 7. In addition, for day 21 samples mouse monoclonal Anti-Osteocalcin antibody [OCG3] (Abcam, United States) was used (1:400) as a primary antibody. Donkey anti-Mouse IgG (H+L) Highly Cross-Adsorbed Secondary Antibody, Alexa Fluor 488 (Thermo Fisher Scientific, USA) was used (1:400) as a secondary antibody for day 21 samples with Phalloidin-TRITC.

2D control was prepared for functional baseline for staining. It was done by plating the hBMSCs to 12-well plates (10 000 cells / well), which were cultured in the same conditions as 3D bioprinted hBMSCs for 21 days. During this time, the medium changes were done similarly as with bioprints and the growth of the 2D controls was followed by imaging them on days 1, 7, 14, and 21 with Zeiss Axio Vert.A1 microscope. On days 7 and 21, 2D control plates were fixed for staining. The wells were washed three times with DPBS and then fixed with 0.2 % Triton-X-100 4 % PFA in DPBS for 15 minutes at RT. After fixing the wells were washed four times with DPBS and then the plates were stored at 4 °C until the staining was continued. The wells were blocked with 1 % BSA in DPBS for 1 hour at RT. Primary antibodies were diluted in blocking solution and left on shaker overnight at 4 °C. Same primary antibodies and concentrations for days 7 and 21 in 2D controls were used as with bioprints. On next day, the wells were washed three times with DPBS for 3 minutes in every round and after that secondary antibodies diluted in blocking solution were kept on shaker for 45 minutes at 4 °C. From secondary antibody addition forward, samples were protected from light. Same secondary antibodies, Phalloidin-TRITC, and concentrations were used as with bioprints. After secondaries, the wells were washed two times with DPBS for 3 minutes in both rounds and then DAPI was added with third washing solution (1:2000) and incubated 5 minutes at RT. The wells were washed with DPBS and imaged with Olympus IX51.

4.6 Data handle and statistical analysis

All image panels and handling were done by using Fiji ImageJ 2.1.1 software. Data handle and all graphs were done in Microsoft Excel for Microsoft 365 MSO (16.0.13801.20288), except representative graphs from flow sweep and temperature ramp measurements which were obtained from TRIOS software from TA Instruments version v5.1.1.46572. Pore area calculations in printability studies were done using ImageJ.

The statistical significance of data from rheological measurements (extracted data), degradation study, printability study (pore size accuracy), proliferation analysis (CCK-8) and toxicity measurement (LDH assay) were determined with independent-samples t-test, and p-values < 0.01 were considered statistically significant. Statistical analysis was not done for proliferation analysis and toxicity measurement made in the 3D bioprinting pilot. The statistical data analysis was done with IBM SPSS Statistics software V26.0.

5. RESULTS

The effect of different concentrations of nHA in an optimized biomaterial ink composition and the biological responses of hBMSCs embedded in the developed bioinks were evaluated in this thesis. The nHA concentrations were chosen to be 0, 1, 3, and 5 % (w/v). First, the biomaterial inks and printing conditions were optimized, and the biomaterial inks characterized for their material properties. To optimize the cell bioprinting and UV exposure time in crosslinking, bioink of 1 % nHA with hBMSCs was used. After that, the responses of hBMSCs bioprinted in no- (0 %), low- (1 %) and high- (5 %) nHA bioinks were assessed in terms of viability, proliferation, and osteogenic differentiation.

5.1 Optimization of the biomaterial inks and printing conditions

The optimization phase included 4 % GelMA casting pilot with different concentrations of IC and 3D printing pilots with 1 % and 5 % nHA biomaterial inks. Table 12 summarizes all variations in temperatures and exposure times in the IC concentration range test with 4 % GelMA casting, and observations made from the pilot. In first experiment, after first UV exposure on ice, all the samples were liftable from mold. After next UV exposures at RT, the samples were not liftable anymore and it was observed that the earlier stability of the samples was due to gelation on cold temperature, not because of successful crosslinking. To summarize the results from the last three experiments, 4 % GelMA samples with 0.3 % IC concentration were the only samples which showed successful UV crosslinking since they were the only ones which held their structure on a heat plate at 35 °C. In addition to cast samples, droplets of 4 % GelMA with different concentrations of IC were pipetted to a plastic plate which were then exposed to UV light at RT or on ice. After UV exposure, no crosslinking was observed in any sample. Based on literature review (Tables 1 and 2) and experiments made with 4 % GelMA and different concentrations of IC, 0.3 % IC concentration was chosen for future experiments.

Table 12. *Overview of the IC concentration range experiments and its observations.*

Experiment	**IC (w/v %) in sample**	**UV exposure (min)**	**Environment**	**Observations**
1	0.05	1.5	On ice	gelation
	0.10	3.5	RT	no crosslinking
	0.15	4.5		
	0.2 0.3	5.5		
2	0.3	6	On ice	gelation
3	0.3	5	On ice, after UV exposure moved to heat plate at 35 °C	crosslinking
4	0.2 0.3	6	On ice, after UV exposure moved to heat plate at 35 °C	0.3 crosslinking, 0.2 partially crosslinked

3D printing pilots with 1 % and 5 % nHA biomaterial inks and observations from those are summarized in Table 13. UV exposure times from 10 to 30 s were not enough to crosslink the material, when UV distance was 44.5 mm and intensity 40 mW / cm^2, as the structures degraded in 30 minutes incubation. 45 s UV exposure time per layer was enough to crosslink the biomaterial inks with both UV intensities and distances tested. Continuous projection was not enough to crosslink the biomaterial inks, as they dissolved at 37 °C (Figure 18). Successful crosslinking was observed with single projection and UV exposure times from 45 to 105 seconds. In the next 3D printing pilot with 5 % nHA biomaterial ink, UV exposure times for crosslinking with single projection varied from 45 to 90 s per layer, and the exposure times were observed to initiate crosslinking also with this higher nHA concentration having biomaterial ink.

Table 13. *Combinations for single projection UV crosslinking in 3D printing pilots and observations from those.*

Group	**UV distance from last layer (mm)**	**UV beam intensity (mW / cm^2)**	**UV exposure times (s)**	**Observations**
1 % nHA	30.2	64	45, 60, 75, 90, 105	crosslinked
	44.5	40	45, 60	crosslinked
	44.5	40	10, 20, 30	degraded
5 % nHA	30.2	64	45, 60, 75, 90	crosslinked

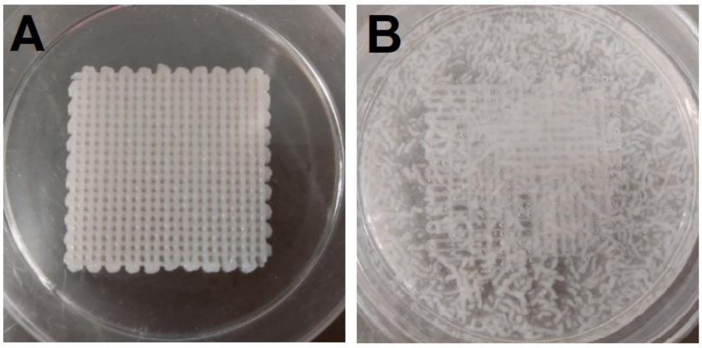

Figure 18. *30 mm x 30 mm structure having 3 layers crosslinked with continuous projection (A). Structure degraded when incubation was started at 37°C in DPBS (B).*

Stability of the 3D printed structures in incubation on day 14 is presented in Figure 19. Based on imaging, stability of both 1 % nHA and 5 % nHA structures was good and they held their structure to the end of the incubation period. On day 14, structures were liftable and it was possible to move and handle them easily.

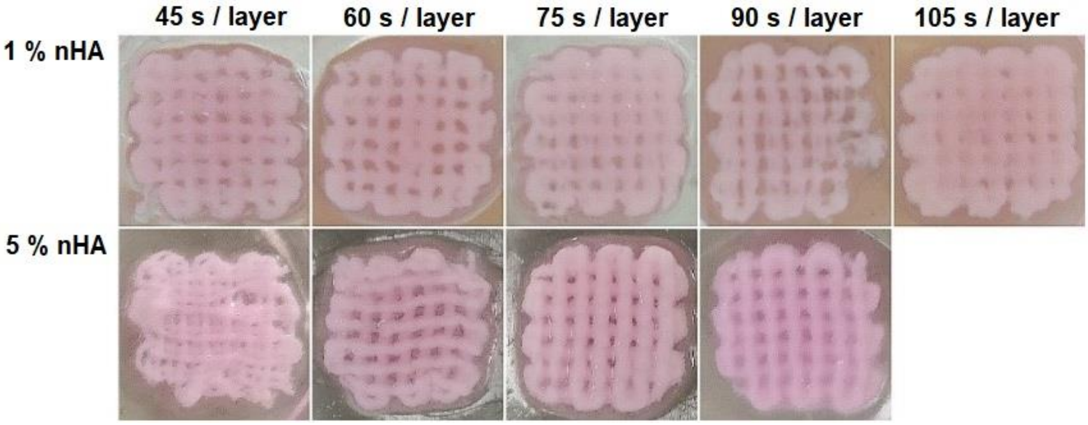

Figure 19. *The stability of the 3D printed structures, crosslinked with different UV exposure times per layer, in incubation on day 14.*

During incubation, it was observed that, in addition to UV crosslinking parameters, the thickness of the printed filament also had an effect on the stability of the structures. For instance, the structures crosslinked with 90 s (1 % nHA) and 45 s (5 % nHA) exposure times (Figure 19), are degraded more than others as too thin filament was 3D printed. With 5 % nHA sample, crosslinked with 45 s exposure time (Figure 19), a small displacement of the filaments also occurred during 3D printing, probably because of small movement of the petri dish.

5.2 Preparation of the biomaterial inks and bioinks

At the same time with 3D printing pilots with 1 % and 5 % nHA biomaterial ink groups, biomaterial ink mixing protocol was optimized. In first hydrogel mixing with 1 % nHA biomaterial ink, visible nHA clumps, not dissolved while mixing, were observed. Based on this observation, different protocol and mixing order of the components was tested with 5% nHA biomaterial ink. New mixing order of 5 % nHA biomaterial ink was better than previous one, since the biomaterial ink was smoother and did not contain nHA clumps after mixing.

After 3D printing pilots, final concentrations of the developed biomaterial ink components were decided, and final mixing protocol of the biomaterial inks was specified. Despite optimized mixing protocol, biomaterial inks mixed were having couple of transparent small clumps in some mixing times being not totally smooth. This time clumps were not unmixed nHA, but rather small amounts of unmixed nanocellulose or GelMA. This caused occasional needle clogging in 3D printing. However, clumps in the biomaterial inks were not observed in all mixings.

5.3 Rheological characterization of the biomaterial inks

Results from rheological characterization are illustrated in Figures 20 and 21. In “temperature sweep” from 37 to 20 °C with shear rate 1.0 1/s, viscosity of all biomaterial ink groups increased when temperature was decreased (Figure 20 (A)). Biomaterial inks with higher nHA concentration had also higher viscosity over the whole temperature range. In lower temperatures (<25 °C) viscosity of the 0 % and 1 % nHA groups was similar.

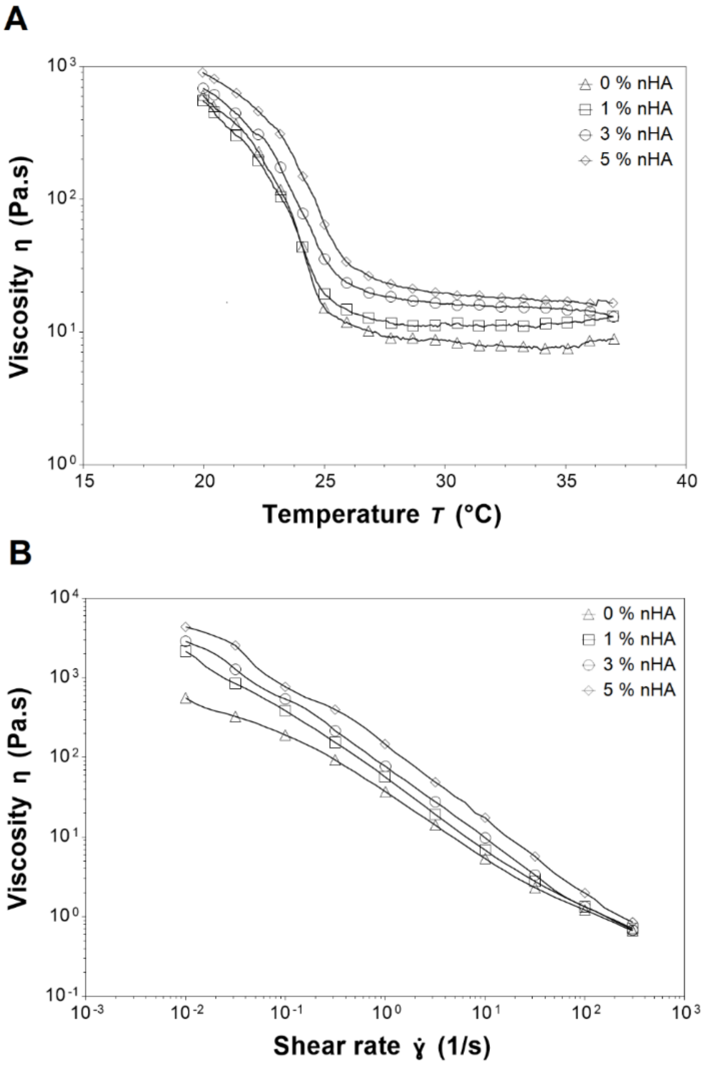

Figure 20. *Temperature sweep from 37 to 20 °C (A) and flow sweep at 26 °C (B) for biomaterial inks with different concentrations of nHA.*

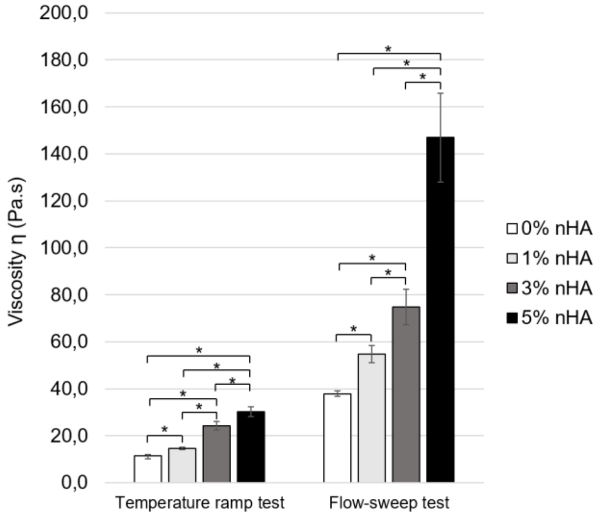

Figure 21. *Extracted data from rheological experiments of each biomaterial ink group, when shear rate is 1.0 ± 0.00007 1/s and temperature 26.0 ± 0.03 °C. n=4, * indicates p < 0.01.*

In “flow sweep” the viscosity of the biomaterial inks as a function of shear rates was measured at 26 °C (Figure 20 (B)). In these measurements, viscosity decreased in all groups when shear rate increased, indicating shear thinning behaviour of the biomaterial inks. Viscosity data from “temperature sweep” and “flow sweep” measurements were also extracted to their own graph when shear rate was 1.0 ± 0.00007 1/s and T = 26.0 ± 0.03 °C (Figure 21). At 26 °C, which was the printing temperature used, the viscosity of the 5 % nHA biomaterial ink was the highest and the viscosity was lowest with the 0 % nHA biomaterial ink both in “temperature sweep” and “flow sweep”. In both measurements viscosities of the biomaterial ink groups, were also significantly different. In “flow sweep” biomaterial inks had higher viscosities than in “temperature sweep” at 26 °C.

5.4 Stability of the biomaterial inks

Figure 22 presents 3D printed structures with different nHA concentrations right after 3D printing and on each timepoint day. In Figure 23, the release of gelatin from the structures based on BCA assay is illustrated. Absorbance units in the figure correlate to the amount of released gelatin.

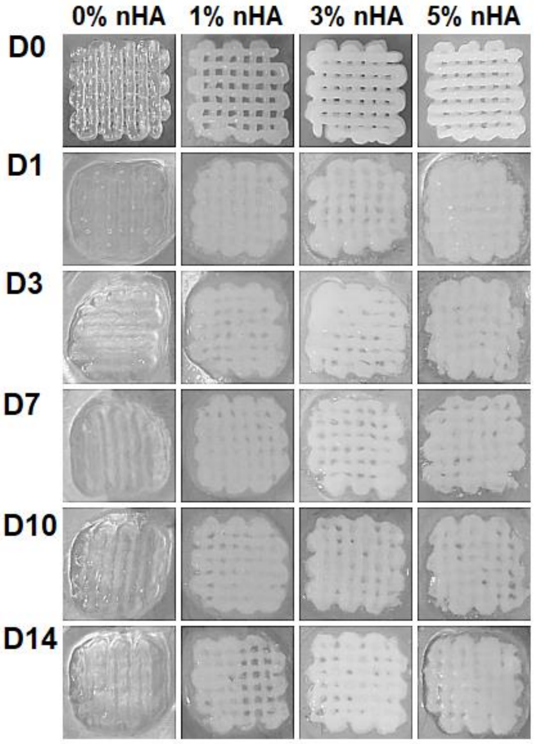

Figure 22. *3D printed structures with different nHA concentrations on days 0, 1, 3, 7, 10, and 14 (D 0-14). Day 0 prints are imaged right after 3D printing and crosslinking.*

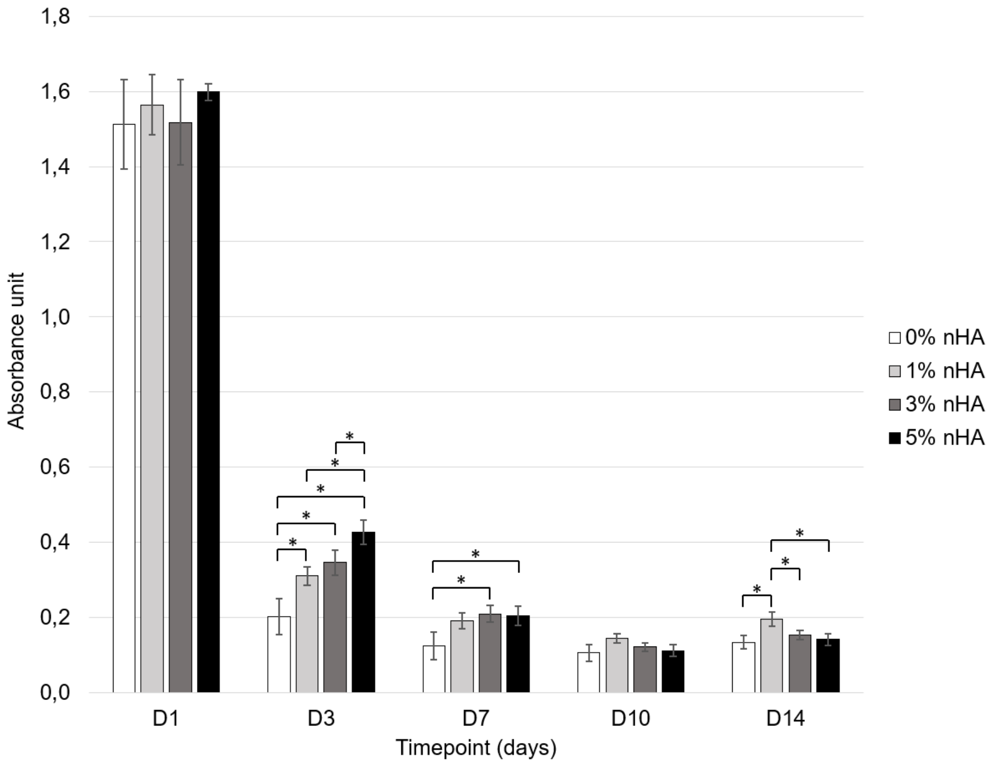

Figure 23. *The release of gelatin from the printed structures with different nHA concentrations. n=5, * indicates p < 0.01.*

Based on imaging (Figure 22), stability of all crosslinked biomaterial inks was good and they held their structure to the end of the incubation period, as in earlier 3D printing of 1 % and 5 % nHA groups (Figure 19). From the results of BCA assay (Figure 23), it was observed that most of the gelatin release happened on day 1. After day 1, the release of gelatin from the structures decreased. The release of gelatin on days 1 and 10 was similar between groups. On day 3, 0 % nHA group had significantly lower and 5 % nHA group had significantly higher release than other groups.

5.5 Printability of the biomaterial inks

The printability studies of the biomaterial inks included imaging of the structures and evaluation in a filament formation test, filament spreading, and buildability. The filament formation test was studied by extruding smooth filaments with all biomaterial ink groups at 26 °C (Figure 24). With all groups, filaments were successfully printed. With the 5 % nHA biomaterial ink, the filament had slightly less smooth filament with irregularities.

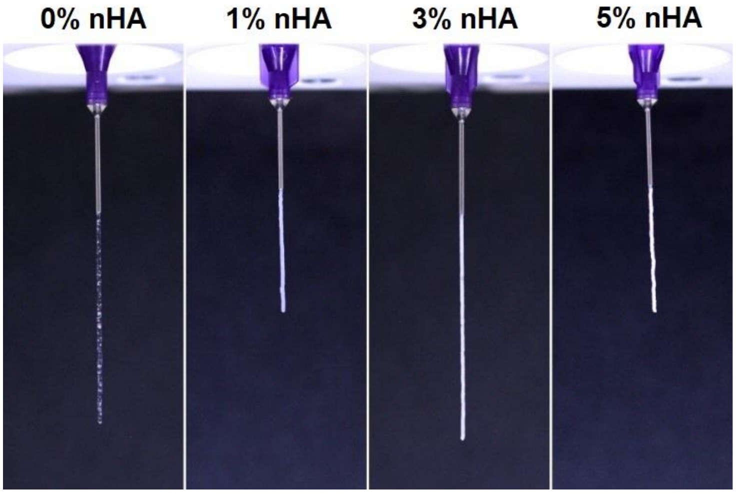

Figure 24. *Filament formation test. Filaments of all biomaterial ink groups were extruded.*

Filament spreading and pore geometry were studied by 3D printing three layers of 30 x 30 mm lattice structures from all biomaterial ink groups and imaging them. The most representative structures are presented in Figure 25 (A), together with threshold images from ImageJ, which illustrate the shape of the pores in each group. Based on Figure 25 (A), the sharpest filament and most square-like pores, resembling 3D design, were observed in 0 % and 5 % nHA groups. Filament breaks, occurred during 3D printing, were observed in 3 % and 5 % nHA structures. Pore size area accuracy relative to design of each biomaterial ink group is also presented in Figure 25 (B). Shortly, pore size area of the 0 % and 5 % nHA biomaterial ink groups were closest to the theoretical pore area of the design.

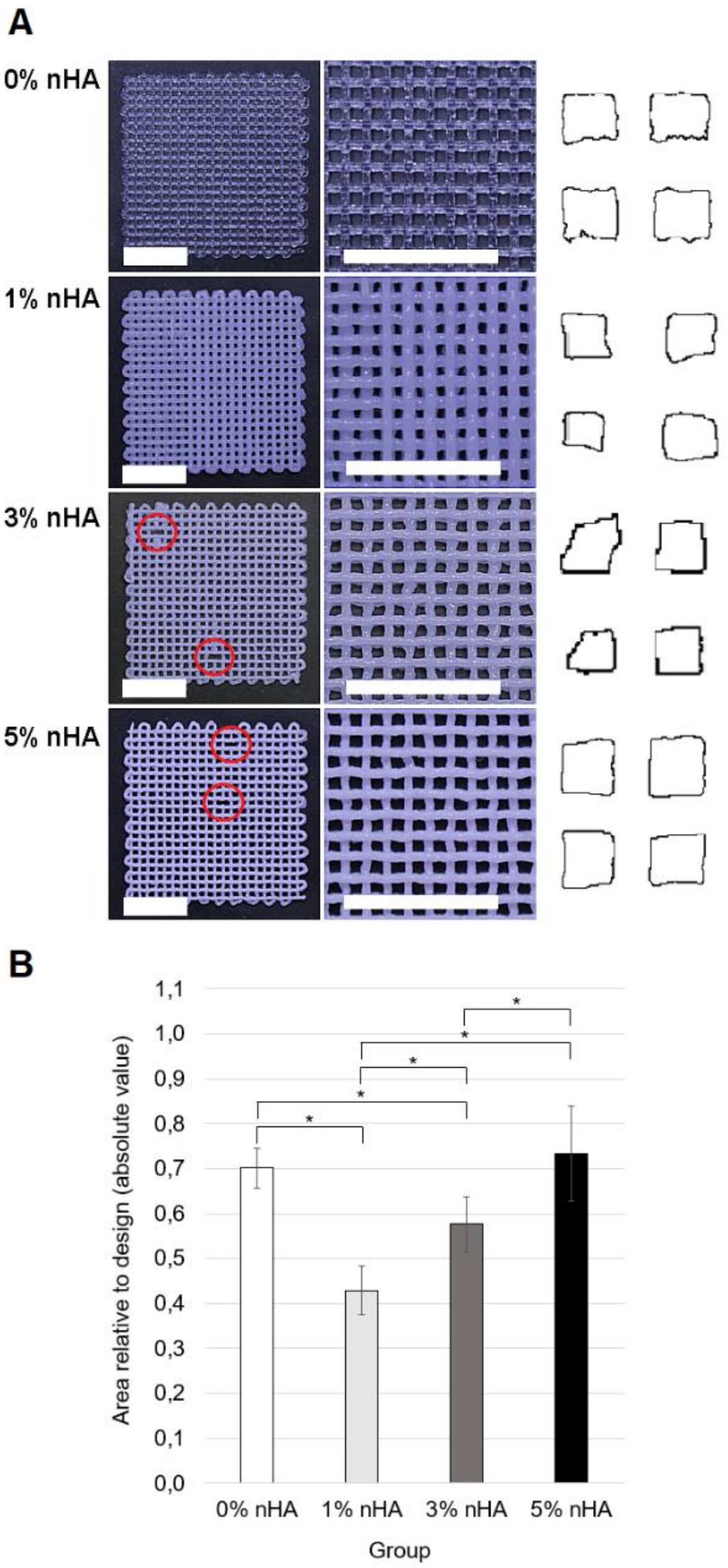

Figure 25. *Filament spreading. (A) From left to right: 3D printed lattice structures of all groups, magnified images from the same structures, threshold images from ImageJ which describe the shape of the pores (taken from the centre of the images). Red circles indicate filament breaks occurred during 3D printing. Scale bar 10 mm. (B) Pore size area accuracy relative to design. n=36, * indicates $p < 0.01$.*

Buildability of the biomaterial ink groups was studied by 3D printing higher hollow geometrical structures and imaging them. The most representative images of the cylinder and cone structures from each group are presented in the Figure 26.

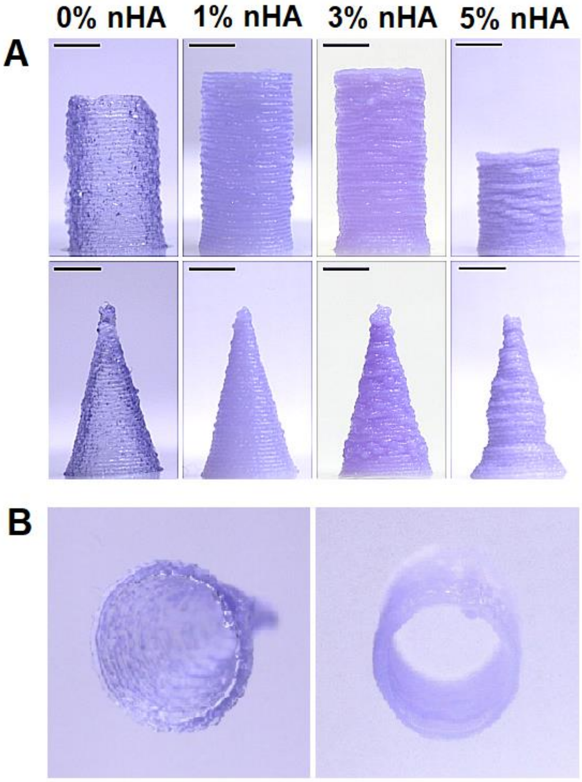

Figure 26. *Buildability of the biomaterial inks. Hollow cylinders and cones from all groups (A). Scale bar 5 mm. 0 % nHA cone (left) and 1 % nHA cylinder (right) from the side (B).*

Buildability of the biomaterial inks was good with 0 %, 1 %, and 3 % nHA biomaterial inks. The highest 3D printed cylinders were 2 cm high, and they were achieved with the 1 % and 3 % nHA biomaterial inks. With the 5 % nHA biomaterial ink, it was not possible to print a cone or a cylinder of 2 cm, as the structure collapsed when filament breaks occurred. Structures made, were also elastic and self-standing. All printed cones and cylinders in the printability studies were possible to lift and turn upside down.

5.6 3D bioprinting pilot

Biological optimization was done by conducting a 3D bioprinting pilot with 1 % nHA bioink. Stability of the 3D bioprinted structures and blanks, crosslinked with different UV times, is presented in Figure 27. Stability of all UV exposure time groups was good in incubation and, as in earlier 3D printing studies (Figures 19 and 22), the structures with or without cells held their structure to the end of the incubation period. Still, some difference in filament thicknesses between blanks and bioprints with hBMSCs was observed. Bioprints with hBMSCs looked more degraded or grainy and had thinner filaments. The difference observed was likely caused by cells, not printing process.

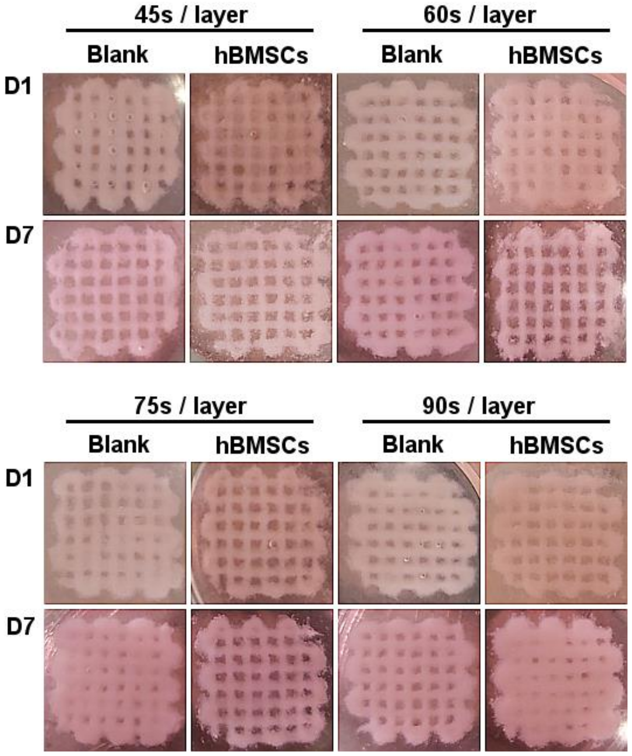

Figure 27. *The stability of the printed structures (with or without cells) crosslinked with different UV times in incubation on days 1 and 7 (D 1 and 7).*

Figures 28 and 29 present cell viability of hBMSCs in 3D bioprinting pilot. In Figure 28, the hBMSCs viability on days 1, 7, and 14 in bioprints is presented. Results from live/dead staining were observed and estimated visually. Based on the live/dead staining, after 1 day, several dead cells (red) were observed in all groups. In general, viability of the cells decreased with increasing the UV exposure time. Cells in the structures that had the longest UV exposure times (75 and 90 s/layer) failed to recover from the printing shock after 14 days in culture. Cells that were subjected to shorter UV exposure times (45 and 60 s/layer) maintained high viability from day 7 to day 14. In general, less dead cells were observed in the samples at 14 days in culture, as they were probably flushed away during medium changes. In Figure 29, the first and last printed layers in the same bioprint are compared from day 7 samples of all UV exposure groups. In all UV exposure groups, the cell viability of hBMSCs was observed to be lower in the 1st printed layer of the bioprints when compared to 4th or upper layers.

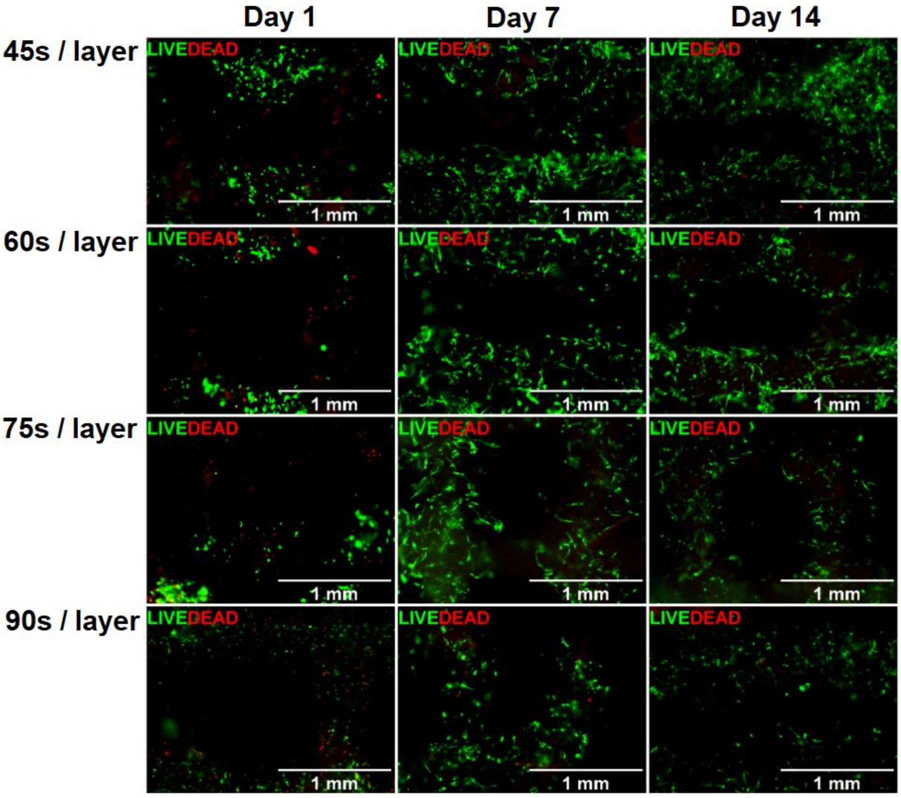

Figure 28. *Cell viability in 3D bioprinting pilot on days 1, 7, and 14. UV exposure times 45 s, 60 s, 75 s, and 90 s per layer.*

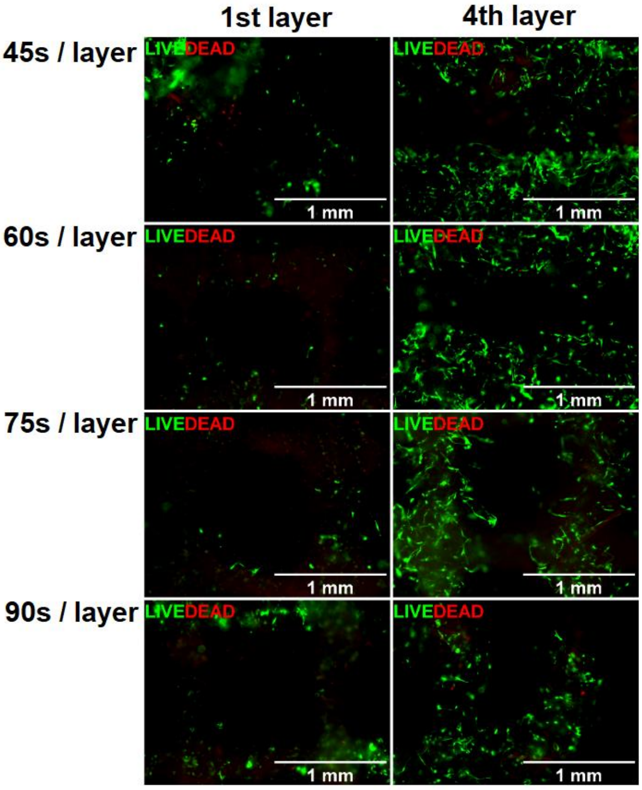

Figure 29. *Cell viability in 3D bioprinting pilot on day 7. Comparison of the first and last printed layer in the same print. UV exposure times 45 s, 60 s, 75 s, and 90 s per layer.*

Proliferation or viability of the hBMSCs in 3D bioprinting pilot, based on CCK-8, is presented in Figure 30. On days 1 and 3, the metabolic activity was observed to be higher in 75 and 90 second UV exposure groups, when compared to other groups. However, decreasing mitochondrial activity was observed in these groups from day 1 to day 7. 45 second UV exposure group showed the highest increase in metabolic activity from day 3 to day 7 and maintained that until 14 days. 60 second UV exposure group showed decreased mitochondrial activity from day 7 to day 14. At 14 days, 45 second UV exposure group had highest metabolic activity of the hBMSCs. However, statistical analysis of the results was not done.

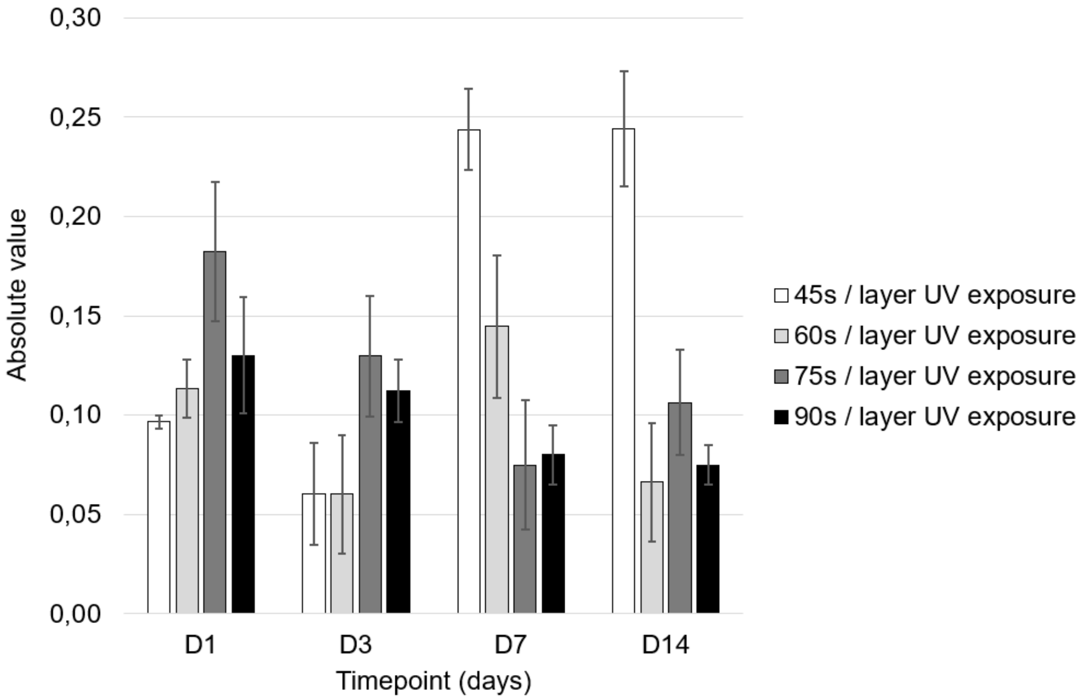

Figure 30. *Proliferation of the hBMSCs in 3D bioprinting pilot. CCK-8 results from 1 % nHA bioprinting with hBMSCs and by using different UV exposure times for crosslinking. n=4.*

Figure 31 presents normalized LDH production by cells in 3D bioprinting pilot. Normalized LDH production by cells decreased in all groups from day 1 to day 7. On days 1 and 3, higher LDH production by cells was observed with 45- and 60-seconds exposure time groups. On day 7, 45 seconds UV exposure time group demonstrated the lowest LDH production. Statistical analysis of the results was not done.

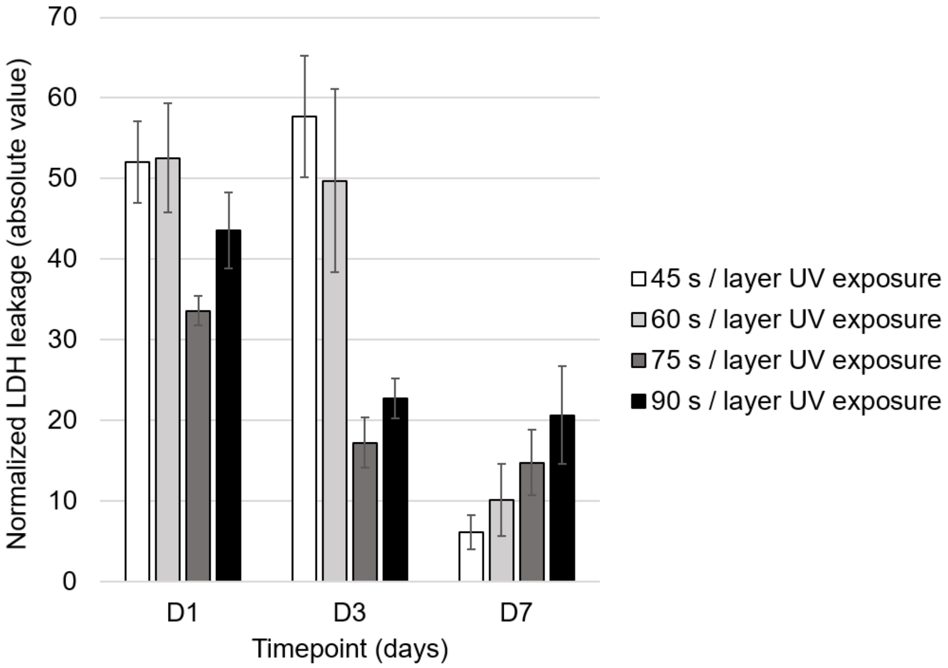

Figure 31. *Cytotoxicity of the bioinks or 3D bioprinting process for hBMSCs. LDH production by cells on days 1, 3 and 7 in 3D bioprinting pilot. Measurement point = 15 min, n=3.*

Cell morphology of the 3D bioprinted hBMSCs from all UV exposure groups was studied on day 7. This was done with Phalloidin-TRITC and DAPI staining for visualization of actin filaments and nuclei of the cells (Figure 32). In addition, osteogenic differentiation of the 3D bioprinted hBMSCs from 45 and 60 second UV exposure time groups was also studied on day 7. Immunostainings were made to detect the early phase osteogenic marker RUNX2 together with the actin filaments and nuclei of cells (Figure 33).

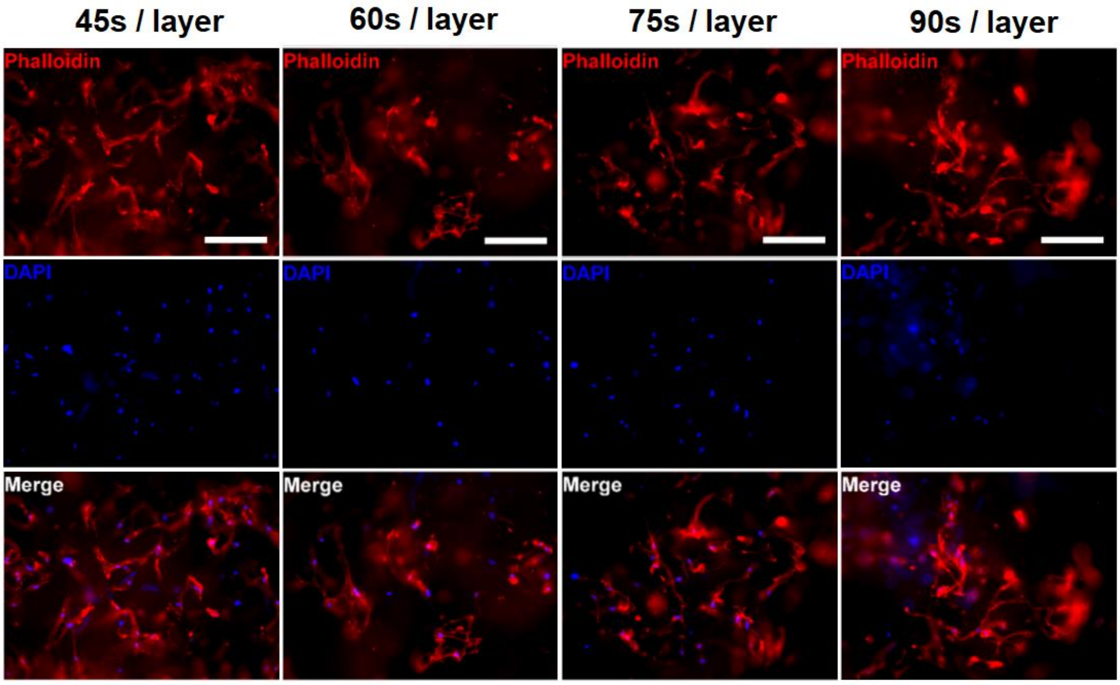

Figure 32. *Cell morphology of hBMSCs in bioprints on day 7. UV exposure times 45 s, 60 s, 75 s, and 90 s per layer. Scale bar 200 µm.*

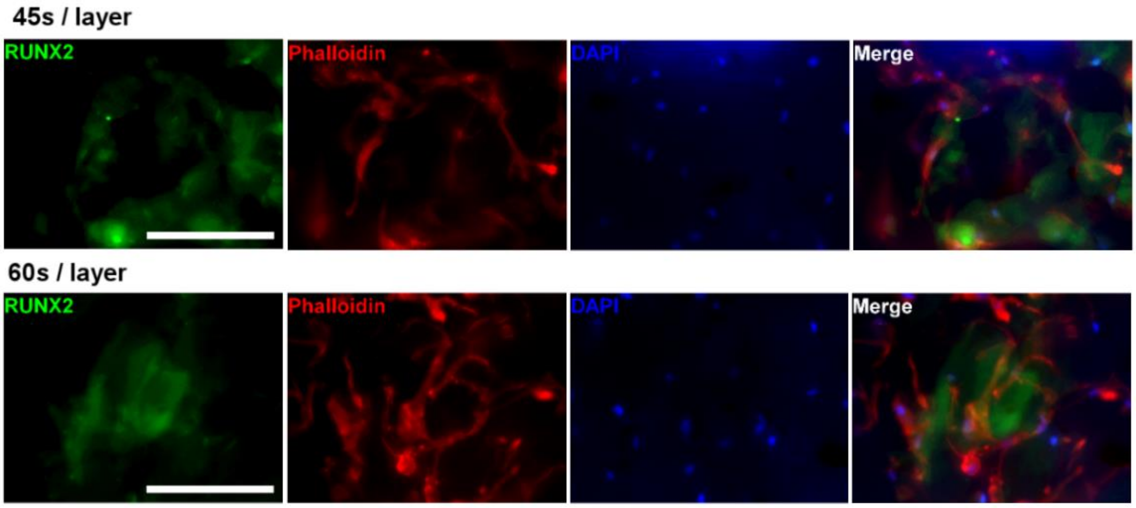

Figure 33. *Osteogenic differentiation of hBMSCs in bioprints on day 7. Expression of RUNX2. UV exposure times 45 s and 60 s per layer. Scale bar 200 µm.*

No obvious differences, in cell morphology between groups (Figure 32), were observed. The cells were elongated and spread into the 3D space of the bioink. Osteogenic differentiation (Figure 33) was not possible to verify based on the expression of the osteogenic marker RUNX2 in the samples, as the used antibody had strong background staining in the biomaterials used.

5.7 Final optimized 3D bioprinting

3D bioprinting with hBMSCs was done for 0 %, 1 %, and 5 % nHA bioink groups. Stability of nHA groups in incubation on each timepoint day is presented in Figure 34 (A). Stability of all nHA groups was good in incubation and the structures with or without cells held their structure to the end of the incubation period, up to three weeks. Still, some difference in filament thicknesses between blanks and bioprints with hBMSCs was observed as in 3D bioprinting pilot. In the 0 % nHA group, the pores of the structures were not so clear or visible as with other groups. During incubation nHA leakage from the structures was especially observed from the 5 % nHA group since the culturing medium contained a clear nHA sediment. From all groups, cell leakage from the structures was observed on day 21, by imaging the well plate bottoms of the bioprints with a light microscope (Figure 34 (B)).

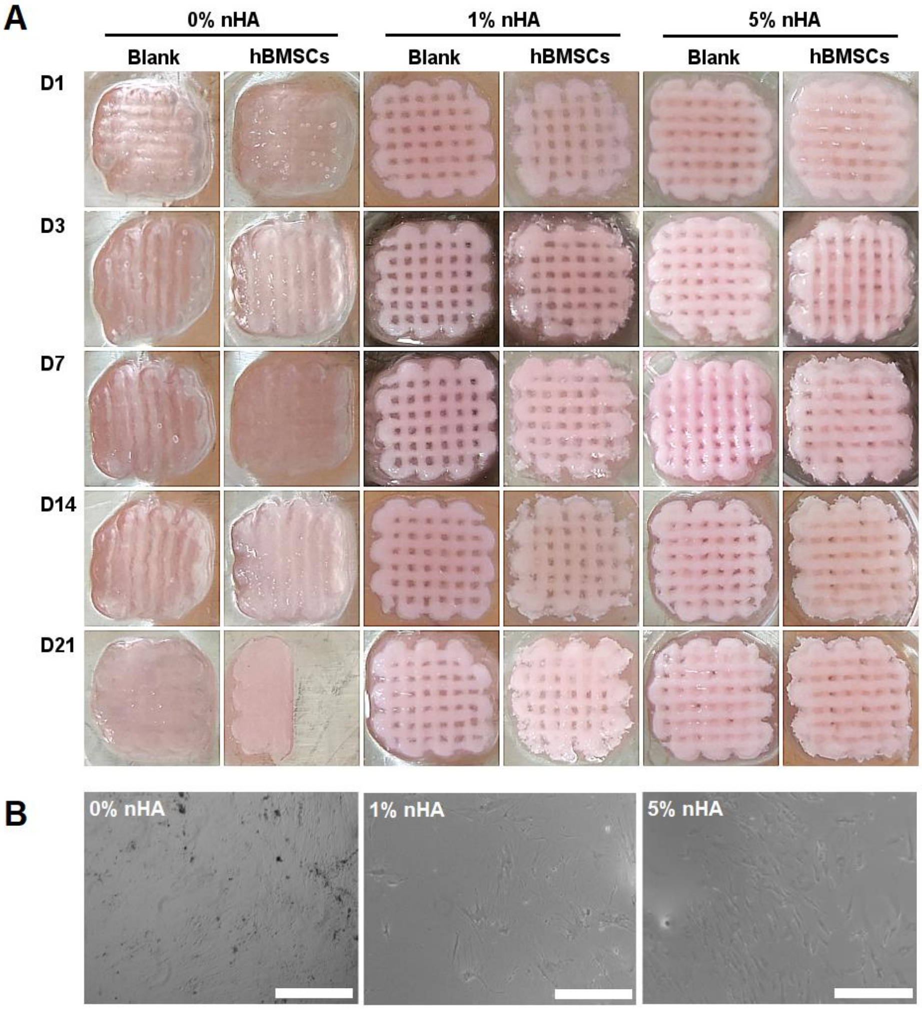

Figure 34. *The stability of the printed structures in incubation for three weeks (A). On day 21 (D21), only half a print for 0 % nHA with cells was imaged. Cell leakage from 3D bioprinted structures (B). Well bottoms of the 12-well plates on day 21, where structures with hBMSCs were incubated. Scale bar 500 µm.*

Figures 35 and 36 present cell viability of hBMSCs in nHA groups. In Figure 35, the hBMSCs viability on days 1, 3, 7, 14, and 21 in bioprints is presented. As in 3D bioprinting pilot, results were observed and estimated visually. Based on the live/dead staining after 1 and 3 days, several dead cells (red) were observed in all groups. Cells in the structure that had the highest nHA concentration (5 %) presented decreased viability at 21 days of culture. Cells in the structures that had 0 % or 1 % nHA concentration maintained high viability throughout the culture period. In Figure 36, the first and last bioprinted layers in the same structure are compared on day 7 samples of all nHA groups. As in 3D bioprinting pilot, the cell viability of hBMSCs was observed to be lower in the 1st bioprinted layer of the structure when compared to upper layers of the bioprints. Based on visual observation, decreased cell viability or growth was not observed in 2D control (Figure 37).

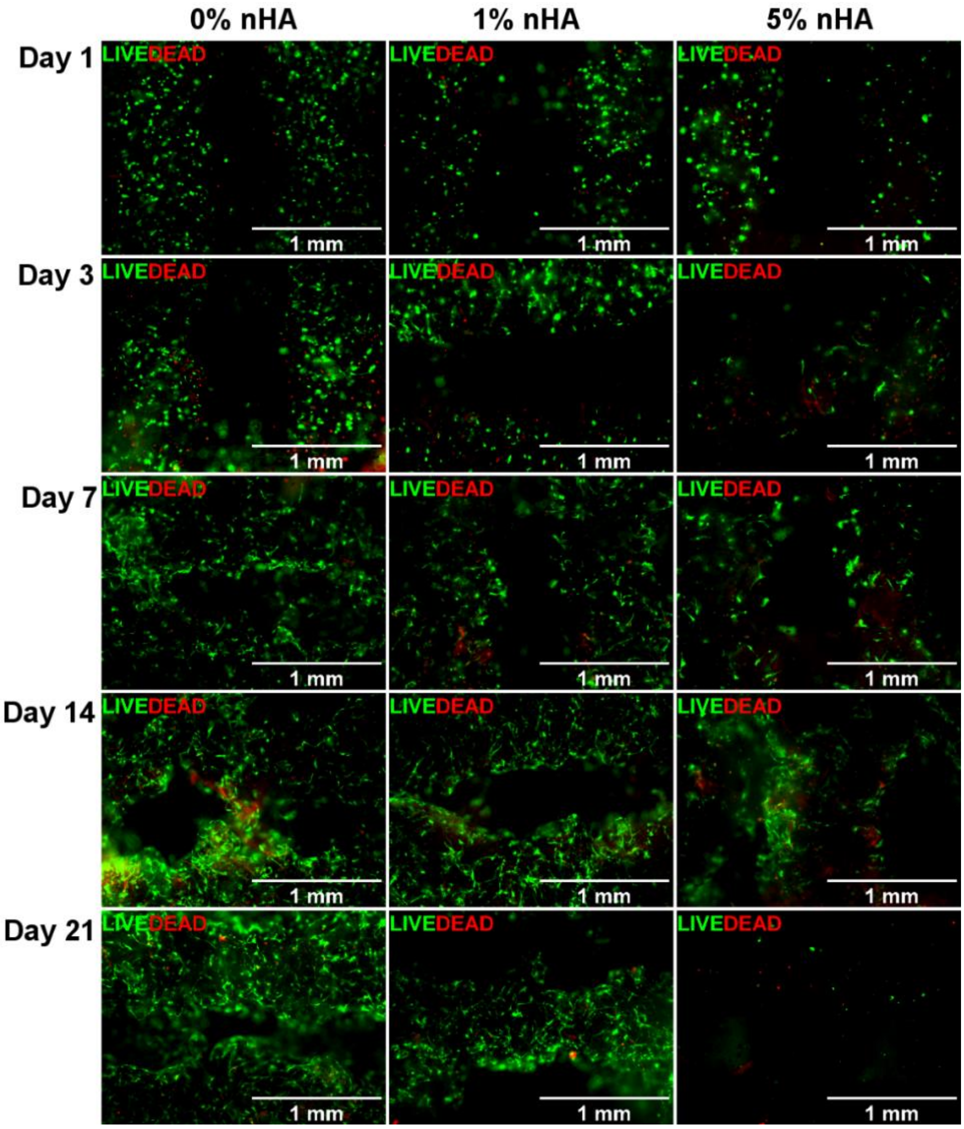

Figure 35. *The hBMSC viability of the bioprints with different nHA concentrations on days 1, 3, 7, 14, and 21.*

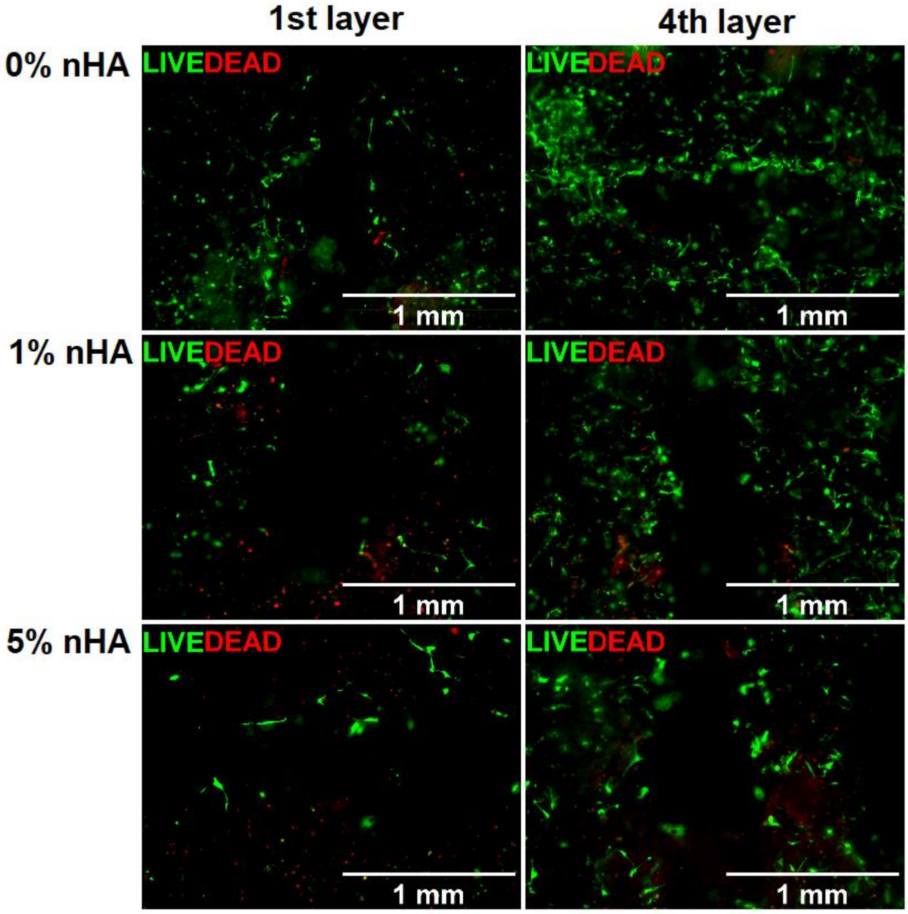

Figure 36. *The hBMSC viability of the bioprints with different nHA concentrations on day 7. Comparison of the first and last printed layer in the same print.*

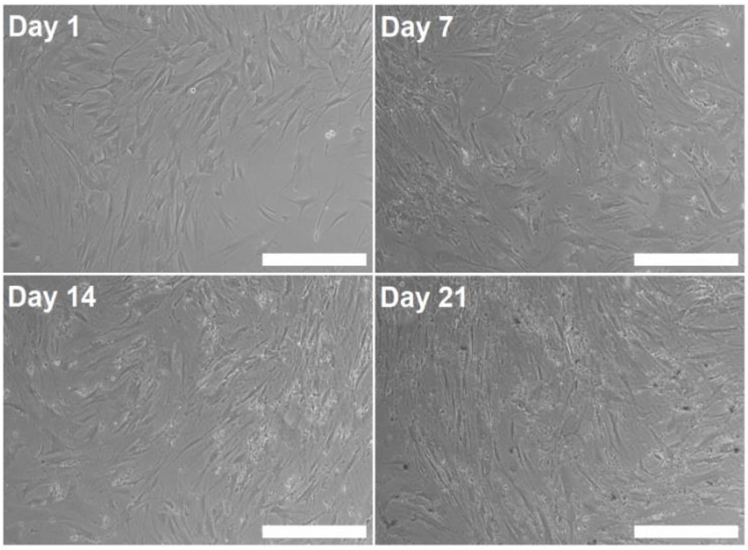

Figure 37. *Cell growth and proliferation of hBMSCs in 2D control. Scale bar 500 µm.*

Relative proliferation of the hBMSCs in bioprints with different concentrations of nHA, based on CCK-8, is presented in Figure 38. On days 1, 3, 7, and 21, proliferation was significantly higher both in 0 % and 1 % nHA group than in 5 % nHA group. On day 21, proliferation of hBMSCs in the 1 % nHA group was significantly higher than in the 0 % and 5 % nHA group. In the 1 % nHA group, the metabolic activity remained quite stable, whereas the 0 % and 5 % nHA groups showed decreased mitochondrial activity from day 7 to day 21.

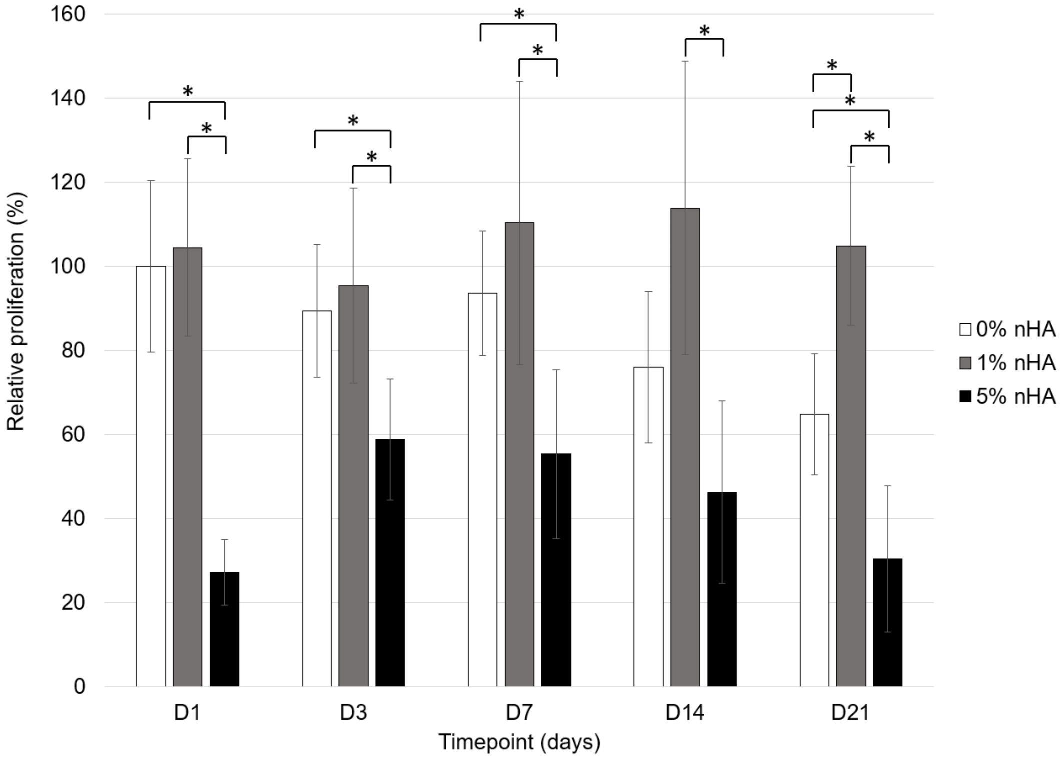

Figure 38. *Relative proliferation of hBMSCs in bioprints with different nHA concentrations. n=8, * indicates p < 0.01.*

Figure 39 presents normalized LDH production by cells 3D bioprinted with different nHA concentrations on days 1, 3 and 7. Normalized LDH production by cells decreased in all groups from day 1 to day 7. On day 1, 5 % nHA group had significantly higher LDH production by cells than 0 % and 1 % groups had.

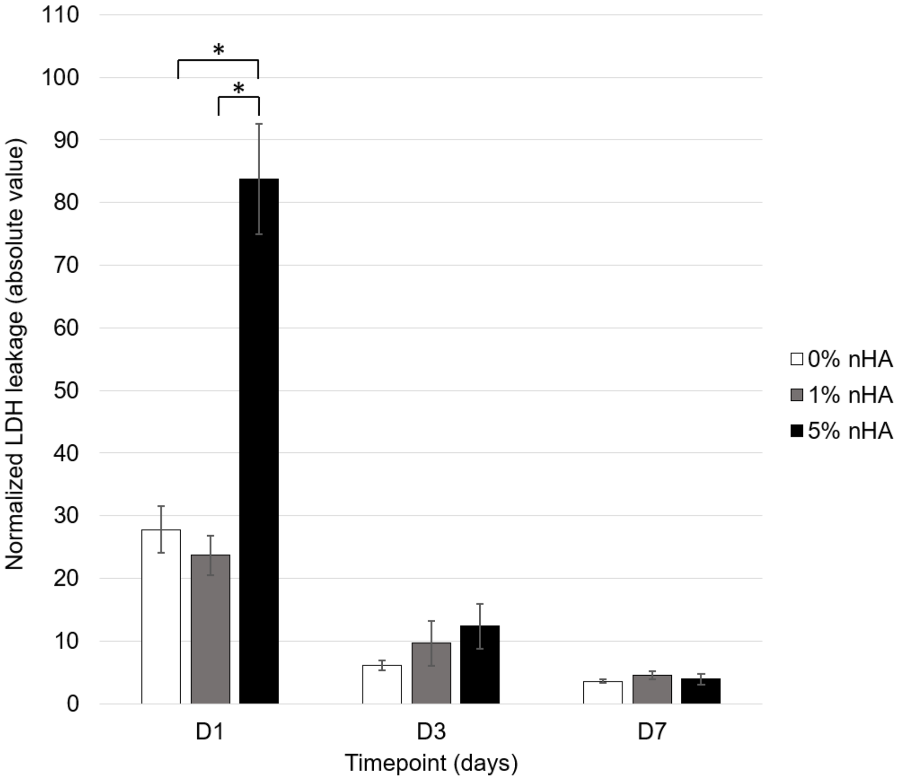

Figure 39. *Cytotoxicity of the bioinks or 3D bioprinting process for hBMSCs. Normalized LDH production by cells 3D bioprinted with different nHA concentrations on days 1, 3, and 7. Measurement point =15 min, n=3. * indicates $p < 0.01$.*

Cell morphology of the 3D bioprinted hBMSCs from all nHA groups and 2D control was studied on day 7 (Figure 40) and day 21 (Figure 41) as in 3D bioprinting pilot. No obvious differences in cell morphology between groups were observed. The cells were elongated and had a fibroblastic cell morphology typical for hBMSCs. On day 21, especially fine morphology of cells was observed in 1 % nHA group. Cell spreading into the 3D space of bioinks was better, when compared to hBMSCs in 3D bioprinting pilot (Figure 32).

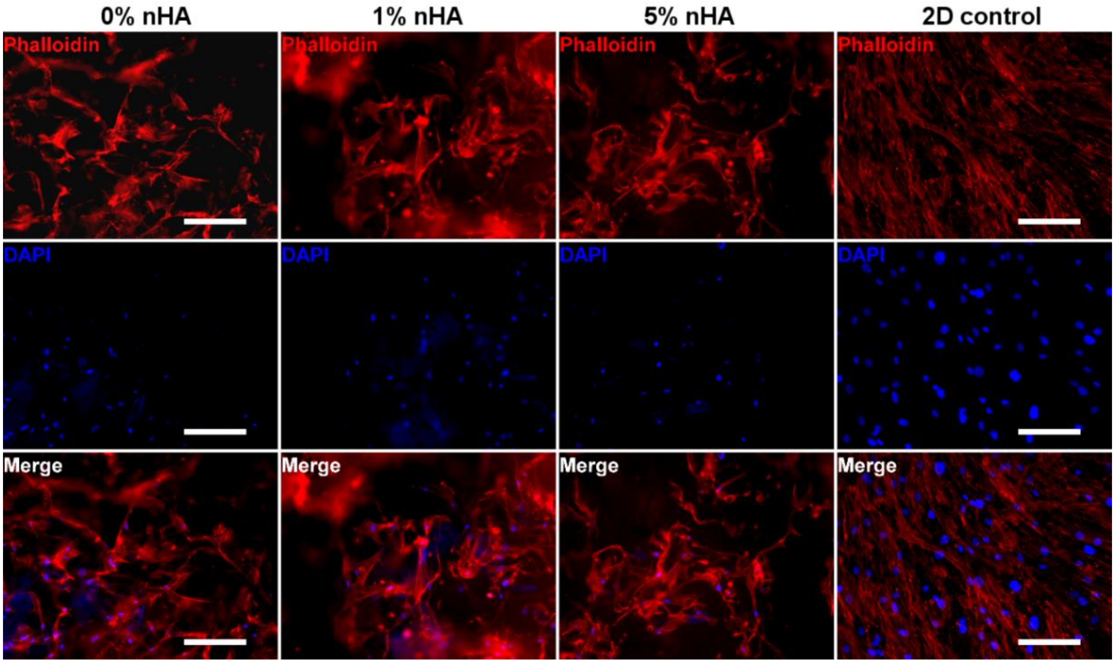

Figure 40. *Cell morphology of hBMSCs in bioprints and in 2D control on day 7. Scale bar 200 µm.*

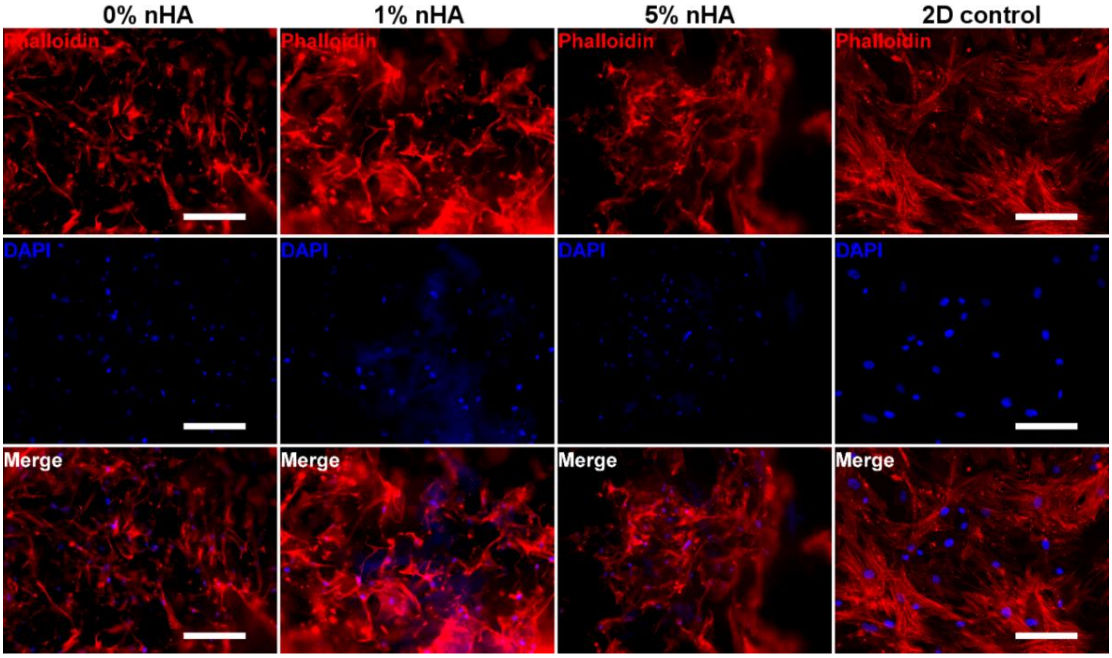

Figure 41. *Cell morphology of hBMSCs in bioprints and in 2D control on day 21. Scale bar 200 µm.*

Osteogenic differentiation of the 3D bioprinted hBMSCs of all nHA groups was studied on days 7 and 21. Immunostainings were done for visualization of early phase osteogenic marker RUNX2 (day 7 samples) (Figure 42) and late phase osteogenic marker osteocalcin (day 21 samples) (Figure 43), together with actin filaments and nuclei of cells. In Figure 44, expression of RUNX2 and osteocalcin in 0 % nHA blank structure and structure with cells are compared by presenting green channels also for blanks. Both used antibodies had strong background staining for the biomaterials. With RUNX2, despite strong background staining, some expression possibly located to nuclei was observed in all groups (Figure 42). It was not possible to verify expression of osteocalcin in the samples from day 21 (Figure 43). Some areas with staining were detected but it was difficult to determine whether this was correct osteocalcin staining or just a background from the material. Day 21 osteocalcin expression in 2D control hBMSCs was also weak.

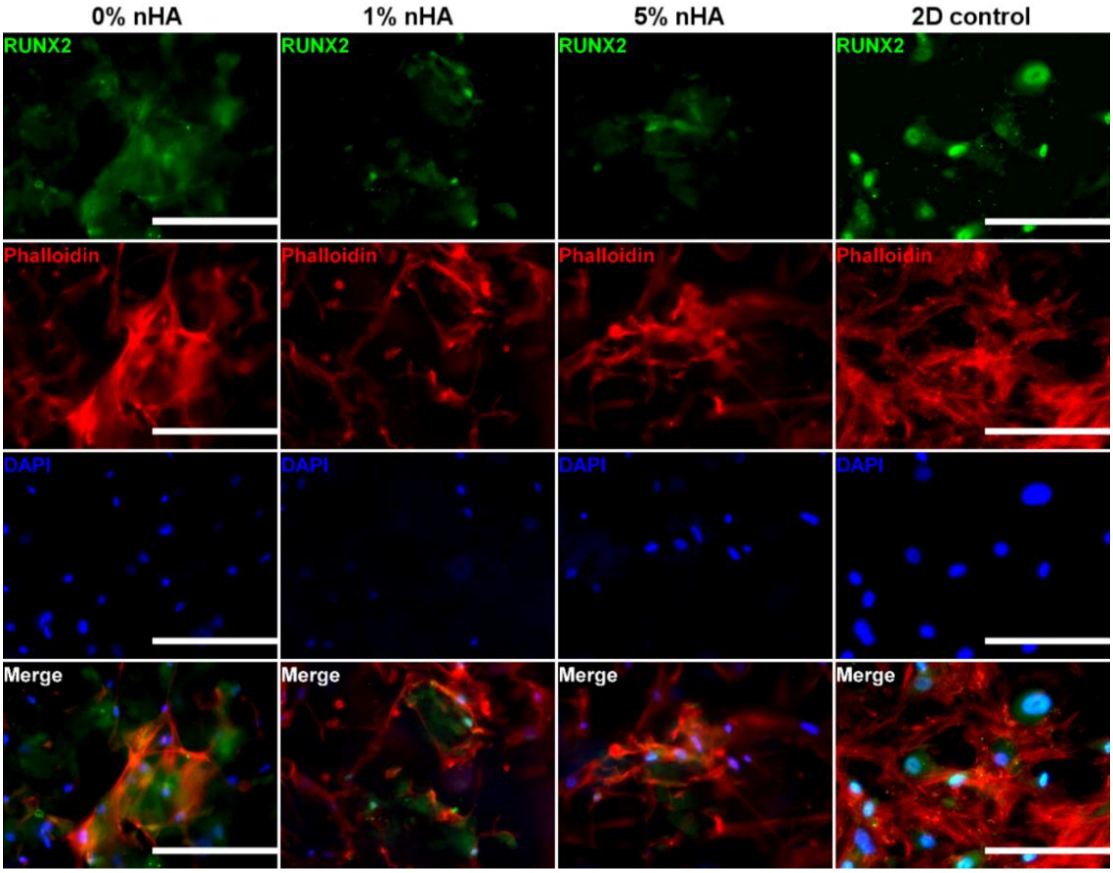

Figure 42. *Osteogenic differentiation of hBMSCs in bioprints and 2D control on day 7. Expression of RUNX2. Scale bar 200 µm.*

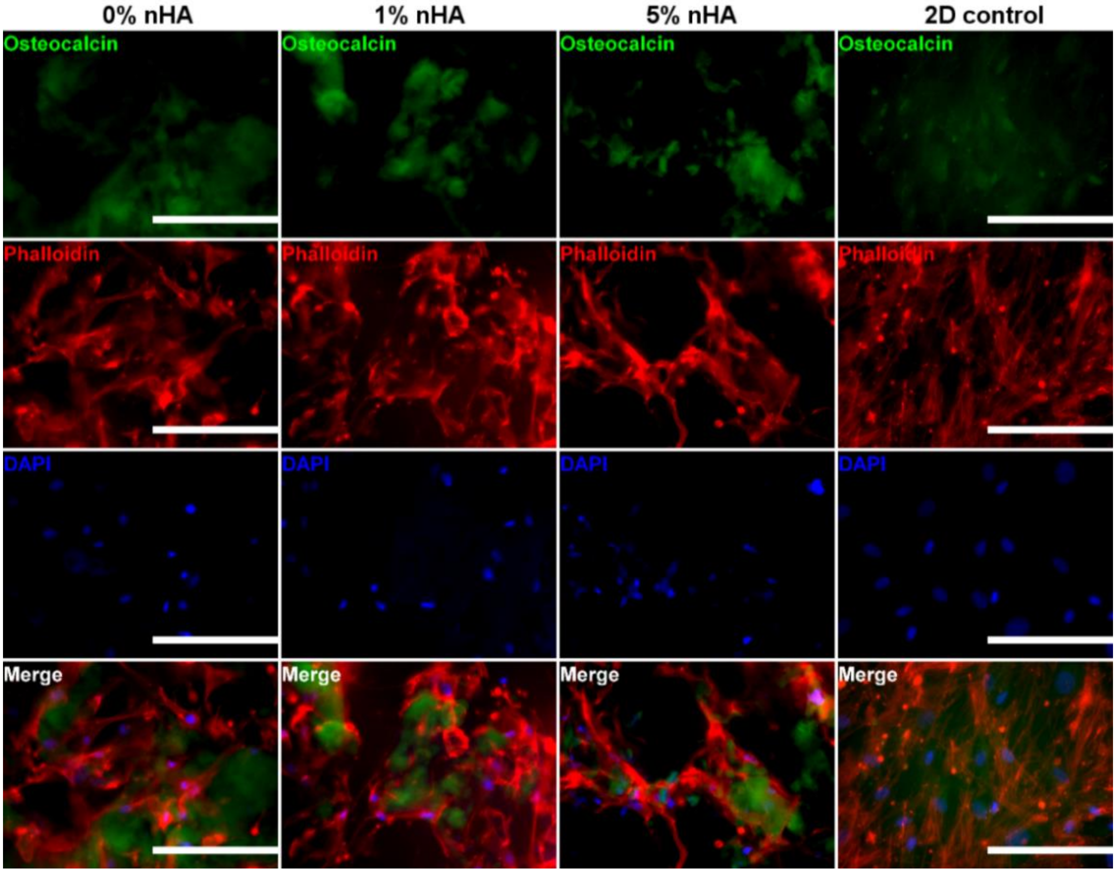

Figure 43. *Osteogenic differentiation of hBMSCs in bioprints and 2D control on day 21. Expression of osteocalcin. Scale bar 200 µm.*

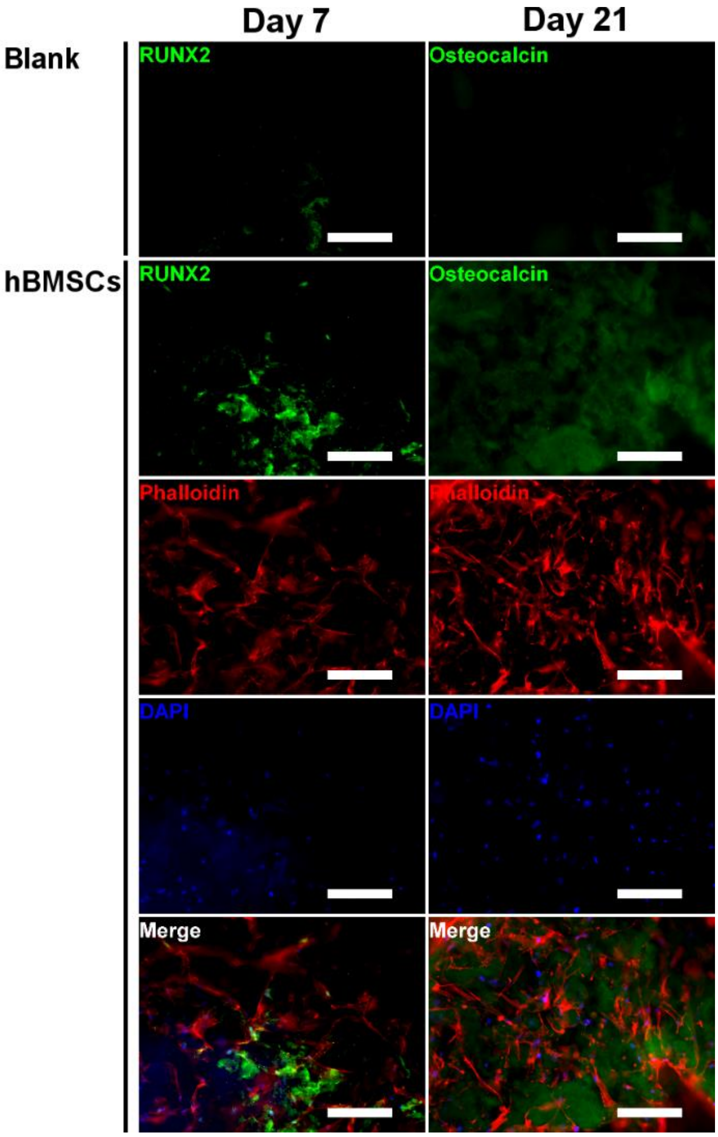

Figure 44. *Osteogenic differentiation of hBMSCs in 0 % nHA bioprints on days 7 and 21. Green channels for blank structure and structure with cells are taken with same exposure on each day and processed the same way on ImageJ. Scale bar 200 µm.*

In Figure 44, expression of RUNX2 and osteocalcin in blank structure and structure with cells of the 0 % nHA group are compared. In other words, difference between green channel of the blank structure and hBMSCs structure on days 7 and 21 is shown. Green channels for blank structure and structure with cells are taken with same exposure on each day and processed the same way on ImageJ. Based on Figure 44, osteocalcin expression might also be positive in the samples. Still, to summarize 3D immunostainings, osteogenic differentiation of the 3D bioprinted hBMSCs and the effect of nHA on that was not verified completely.

6. DISCUSSION

The incidence of bone defects is continuously increasing and the need for effective treatment strategies exists, as traditional treatment strategies, such as grafts, synthetic materials, and tissue engineered scaffolds have their limitations. 3D bioprinting is seen as a potential new solution in BTE to create natural tissue resembling large constructs. However, lack of ideal bioinks for 3D bioprinting is one of the greatest issues in the field. The aim of this thesis was to characterize the effect of different concentrations of nHA particles in an optimized multicomponent bioink for extrusion-based 3D bioprinting for bone applications.

6.1 Optimization of the biomaterial inks and printing conditions

The base components of the biomaterial inks were GelMA, gelatin, CNFs, and nHA particles. GelMA was chosen for its thermal and photo-crosslinking properties. Additionally, GelMA-based bioinks with mineral components have also been used in previous studies targeted to bone applications (Cidonio *et al.*, 2019; Byambaa *et al.*, 2017). IC was chosen for photocrosslinking of GelMA, as it has been found to be more cytocompatible than other existing photoinitiators (Pahoff et al., 2019; O'Connell et al., 2018; Levato et al., 2017). Gelatin and CNFs were used because of their preferred shear thinning and printability improving qualities (Lim *et al.*, 2020) and nHA was expected to support osteogenic differentiation of the cells in the bioinks (Gungor-Ozkerim *et al.*, 2018; Wang, Xiao-Fei *et al.*, 2016).

6.1.1 Optimization of the IC concentration in molded GelMA

Optimization of the inks started with the 4 % GelMA molding with different IC concentrations and UV exposure times, based on data from previous studies (Tables 1 and 2). Based on the GelMA molding tests, the UV exposure time needed for crosslinking was determined to be around 5 to 6 minutes. However, UV source used in crosslinking was different than that one later used in crosslinking after 3D bioprinting. Because of this, the results obtained were considered just guidance giving for future experiments. Photoinitiator concentration of 0.3 % was the only concentration which crosslinked well the molded GelMA. Based on literature review made (Table 2), 5 to 6 minutes UV exposure times and 0.3 % IC concentration have also been used earlier in castings or other forms.

Based on the experiment, temperature dependent gelation of GelMA was needed before or during the UV exposure, to initiate successful crosslinking. Gelatin and it´s modified version GelMA are thermo responsive materials that can be reversibly crosslinked at lower temperature due to the formation of triple helices and polypeptide chain networks (Gungor-Ozkerim *et al.*, 2018). When GelMA is in thermally crosslinked state, UV light induced irreversible crosslinking, where covalent bonds between methacrylate groups are formed, leaves the polypeptide chains in their entangled state. This leads to better crosslinking, when compared to photo-crosslinking of loose polypeptide network without thermal crosslinking. (Chansoria *et al.*, 2021)

The molding pilot made, together with the literature review gave guidance for the potential UV exposure time needed to crosslink GelMA and for suitable IC concentration. To achieve more accurate results, GelMA molding could have been repeated with 5 % GelMA, since the concentration of GelMA in the bioinks was later raised to that. With 5 % GelMA lower concentrations of IC might have been enough for successful crosslinking. The molding pilot could also have been made more systematically, and more repeats could have been done. For instance, it would have been good to repeat the first experiment (Table 6) so that all UV exposures would have been given on ice for the samples and observation made at the heat plate at 35 °C. Now the samples were kept on ice only 90 seconds and after that moved and observed at RT. In the made pilot, after first experiment, UV exposure time was also directly 5 – 6 minutes. Shorter exposure times could have been tested more. By this way more accurate information about the sufficient UV exposure time could have been achieved.

6.1.2 Optimization of 3D printing and crosslinking parameters

To find the optimal printing and crosslinking parameters, 3D printing pilots were conducted with the 1 % and 5 % nHA containing biomaterial inks. The pilots were done with the nHA having biomaterial inks, as the assumption was that the inks with nHA would require longer UV exposure time for crosslinking due to nHA, preventing transparency of the biomaterial inks (Lim *et al.*, 2020). The observed suitable IC concentration of 0.3 % was slightly higher than most of the concentrations reported in other 3D bioprinting studies (Table 1). As an exception, Krishnamoorthy *et al.* used higher 0.5 % IC concentration (Krishnamoorthy *et al.*, 2020). The UV exposure times used from 45 to 105 seconds after each printed layer are close to the values reported in other 3D bioprinting studies (Table 1).

Two UV light intensities and distances were tested in the 3D printing pilots from which 30.2 mm distance and 64 mW / cm^2 intensity was chosen for further studies (Table 13).

The decision to use 30.2 mm distance and 64 mW / cm^2 intensity was made, as the aim was to get the UV light head of the printer as close to the structure as possible, to ensure functional crosslinking also in corner areas of the structure with minimal UV exposure time. This was because of the area of the printer UV light was relatively small (can be seen in Figure 10 (B)) in single projection and no bigger structures than 10x10 mm were possible to crosslink with it. Continuous projection of the UV light head would have been faster and more efficient to use with bigger 30x30 mm 3D design in sample fabrication. However, continuous projection wasn’t effective enough to crosslink the biomaterial inks (Figure 18).

The 3D printing pilots also gave general idea on what kind of printing pressures, speeds, and temperatures were required for 3D printing of the biomaterial inks. During the 3D printing pilot of the 1 % nHA biomaterial ink, the printing temperature needed to be constantly changed during printing process from 23 to 26 °C which made the printing difficult. Printing temperature was stabilized to 26 °C and printability of the biomaterial inks was improved by raising GelMA and gelatin concentration to 5 %. By changing the concentration of a chosen polymer, viscosity of the bioink can be adjusted, which in turn helps to stabilize the printing temperature (Cui *et al.*, 2020). Temperature of 26 °C has also been used in other 3D bioprinting study where hBMSCs and ceramics were used in 3D bioprinting (Ojansivu *et al.*, 2019).

Based on imaging, stability of both 1% nHA and 5% nHA structures, made in the 3D printing pilots, was good and they did not disintegrate during incubation period (Figure 19). However, leakage of nHA from structures was observed, especially with the 5 % nHA biomaterial ink. The release of reversibly crosslinked gelatin from the structures might have caused partially nHA leakage, when nHA was flushed away with it. The release of nHA and disintegration of the structures might also be higher and faster with the group having higher concentration of nHA, as light induced crosslinking might be weaker in less transparent inks (Lim *et al.*, 2020).

It was also observed that in addition to UV exposure time, the thickness of the 3D printed filament affected the stability of the structures. The release of reversibly crosslinked gelatin might explain disintegration of the structures printed with thinner filament. Because of this, in future experiments as similar samples as possible with similar filament thicknesses were fabricated. Filaments printed were also intentionally kept relatively thick in the samples to ensure stability of the printed constructs.

Generally, UV crosslinking parameters and printing conditions were successfully optimized in 3D printing pilots with two nHA biomaterial inks. UV crosslinking was found to be effective but relatively time-consuming way to crosslink the biomaterial inks, as printing of several samples takes hours. The UV exposure time required for crosslinking of the biomaterial inks did not exceed times used in other studies (Table 1). However, most of the studies reported that they used UV crosslinking after 3D bioprinting of the whole structure (Table 1), not after each layer as in this thesis. The optimization phase of the project could have been continued even further, for instance, repeats with other groups could have been made. However, optimization of the biomaterial inks and printing conditions in this form took already big part from the whole study. If optimization would have been continued further, higher IC concentrations and shorter UV exposure times could have also been tested.

6.2 Preparation of the biomaterial inks and bioinks

Based on optimization, final mixing protocol of the biomaterial inks was specified. Despite optimization, the mixing protocol of the biomaterial inks still needs improvements. For instance, bubbles in the biomaterial inks were detected, especially in the 0 % nHA biomaterial ink (can be seen in Figure 24). However, all biomaterial inks might have had bubbles and they were just more visible in the transparent 0 % nHA biomaterial ink. Transparent hard clumps in the biomaterial inks were also detected in some mixing times, which complicated material extrusion in 3D bioprinting and caused needle clogging in some printing times. Transparent clumps were speculated to be either unmixed CNFs or GelMA. Batch to batch variation of GelMA in the mixing was also observed which might be explanation for occasional clumps in the biomaterial inks.

Biomaterial inks could be prefiltered by using syringe barrel and printing needle before IC and cell addition to get rid of the clumps in the future. Other option would be that even longer mixing times could be used, especially with CNFs. For instance, Ojansivu *et al.* mixed CNFs overnight (Ojansivu *et al.*, 2019). Addition of the biomaterial ink components also needs to be done very carefully, for instance addition of cold medium to the biomaterial ink caused nanocellulose separation/dissociation resulting non homogenous grainy biomaterial ink.

6.3 Characterization of the biomaterial inks

Various characterization methods for biomaterial inks and bioinks exist, but main aspects to consider are printability and viscosity of the inks (Morgan *et al.*, 2020; Matai *et al.*, 2020). In this thesis, the optimized biomaterial inks were characterized in terms of rheological properties, printability, and stability after crosslinking. In addition to used characterization methods, testing mechanical properties of the biomaterial inks after crosslinking and in incubation could have been a good addition to characterization. However, this was not executed, as 3D printed crosslinked structures made did not fulfil the geometries required for machinery measurements. In addition, casting of the biomaterial inks with UV crosslinking was difficult, due to nHA causing uneven crosslinking in a thick cast. The possible chemical interactions between nHA and the biomaterial inks could have also been evaluated by energy-dispersive X-ray spectroscopy or Fourier-transform infrared spectroscopy. The distribution of the nHA in the printed structures might have been possible to observe with micro-CT, to confirm the homogeneous distribution.

6.3.1 Rheological characterization of the biomaterial inks

The rheological behavior of bioinks is due to the physical, electrostatic, and biological interactions of components (Chopin-Doroteo *et al.*, 2021). Rheological measurements in this thesis focused on the viscosity, temperature dependency, and shear thinning properties of the developed biomaterial inks. Viscosity and shear-thinning characteristics of the bioink are crucial, especially in extrusion 3D bioprinting, since the bioink has to have smooth flow from the nozzle and after that it needs to be stabilized (Cui *et al.*, 2020; Groll *et al.*, 2019). Additionally, preferred viscosity for the bioink depends on what 3D bioprinting modality is used (Cui *et al.*, 2020). For cell viability, spreading, and activity, it's better that lower pressures are used in 3D bioprinting, which is possible with lower viscosities having bioinks (Matai *et al.*, 2020; Morgan *et al.*, 2020). It was expected, that higher nHA concentration in the biomaterial ink increases the viscosity, since ceramic phase in a bioink has been studied to increase the viscosity (Cidonio *et al.*, 2019; Wüst *et al.*, 2014).

The bioink temperature affects the viscosity of a bioink, as noncovalent interactions in the material are affected by environmental conditions, such as temperature, around them (Cui *et al.*, 2020). In "temperature sweep", all biomaterial ink groups presented lower viscosity at higher temperature (Figure 20 (A)). In addition, all bioinks presented radical increase in viscosity when temperature was decreased beyond 25 °C. This indicated that the lowest adequate printing temperature was 26 °C, even though a slightly higher temperature could have been optimal for the 5% nHA biomaterial ink. The temperature decrease caused the increase in viscosity, as gelatin and GelMA are thermo responsive materials, which undergo reversible crosslinking at lower temperature (Gungor-Ozkerim et al., 2018).

The increase in nHA concentration resulted in increase in viscosity, but it did not hinder the achieved shear-thinning properties. Other studies have also reported that ceramic phase in their bioinks increased the viscosity (Ojansivu *et al.*, 2019; Cidonio *et al.*, 2019; Wüst *et al.*, 2014). One possible explanation for viscosity increase might be that nHA particles can form electrostatic interactions between the particles in aqueous solutions. In addition to the concentration of nHA, smaller nHA particle size (20–80 nm) is reported to result higher viscosity of the material. (Ryabenkova *et al.*, 2017) As the 5 % nHA biomaterial ink had higher dry composition than other inks had, drying of the 5 % nHA biomaterial ink might also explain higher viscosity. In “flow sweep” measurements (Figure 20 (B)), viscosity decreased in all groups when shear rate increased, indicating shear thinning behaviour of the biomaterial inks. Low viscosity in high shear stress means that material can be easily printed and after the printing when shear stress is zero, it can recover to a higher viscosity.

Extracted viscosities (Figure 21) from “temperature sweep” and “flow sweep” measurements were from 11 to 147 Pa s. The viscosities of the biomaterial inks are rather low when compared to the limitations of the machinery, as for extrusion 3D bioprinting more viscous bioinks up to 300 000 Pa s are reported to be possible to print (Matai *et al.*, 2020; Derakhshanfar *et al.*, 2018; Hölzl *et al.*, 2016). Ojansivu *et al.* reported viscosities of their biomaterial inks consisting of alginate-gelatin with or without BaG or CNFs being from 56 ± 5 Pa s to 1143 ± 85 Pa s at 26 °C (Ojansivu *et al.*, 2019). These are close to results achieved in this project. Cidonio *et al.* studied biomaterial inks consisting of GelMA with or without nanoclay and the reported viscosities from ~0.1 to ~12 Pa s (“temperature sweep”, at 26 °C, shear rate 8 1/s, red from the figure) and from ~100 to ~300 Pa s (“flow sweep”, at 20.5 °C, shear rate 1 1/s, red from the figure) are also close to the results obtained in this thesis (Cidonio *et al.*, 2019). With shear rate 1 1/s and at 37 °C, Wüst *et al.* reported ~5 Pa s for 8 % (w/v) nHA, ~3 Pa s for 4 % nHA, and ~2 Pa s for the biomaterial ink without nHA (“flow sweep”, values red from the figure) (Wüst *et al.*, 2014). In this thesis, the 0% nHA biomaterial ink had ~8 Pa s and the 5 % nHA biomaterial ink ~14 Pa s viscosity at 37 °C with shear rate 1 1/s. The results differ a bit between each other. However, Wüst *et al.* studied alginate gelatin -based bioink where GelMA was not used (Wüst *et al.*, 2014). Other studies, where nHA was used in the bioink, did not report viscosities of their bioinks (Wang, Xiao-Fei *et al.*, 2016; Gao *et al.*, 2014).

It must be noticed that the addition of cells to the biomaterial inks has an effect on rheological properties (Lim *et al.*, 2020). Because of this, the achieved results do not completely correspond rheological properties of the bioinks. In rheological measurements, volume of cell suspension and IC could have been compensated for instance with medium addition, to achieve results corresponding more accurately bioinks.

6.3.2 Stability of the biomaterial inks

Crosslinking of a bioink during or after 3D bioprinting process is a way to ensure long-term stability of the construct. If crosslinking is not successful and remains uncomplete, unwanted rapid degradation and collapse of the construct can happen. (Cui *et al.*, 2020) Stability of the biomaterial inks and their degradation in incubation after 3D printing and crosslinking was estimated by incubating 3D printed structures, imaging them (Figure 22), and studying the release rate of gelatin from the structures (Figure 23). Expectations were that the release of gelatin and degradation of the structures would be higher and faster with groups having higher concentrations of nHA. This was because nHA has a decreasing effect on transparency of the biomaterial inks which may weaken light induced crosslinking (Lim *et al.*, 2020). Most of the gelatin was released in all groups on day 1 or right after the incubation was started (Figure 23). Gelatin was released from the structures, as it was crosslinked just by unstable thermal gelation (Gungor-Ozkerim *et al.*, 2018). The release of gelatin was similar between groups on day 1, indicating that nHA in structures had no effect on release rate. However, on day 3, 0 % nHA group had significantly lower and 5 % nHA group had significantly higher release of gelatin than other groups had, which was in line with expectations.

The results from BCA assay and imaging gave general view about the effect of nHA for crosslinking and stability. However, BCA assay measures general protein levels, not directly gelatin, and leaked nHA might have disturbed measurement made. The made BCA assay does not correspond directly degradation *in vivo* and, since incubation was done in DPBS, degradation profile might be different in medium and with cells. It would have been good to repeat the degradation study to verify results.

6.3.3 Printability of the biomaterial inks

The printability studies of the biomaterial inks included imaging of the structures and evaluation in a filament formation test, filament spreading, and buildability. Usually, high viscosity bioinks require higher printing pressures (Ji and Guvendiren 2017). As expectations were that nHA would increase the viscosity of the biomaterial inks, because of higher dry composition, higher concentration of nHA having biomaterial inks were expected to require higher printing pressure in the printability tests. However, similar printability properties between the biomaterial inks were expected. Higher printing pressure, 2.1 bar, was needed in 3D printing of the 5 % nHA group than with other groups (Table 9). However, faster printing speed was also used with the 5 % nHA biomaterial ink, which increased the need of higher printing pressure. On the other hand, the 3 %

nHA biomaterial ink was printed with the lowest speed (10.3 mm/s) and despite that, it required higher printing pressure (1.5 – 1.6) than 1 % and 0 % nHA biomaterial inks. The lowest pressure in 3D printing was used with 0 % nHA group (0.8 – 1.0 bar). The results indicate that, as expected, nHA in the biomaterial inks increases printing pressure needed. However, keeping the printing speed constant in the printability studies would have made the results easier to compare.

The filament formation was studied by extruding filaments with all biomaterial ink groups at 26 °C (Figure 24). Irregularities in the 5 % nHA group indicated that the biomaterial ink was too viscous for printing of smooth filaments at 26 °C. Same thing was observed when filament spreading was studied (Figure 25). Higher nHA concentrations having biomaterial inks (3 % and 5 %) had breaks in a printed filament. As the 5 % nHA biomaterial ink had higher dry composition than other inks had, drying of the 5 % nHA biomaterial ink might explain less smooth filament and breaks occurred in 3D printing. Humidity in the room was also non-controlled during the printability studies, which might have caused drying of the ink, drying of the nozzle, or drying of the printed structure. Pressures used might also have been too low, as the aim was to print as accurate filaments as possible, so that the best possible printing accuracy was achieved without filament spreading. On the other hand, pore size area of the 0 % and 5 % nHA biomaterial inks were closest to the theoretical pore area of the design. This indicates quick stabilization of the bioinks after shear thinning, which is an important feature for bioinks (Matai *et al.*, 2020). However, transparency of the 0 % nHA group affects the reliability of that group´s result since it was harder to calculate pore areas of the 0 % nHA group as it did not stand out from the background as much as other groups.

Buildability of the biomaterial ink groups was studied by 3D printing higher hollow geometrical structures (Figure 26) and in that, high viscosity of the 5 % nHA biomaterial inks was noticed to affect negatively on printability, as the structures were not as successfully printed as with other groups. Also, with the 3 % nHA biomaterial ink, the printed cylinders and cones were not as smooth as with the 0 % and 1 % nHA biomaterial inks. However, the highest 3D printed cylinders were achieved with the 1 % and 3 % nHA biomaterial inks.

The effect of nHA for printability of the biomaterial inks has not been reported much in previous studies (Wang, Xiao-Fei *et al.*, 2016; Wüst *et al.*, 2014; Gao *et al.*, 2014). Wüst *et al.* did only single layer analysis for nHA containing biomaterial inks to evaluate filament spreading. With nHA, the biomaterial inks were reported to be more inhomogenous and hydrogel was noticed to accumulate in the corners of the printed spiral. (Wüst *et al.*, 2014) Accumulation of the biomaterial inks to the corners of the structures was not observed in this thesis but similar observations about inhomogeneity of the high nHA having filaments were made. However, Wüst *et al.* stated that printability of the inks was maintained despite addition of high concentration of nHA (8 % w/v) (Wüst *et al.*, 2014), which was not observed in this study with the 5 % nHA biomaterial ink.

To summarize the printability studies made, high nHA concentration (higher than 3 %) affects negatively on printability. However, the printability of the other biomaterial inks, especially with the 0 % nHA and 1 % nHA biomaterial inks, was observed to be very good. Based on buildability studies (Figure 26), these biomaterial inks are also very promising for 3D bioprinting of even bigger hollow structures than tested ones. Achieved results from the printability studies are reliable, but the printability of the biomaterial inks does not directly correspond situation with the bioinks. The volume of cell suspension could have been compensated in the biomaterial inks in the printability studies. Now it was just partially compensated when crystal violet was added. Additionally, more repeats for lattice structures could have been made. Imaging of the structures was made with camera, and even if settings and camera distance was tried to be kept similar with all groups, some differences between groups exists. For instance, the 3 % nHA group was made on a different day than others, so distance from the sample to camera and other settings are not completely same with that.

6.4 Biological characterization

Printability and bioink´s effect on cell behavior and viability are crucial aspects to consider in the bioink development (Parak *et al.*, 2019). Other important aspects to consider are cell type and density used in the bioink (Cui *et al.*, 2020; Matai *et al.*, 2020). In this study, as in several other studies (Cidonio *et al.*, 2019; Ojansivu *et al.*, 2019; Byambaa *et al.*, 2017; Gao *et al.*, 2014), human bone marrow-derived mesenchymal stem cells were used. For 3D bioprinting of complex tissues like bone, use of stem cells makes the fabrication process easier and simpler, as then there’s no need for various bioinks with different cell types. Cell density in the bioink needs to be high enough to achieve enough viable cells after 3D bioprinting. (Matai *et al.*, 2020) In this project the density of the cells in the bioink, 5 million / ml, was relatively high when compared to other studies focused on 3D bioprinting of bone (Ojansivu *et al.*, 2019; Byambaa *et al.*, 2017; Wang, Xiao-Fei *et al.*, 2016).

In 3D bioprinting, cellular component in the bioinks was found to influence the needed printing pressure (Table 11) and the stability of the structures in incubation (Figures 27 and 34 (B)). In all groups, lower pressures were needed in 3D bioprinting when compared to the 3D printing of the biomaterial ink of the same group (Table 11). Additionally, the 5 % nHA group required higher printing pressure (0.9 bar) than other groups, as in printability studies. This was expected because of the higher viscosity of the 5 % nHA biomaterial ink. Printing pressure did not differ much between the 0 % and 1 % nHA bioinks. All in all, used pressures in 3D bioprinting were relatively low from 0.4 to 0.9 bar. Earlier studies, where nHA was used in a bioink and extrusion-based 3D bioprinting was used, did not report pressure or speed, which they used in 3D bioprinting (Wang, Xiao-Fei *et al.*, 2016; Wüst *et al.*, 2014).

In terms of stability, structures with hBMSCs looked more disintegrated or grainy and had thinner filament after incubation periods (Figures 27 and 34 (B)). As said earlier, the addition of cells to the biomaterial inks might have an effect on rheological properties, but also on crosslinking efficiency (Lim *et al.*, 2020), hence, it might be that structures with cells were not totally crosslinked and disintegrated faster in incubation. Another possibility is that hBMSCs remodeled and disintegrated their surrounding bioink during incubation.

6.4.1 Cell viability and proliferation

In this project, it was expected that equal or even better cell viability would be observed in nHA groups than in the 0 % nHA group, as nHA in a bioinks has been studied to support cell viability and proliferation (Wang, Xiao-Fei *et al.*, 2016; Wüst *et al.*, 2014; Gao *et al.*, 2014). On the other hand, too high concentration of nHA in the bioink was expected to cause decreased cell viability, as the viscosity of it was expected to be high for 3D bioprinting causing high shear stress on cells (Matai et al., 2020; Morgan et al., 2020). Bioinks with low viscosity have been reported to support cell viability better than bioinks with high viscosity (Ashammakhi *et al.*, 2019). In the 3D bioprinting pilot, it was expected that longer UV exposure times used, would decrease cell viability. This was expected, as light induced crosslinking with UV light and photoinitiator IC can be cytotoxic for the cells, if excess exposures and amounts of those are used (Lim *et al.*, 2019; Stratesteffen *et al.*, 2017; Williams *et al.*, 2005). The cytotoxicity of IC is due to formation of high-energy radical species (discussed in chapter 2.3.2.1), which can cause oxidative damage for cells (Williams *et al.*, 2005). UV light in turn can cause, for instance, production of reactive oxygen species, which can cause oxidative damage or breaks in the deoxyribonucleic acid (DNA) of cells (Urushibara *et al.*, 2014).

Multiple factors can affect cell viability in 3D bioprinting. First, 3D bioprinting itself is a hard process for cells where, for instance, too high printing pressure may affect negatively on cell viability (Matai *et al.*, 2020). Printing temperature must also be suitable for used cells. In this project, 3D bioprinting of each group took from one to three hours, so cells needed to survive relatively long time in the syringe barrels without proper nutrient or oxygen supply. In extrusion 3D bioprinting the cell membrane of the hBMSCs can also be mechanically damaged, since the cells experience high shear stress in the nozzle (Lim *et al.*, 2020). In this project, after 1 and 3 days, several dead cells were observed in all groups possibly because of the stressful printing process (Figures 28 and 35).

In this thesis, UV crosslinking was found to decrease cell viability, especially if longer exposure times were used. For instance, the cell viability of hBMSCs was observed to be lower in the 1st printed layer of the bioprints, which got the longest UV exposure, when compared to 4th or upper layers of the bioprints (Figures 29 and 36). Also, in the 3D bioprinting pilot, viability of the cells decreased with increasing the UV exposure time (Figure 28). Stratesteffen *et al.* also reported decreased cell viability of hMSCs in GelMA hydrogels if UV light induced crosslinking was used with excessive exposure times (Stratesteffen *et al.*, 2017). Due to cytotoxic radical species possibly left after crosslinking, samples are recommended to be washed after light exposure (Lim *et al.*, 2020). Washing of the structures after crosslinking could have been done to improve cell viability even better. Now only short DPBS wash was done for some of the prints to detach them from the printing dish and this was not done systematically to all samples.

In addition to 3D bioprinting and UV crosslinking, bioink properties, such as cell type and used materials, affect cell viability (Ashammakhi *et al.*, 2019). In this project, the effect of nHA particles in the bioinks was studied. The cells 3D bioprinted with the highest nHA concentration (5 %) had decreased viability through 21 days in culture (Figure 35). Cells in the structures that had 0 % or 1 % nHA concentration maintained high viability from day 1 to day 21 and there was no obvious difference between the groups. However, quantification of live/dead assay was not done, and the results were just visually inspected. Wang *et al.* reported similar results in their study where 1 wt% nHA concentration having bioink was compared to a bioink without nHA. Here, the viability was assessed at 1 and 7 days after bioprinting. (Wang, Xiao-Fei *et al.*, 2016) Gao *et al.* reported that a higher cell viability was observed in hBMSCs 3D bioprinted with nHA (2% w/v) when compared to a bioink with BaG and a bioink without BaG or nHA. Their viability assay was done only 24 hours after bioprinting. (Gao *et al.*, 2014) Higher concentrations of nHA, as 5 % nHA in this study represents, decrease cell viability possibly due to high shear stress in 3D bioprinting and high bioink viscosity (Figure 20). On the contrary, Wüst *et al.* reported in their study that even 8 % (w/v) nHA concentration in their alginate-gelatin bioink didn´t decrease cell viability of hMSCs (Wüst *et al.*, 2014). Because of this, in this thesis, the decrease in viability might be due to other reasons than just the high nHA concentration. However, Wüst *et al.* made their viability assessments 3 days after printing, which is relatively short time to follow the samples (Wüst *et al.*, 2014).

Crosslinking efficiency and material degradation rate in incubation affects cell leakage from the structures. In this study, cell leakage from the structures during incubation might have seemed like decreased cell viability, as some cell leakage was observed in all nHA groups (Figure 34 (B)). However, the bottoms of the well-plates were just briefly observed on day 21, and the images taken are not sufficient for evaluation of differences between the bioinks. With the 5 % nHA bioink, cell leakage might have been higher, if it was less crosslinked than other groups, as BCA assay results suggest (Figure 23). Insufficient nutrient and oxygen supply during incubation might also be one explaining factor why cell viability was decreased in 1st printed layers of the bioprints, as this side of the print was towards the bottom of the wells in incubation.

Overall, most of the hBMSCs survived from 3D bioprinting, as a good number of live cells was left after each 3D bioprinting. During 21 days of culture, especially 0 % and 1 % nHA bioinks were observed to be cytocompatible and supporting cell viability. Results obtained are reliable data for evaluation of cell viability in bioprinted constructs. However, in the future live/dead staining would be good to repeat with cells from another donor, to see whether similar results are obtained. Also, more than one sample per timepoint day could have been evaluated. Despite the expectation that the cells are evenly distributed in the bioink and the bioprinted samples were similar with each other inside each group, some variation between might have occurred. In the 3D bioprinting pilot on day 1, images presented from the structures (Figure 28) might be from different sides of the prints, as difference in cell viability between lower and upper layers was noticed on day 7.

In the 3D bioprinting pilot, the metabolic activity or proliferation of the hBMSCs was expected to be better with shorter 45 seconds UV exposure time. Contradicting, on days 1 and 3, the metabolic activity was observed to be higher in 75 and 90 second UV exposure groups, when compared to other groups (Figure 30). However, decreasing mitochondrial activity was observed in these groups from day 1 to day 7 and at 14 days, the metabolic activity was highest in 45 seconds UV exposure group, as expected. However, it must be noticed, that for this data statistical significance of the results was not analysed, and the sample amount of each group was only 4 bioprint pieces which were cut by hand. This causes relatively high standard deviation in the data from the pilot.

In the 3D bioprinting of 0 %, 1 %, and 5 % nHA bioink groups, it was expected that nHA in a bioink would support cell proliferation of hBMSCs. On days 1, 3, 7, and 21, relative proliferation was significantly higher both in the 0 % and 1 % nHA bioinks than in the 5 % nHA bioink (Figure 38). This result goes hand in hand with the results from L/D staining (Figure 35). On day 21, relative proliferation of hBMSCs in the 1 % nHA bioink was significantly higher than in 0 % or 5 % nHA bioinks. With the 1 % nHA bioink, metabolic activity of the cells remained at quite similar level, whereas the 0 % and 5 % nHA bioinks showed decreased mitochondrial activity from day 7 to day 21. These results indicate that 1 % nHA concentration in the bioink, enhanced metabolic activity of the hBMSCs. Wang *et al.* reported in their study that proliferation of human adipose derived stem cells was not different between nHA having bioink and without nHA having bioink and the cells proliferated well in both bioinks. This was based on comparison of live/dead assays from day 1 and 7. (Wang, Xiao-Fei *et al.*, 2016) Gao *et al.* reported that in their study proliferation of hMSCs was not observed during the differentiation, based on the DNA content normalized to scaffold dry weigh (Gao *et al.*, 2014).

Based on live/dead staining (Figure 35), the number of live cells was very low in last days of culture in the 5 % nHA group. This might explain also the decreased and lower metabolic activity of the group. With the 0 % nHA group, decreasing metabolic activity of the hBMSCs in last days of culture is harder to explain, as in this group viability of the cells was as good as with the 1 % nHA group. Decreased metabolic activity might also mean differentiation of the hBMSCs in the samples (Ruijtenberg and van den Heuvel 2016). Proliferation assay would be good to repeat to verify the results, and sample number (n=8) could be even higher, as the samples were cut by hand. However, 1 % nHA group gave promising results about proliferation of the hBMSCs and showed that suitable concentrations of nHA are beneficial and support cells in terms of viability and proliferation.

6.4.2 Cytotoxicity of the printing process and bioinks

When cells are damaged or died, LDH enzyme is released from their cytoplasm to culture medium. It was expected that both in the 3D bioprinting pilot and in the 3D bioprinting of nHA bioinks, LDH production would be higher on day 1, after stressful 3D bioprinting process for cells, and would then decrease. Longer UV exposure times were expected to cause increased LDH production by cells, as UV light and IC can be cytotoxic to cells, if excess exposures are used (Stratesteffen *et al.*, 2017; Lim *et al.*, 2016). LDH production by cells was also expected to be higher in the 5 % nHA bioink, than in the other groups, as high nHA concentration was known to cause higher shear stress creating harder circumstances for hBMSCs in 3D bioprinting.

In the 3D bioprinting pilot (Figure 31) and in 3D bioprinting of nHA groups (Figure 39), as expected, normalized LDH production by cells decreased in all groups from day 1 to day 7 after bioprinting. This indicates that the cells recovered from the 3D bioprinting process and crosslinking. In the 3D bioprinting pilot, on days 1 and 3, higher LDH production by cells was observed with 45- and 60 seconds UV exposure time groups, when compared to 75- and 90 seconds groups (Figure 31). On the contrary, on day 7, the 45 seconds UV exposure time group had the lowest LDH production, which was in line with expectations. However, it must be noted, that statistical significance of these results was not analysed.

In the 3D bioprinting of nHA groups (Figure 39), as expected, on day 1, the 5 % nHA bioink had significantly higher LDH production by cells than the 0 % and 1 % groups had. Other studies, where GelMA was used as a bioink backbone with mineral components or where nHA was used in a bioink, have not reported results related to LDH production or cytotoxicity (Cidonio *et al.*, 2019; Byambaa *et al.*, 2017; Wang, Xiao-Fei *et al.*, 2016; Wüst *et al.*, 2014; Gao *et al.*, 2014). However, the colorimetric reaction of the LDH assay was very fast, only 3 samples from each group were analyzed, and samples needed to be diluted. Fast color reaction and a small pipetting delay in the reaction plates might have affected standard deviation and results. Because of this, achieved results can only be considered giving general view and the measurement would be good to repeat.

6.4.3 Cell morphology and osteogenic differentiation

Morphology of hBMSCs can vary from small and triangular to elongated, fibroblast-like, spindle-like or large and flattened morphology (Haasters *et al.*, 2009). Typical morphology for osteoblasts is more cuboidal (Rutkovskiy *et al.*, 2016). In the 3D bioprinting pilot (Figure 32), no obvious differences between groups in cell morphology were not observed and the cells were elongated and spread into the 3D space of the bioink. After 3D bioprinting of the 0 %, 1 %, and 5 % nHA bioink groups (Figures 40 and 41), the hBMSCs were elongated, branched, and had a fine cell morphology typical for hBMSCs. On day 21 (Figure 41), especially fine morphology of hBMSCs was observed in the 1 % nHA group. However, nHA was not observed to have a considerable effect on cell morphology. Cell spreading into the 3D space of the bioinks was better, when compared to hBMSCs in the 3D bioprinting pilot. This was probably because of OM used in the sample culture, as in the 3D bioprinting pilot only BM was used. Achieved results handling morphology were exceptional in that sense that often such nice spreading and morphology is not observed. In several other studies where bioinks with ceramics were used, cells remained round-like after 3D bioprinting (Ojansivu *et al.*, 2019; Cidonio *et al.*, 2019; Ahlfeld *et al.*, 2017; Wang, Xiao-Fei *et al.*, 2016; Wüst *et al.*, 2014).

Mechanical properties and structure of the hydrogel system can have an effect on the morphology of hMSCs (Lee *et al.*, 2013). This is because of the process called mechanotransduction, where physical forces turn into biochemical signals in the cells affecting cellular responses. In practice, cytoskeleton of the cells in linked to the external mechanical environment through protein interactions. (Huang, H. *et al.*, 2004) The morphology of the hBMSCs in this thesis indicates that mechanical stiffness and properties of the materials used are suitable for the cells. Furthermore, external stress, matrix mechanics, cell shape, and chemical stimuli affect hMSC differentiation dictating their fate determination (Duarte Campos *et al.*, 2015). The effect of mechanical properties has been studied to have a crucial impact on bone regeneration and resorption process and on osteogenic differentiation of hMSCs (Duarte Campos *et al.*, 2015; Huang, C. and Ogawa 2010).

Osteogenic differentiation of the 3D bioprinted hBMSCs of all nHA groups was studied by doing immunostainings for visualization of early phase osteogenic marker RUNX2 and late phase osteogenic marker osteocalcin (Figures 42 and 43). It was expected that nHA in a bioink would support osteogenic differentiation of the cells, as nHA and other ceramics have been shown to support osteogenic differentiation of hBMSCs (Ojansivu *et al.*, 2019; Gungor-Ozkerim *et al.*, 2018; Wang, Xiao-Fei *et al.*, 2016; Gao *et al.*, 2014). This is because ceramics, like nHA particles, ensure bioactivity of a bioink providing nucleation sites in the bioinks (Gkioni *et al.*, 2010). These nucleation sites provide both cell adhesion sites and formation of a mineralized matrix. (Alipour *et al.*, 2021; Gkioni *et al.*, 2010; Rea *et al.*, 2004). Hydroxyapatite has been studied to be osteoinductive material, which induces expression of osteo-specific genes (Lin, L. *et al.*, 2009).

Both used antibodies had strong background staining for the biomaterials. With RUNX2, despite strong background staining, possible positive expression located to nuclei and cytoplasm of the hBMSCs was observed in all groups (Figure 42). RUNX2 is usually located to nuclei of the cells and its cytoplasmic expression is not understood well. However, it has been studied that RUNX2 might be detected in the cytoplasm if the microtubules of the cells are stabilized. (Pockwinse *et al.*, 2006) In the 3D bioprinting pilot, expression localized to nuclei was not observed so clearly, which was expected as sample culture was done in BM in the pilot.

Osteocalcin is a protein secreted by osteoblasts to the ECM of bone (Pawlina and Ross 2016). In this study, expression of osteocalcin was not possible to verify in the samples from day 21 (Figure 43). Some green areas were detected but it was challenging to distinguish between positive expression of osteocalcin and background staining of the material. Day 21 osteocalcin expression in 2D control hBMSCs was also weak indicating that the used antibody might have been inoperative. Based on Figure 44, where blank structure and structure with hBMSCs are compared, osteocalcin expression might also be positive in the samples.

To summarize the results of the immunostainings, osteogenic differentiation of the 3D bioprinted hBMSCs and the effect of nHA on that was not successfully confirmed and verified. From the results, it´s not possible to say which group had the best osteogenic differentiation or did nHA induce osteogenic differentiation. The effect of nHA in the bioink to osteogenic potential needs more studies. 3D immunostaining protocol made in the project needs further optimization, for instance even longer washings after antibodies and secondaries could be used. Now background staining of the biomaterials was strong and for instance DAPI stained CNFs in the structures. Concentrations of the used antibodies, secondaries, and other staining protocol reagents could also be evaluated again to verify their sufficiency for thick 3D samples. Other antibodies specific for other osteogenic markers could also be tested. Additionally, secondary control (samples stained without primary antibody) for 3D immunostainings was not used, which would have been highly beneficial and is needed in future studies. For imaging, confocal microscope could be used to penetrate deeper in a 3D sample and to achieve better quality images. In the future, 3D immunostainings need to be repeated with the same cells and with cells from another donor to verify the results. Gene assay by quantitative polymerase chain reaction (qPCR) and protein production study (western plot) could have also been done to evaluate the osteogenic differentiation even better.

7. CONCLUSIONS AND FUTURE PROSPECTS

In this thesis, multicomponent bioinks supplemented with nHA for extrusion-based 3D bioprinting of bone were developed and studied. The effect of different concentrations of nHA particles in the bioinks was characterized and biological responses of hBMSCs embedded in the developed bioinks were investigated. Additionally, crosslinking for bioinks, based on light induced UV crosslinking and photoinitiator IC, was used. It was hypothesized that the increased concentration of nHA would induce osteogenic differentiation of hBMSCs. However, high concentration of nHA was expected to increase the viscosity of the bioink, decreasing the printability and causing high shear stress on cells in 3D bioprinting.

In material characterization, as expected, high nHA concentration in the biomaterial ink increased viscosity, which impaired printability. However, printability of the other biomaterial inks, especially with the 0 % nHA and 1 % nHA biomaterial inks, was observed to be very good. These biomaterial inks are also very promising for 3D bioprinting of bigger hollow structures. Viscosity of the biomaterial inks decreased in all groups when shear rate increased, indicating shear thinning behaviour of the biomaterial inks. Bioinks and biomaterial inks, especially the 0 % and 1 % nHA groups, were also easily extrudable with relatively low pressure. Additionally, stability of all groups after 3D bioprinting was excellent and the structures lasted up to three weeks.

In crosslinking, UV exposure time 45 seconds for each printed layer and IC concentration of 0.3 % were found to be most functional in this study and having the most minimal impact for cell viability and proliferation. Shorter UV exposure times tried in this study did not initiate successful crosslinking. However, further optimization of UV crosslinking in the future is needed, so that cell viability also in lower layers of the structures is ensured.

High cell viability and proliferation, when compared to other groups, was observed in the 1 % nHA bioink. Additionally, cell morphology of the hBMSCs was as expected from hBMSCs and the cells were spreading nicely in the bioinks, which is seldomly demonstrated in other studies. Because of high viscosity, the 5 % nHA bioink was found to cause high shear stress for cells and leading to decrease in cell viability and proliferation, as expected. The effect of nHA on osteogenic differentiation of hBMSCs in the bioinks remains to be solved, as only possible expression of RUNX2 was detected. Because of this, the effect of nHA to osteogenic potential needs more studies and suitable methods for this could be further optimized new immunostainings and for instance, qPCR. Additionally, to verify reliability of experiments made with cells, hBMSCs from another donor could be used in 3D bioprinting. Biological characterization for 3 % or 2 % nHA having bioinks could also be done to see their effect for cells and whether it differs or is better when compared to the 1 % nHA bioink.

To conclude, the bioink with 1 % nHA was found to have excellent properties in terms of material properties and cell viability. Based on results, it was shown that 1 % nHA in the bioink enhanced cell viability and proliferation of hBMSCs. The bioink had also excellent properties in terms of rheology, printability, and stability for extrusion 3D bioprinting. After further studies, the developed multicomponent bioink together with UV crosslinking can potentially be used in 3D bioprinting for bone applications.

REFERENCES

Ahlfeld T., Cidonio G., Kilian D., Duin S., Akkineni A.R., Dawson J.I., Yang S., Lode A., Oreffo R.O.C. & Gelinsky M. (2017) Development of a clay based bioink for 3D cell printing for skeletal application. Biofabrication 9(3), p. 034103.

Alipour M., Firouzi N., Aghazadeh Z., Samiei M., Montazersaheb S., Khoshfetrat A.B. & Aghazadeh M. (2021) The osteogenic differentiation of human dental pulp stem cells in alginate-gelatin/Nano-hydroxyapatite microcapsules. BMC Biotechnology 21(6).

Amini A.R., Laurencin C.T. & Nukavarapu S.P. (2012) Bone Tissue Engineering: Recent Advances and Challenges. Critical Reviews in Biomedical Engineering 40(5), pp. 363–408.

Ashammakhi N., Hasan A., Kaarela O., Byambaa B., Sheikhi A., Gaharwar A.K. & Khademhosseini A. (2019) Advancing Frontiers in Bone Bioprinting. Advanced Healthcare Materials 8(7), p. 1801048.

Barati D., Kader S., Pajoum Shariati S.R., Moeinzadeh S., Sawyer R.H. & Jabbari E. (2017) Synthesis and Characterization of Photo-Cross-Linkable Keratin Hydrogels for Stem Cell Encapsulation. Biomacromolecules 18(2), pp. 398–412.

Bartnikowski M., Bartnikowski N.J., Woodruff M.A., Schrobback K. & Klein T.J. (2015) Protective effects of reactive functional groups on chondrocytes in photocrosslinkable hydrogel systems. Acta Biomaterialia, pp. 66–76.

Basha R.Y., Kumar T.S.S. & Doble M. (2015) Design of biocomposite materials for bone tissue regeneration. Materials Science and Engineering: C 57, pp. 452–463.

Byambaa B., Annabi N., Yue K., Santiago G.T., Alvarez M.M., Jia W., Kazemzadeh-Narbat M., Shin S.R., Tamayol A. & Khademhosseini A. (2017) Bioprinted Osteogenic and Vasculogenic Patterns for Engineering 3D Bone Tissue. Advanced Healthcare Materials 6(16).

Chansoria P., Asif S., Polkoff K., Chung J., Piedrahita J.A. & Shirwaiker R.A. (2021) Characterizing the Effects of Synergistic Thermal and Photo-Cross-Linking during Biofabrication on the Structural and Functional Properties of Gelatin Methacryloyl (GelMA) Hydrogels. ACS Biomaterials Science & Engineering. Available at: https://pubs.acs.org/doi/10.1021/acsbiomaterials.1c00635 (Accessed: October 18, 2021)

Choi B.Y., Chalisserry E.P., Kim M.H., Kang H.W., Choi I. & Nam S.Y. (2019) The Influence of Astaxanthin on the Proliferation of Adipose-derived Mesenchymal Stem Cells in Gelatin-Methacryloyl (GelMA) Hydrogels. Materials 12(15), p. 2416.

Chopin-Doroteo M., Mandujano-Tinoco E.A. & Krötzsch E. (2021) Tailoring of the rheological properties of bioinks to improve bioprinting and bioassembly for tissue replacement. Biochimica Et Biophysica Acta (BBA) - General Subjects 1865(2), p. 129782.

Cidonio G., Alcala-Orozco C.R., Lim K.S., Glinka M., Mutreja I., Kim Y., Dawson J.I., Woodfield T.B.F. & Oreffo R.O.C. (2019) Osteogenic and angiogenic tissue formation in high fidelity nanocomposite Laponite-gelatin bioinks. Biofabrication 11(3), p. 035027.

Cidonio G., Glinka M., Kim Y., Kanczler J., Lanham S.A., Ahlfeld T., Lode A., Dawson J.I., Gelinsky M. & Oreffo R. (2020) Nanoclay-based 3D printed scaffolds promote vascular ingrowth ex vivo and generate bone mineral tissue in vitro and in vivo. Biofabrication 12(3), p. 035010.

Costantini M., Colosi C., Święszkowski W. & Barbetta A. (2019) Co-axial wet-spinning in 3D bioprinting: state of the art and future perspective of microfluidic integration. Biofabrication 11(1), p. 012001.

Cui X., Li J., Hartanto Y., Durham M., Tang J., Zhang H., Hooper G., Lim K. & Woodfield T. (2020) Advances in Extrusion 3D Bioprinting: A Focus on Multicomponent Hydrogel-Based Bioinks. Advanced Healthcare Materials 9(15), p. 1901648.

Dababneh A.B. & Ozbolat I.T. (2014) Bioprinting Technology: A Current State-of-the-Art Review. Journal of Manufacturing Science and Engineering 136(6), p. 061016.

Deligkaris K., Tadele S.T., Olthuis W. & van der Berg A. (2010) Hydrogel-based devices for biomedical applications. Sensors and Actuators B: Chemical 147(2), pp. 765–774.

Derakhshanfar S., Mbeleck R., Xu K., Zhang X., Zhong W. & Xing M. (2018) 3D bioprinting for biomedical devices and tissue engineering: A review of recent trends and advances. Bioactive Materials 3(2), pp. 144–156.

Duarte Campos D.F., Blaeser A., Korsten A., Neuss S., Jaekel J., Vogt M. & Fischer H. (2015) The Stiffness and Structure of Three-Dimensional Printed Hydrogels Direct the Differentiation of Mesenchymal Stromal Cells Toward Adipogenic and Osteogenic Lineages. Tissue Engineering Part A 21(3–4), pp. 740–756.

Eke G., Mangir N., Hasirci N., MacNeil S. & Hasirci V. (2017) Development of a UV crosslinked biodegradable hydrogel containing adipose derived stem cells to promote vascularization for skin wounds and tissue engineering. Biomaterials 129, pp. 188–198.

Fedorovich N.E., Kuipers E., Gawlitta D., Dhert W.J.A. & Alblas J. (2011) Scaffold Porosity and Oxygenation of Printed Hydrogel Constructs Affect Functionality of Embedded Osteogenic Progenitors. Tissue Engineering Part A 17(19–20), pp. 2473–2486.

Gao G., Schilling A.F., Yonezawa T., Wang J., Dai G. & Cui X. (2014) Bioactive nanoparticles stimulate bone tissue formation in bioprinted three-dimensional scaffold and human mesenchymal stem cells. Biotechnology Journal 9(10), pp. 1304–1311.

Gkioni K., Leeuwenburgh S.C., Douglas T.E., Mikos A.G. & Jansen J.A. (2010) Mineralization of Hydrogels for Bone Regeneration. Tissue Engineering Part B: Reviews 16(6), pp. 577–585.

Groll J., Burdick J.A., Cho D.-W., Derby B., Gelinsky M., Heilshorn S.C., Jüngst T., Malda J., Mironov V.A., Nakayama K., Ovsianikov A., Sun W., Takeuchi S., Yoo J.J. & Woodfield T.B.F. (2019) A definition of bioinks and their distinction from biomaterial inks. Biofabrication 11(1), p. 013001.

Groll J., Boland T., Blunk T., Burdick J.A., Cho D., Dalton P.D., Derby B., Forgacs G., Li Q., Mironov V.A., Moroni L., Nakamura M., Shu W., Takeuchi S., Vozzi G., Woodfield

T.B.F., Xu T., Yoo J.J. & Malda J. (2016) Biofabrication: reappraising the definition of an evolving field. Biofabrication 8(1), p. 013001.

Gungor-Ozkerim P.S., Inci I., Zhang Y.S., Khademhosseini A. & Dokmeci M.R. (2018) Bioinks for 3D bioprinting: an overview. Biomaterials Science 6(5), pp. 915–946.

Haasters F., Prall W.C., Anz D., Bourquin C., Pautke C., Endres S., Mutschler W., Docheva D. & Schieker M. (2009) Morphological and immunocytochemical characteristics indicate the yield of early progenitors and represent a quality control for human mesenchymal stem cell culturing. Journal of Anatomy 214(5), pp. 759–767.

Hölzl K., Lin S., Tytgat L., Vlierberghe S.V., Gu L. & Ovsianikov A. (2016) Bioink properties before, during and after 3D bioprinting. Biofabrication 8(3), p. 032002.

Huang C. & Ogawa R. (2010) Mechanotransduction in bone repair and regeneration. The FASEB Journal 24(10), pp. 3625–3632.

Huang H., Kamm R.D. & Lee R.T. (2004) Cell mechanics and mechanotransduction: pathways, probes, and physiology. American Journal of Physiology - Cell Physiology 287(1), pp. C1–C11.

Ji S. & Guvendiren M. (2017) Recent Advances in Bioink Design for 3D Bioprinting of Tissues and Organs. Frontiers in Bioengineering and Biotechnology 5(23).

Jung J. & Oh J. (2014) Influence of photo-initiator concentration on the viability of cells encapsulated in photo-crosslinked microgels fabricated by microfluidics. Digest Journal of Nanomaterials and Biostructures 9(2), pp. 503–509.

Jungst T., Smolan W., Schacht K., Scheibel T. & Groll J. (2016) Strategies and Molecular Design Criteria for 3D Printable Hydrogels. Chemical Reviews 116(3), pp. 1496–1539.

Kang L.H., Armstrong P.A., Lee L.J., Duan B., Kang K.H. & Butcher J.T. (2017) Optimizing Photo-Encapsulation Viability of Heart Valve Cell Types in 3D Printable Composite Hydrogels. Annals of Biomedical Engineering 45(2), pp. 360–377.

Krishnamoorthy S., Wadnap S., Noorani B., Xu H. & Xu C. (2020) Investigation of gelatin methacrylate working curves in dynamic optical projection stereolithography of vascular-like constructs. European Polymer Journal 124, p. 109487.

Leberfinger A.N., Ravnic D.J., Dhawan A. & Ozbolat I.T. (2017) Concise Review: Bioprinting of Stem Cells for Transplantable Tissue Fabrication. Stem Cells Translational Medicine 6(10), pp. 1940–1948.

Lee J., Abdeen A.A., Zhang D. & Kilian K.A. (2013) Directing stem cell fate on hydrogel substrates by controlling cell geometry, matrix mechanics and adhesion ligand composition. Biomaterials 34(33), pp. 8140–8148.

Levato R., Visser J., Planell J.A., Engel E., Malda J. & Mateos-Timoneda M.A. (2014) Biofabrication of tissue constructs by 3D bioprinting of cell-laden microcarriers. Biofabrication 6(3), p. 035020.

Levato R., Webb W.R., Otto I.A., Mensinga A., Zhang Y., van Rijen M., van Weeren R., Khan I.M. & Malda J. (2017) The bio in the ink: cartilage regeneration with bioprintable hydrogels and articular cartilage-derived progenitor cells. Acta Biomaterialia 61, pp. 41–53.

Li Y., Li D., Lu B., Gao D. & Zhou J. (2015) Current status of additive manufacturing for tissue engineering scaffold. Rapid Prototyping Journal 21(6), pp. 747–762.

Lim K.S., Galarraga J.H., Cui X., Lindberg G.C.J., Burdick J.A. & Woodfield T.B.F. (2020) Fundamentals and Applications of Photo-Cross-Linking in Bioprinting. Chemical Reviews 120(19), pp. 10662–10694.

Lim K.S., Klotz B.J., Lindberg G.C.J., Melchels F.P.W., Hooper G.J., Malda J., Gawlitta D. & Woodfield T.B.F. (2019) Visible Light Cross-Linking of Gelatin Hydrogels Offers an Enhanced Cell Microenvironment with Improved Light Penetration Depth. Macromolecular Bioscience 19(6), p. 1900098.

Lim K.S., Levato R., Costa P.F., Castilho M.D., Alcala-Orozco C.R., van Dorenmalen K.M.A., Melchels F.P.W., Gawlitta D., Hooper G.J., Malda J. & Woodfield T.B.F. (2018) Bio-resin for high resolution lithography-based biofabrication of complex cell-laden constructs. Biofabrication 10(3), p. 034101.

Lim K.S., Schon B.S., Mekhileri N.V., Brown G.C.J., Chia C.M., Prabakar S., Hooper G.J. & Woodfield T.B.F. (2016) New Visible-Light Photoinitiating System for Improved Print Fidelity in Gelatin-Based Bioinks. ACS Biomaterials Science & Engineering 2(10), pp. 1752–1762.

Lin L., Chow K.L. & Leng Y. (2009) Study of hydroxyapatite osteoinductivity with an osteogenic differentiation of mesenchymal stem cells. Journal of Biomedical Materials Research Part A 89(2), pp. 326–335.

Lin N. & Dufresne A. (2014) Nanocellulose in biomedicine: Current status and future prospect. European Polymer Journal 59, pp. 302–325.

Loai S., Kingston B.R., Wang Z., Philpott D.N., Tao M. & Cheng H.M. (2019) Clinical Perspectives on 3D Bioprinting Paradigms for Regenerative Medicine. Regenerative Medicine Frontiers 1e190004.

Lou Y., Kanninen L., Kuisma T., Niklander J., Noon L.A., Burks D., Urtti A. & Yliperttula M. (2014) The Use of Nanofibrillar Cellulose Hydrogel As a Flexible Three-Dimensional Model to Culture Human Pluripotent Stem Cells. Stem Cells and Development 23(4), pp. 380–392.

Markstedt K., Mantas A., Tournier I., Martínez Ávila H., Hägg D. & Gatenholm P. (2015) 3D Bioprinting Human Chondrocytes with Nanocellulose–Alginate Bioink for Cartilage Tissue Engineering Applications. Biomacromolecules 16(5), pp. 1489–1496.

Matai I., Kaur G., Seyedsalehi A., McClinton A. & Laurencin C.T. (2020) Progress in 3D bioprinting technology for tissue/organ regenerative engineering. Biomaterials 226, p. 119536.

Meakin J.R., Hukins D.W.L., Aspden R.M. & Imrie C.T. (2003) Rheological properties of poly(2-hydroxyethyl methacrylate) (pHEMA) as a function of water content and deformation frequency. Journal of Materials Science: Materials in Medicine 14(9), pp. 783–787.

Midha S., Dalela M., Sybil D., Patra P. & Mohanty S. (2019) Advances in three-dimensional bioprinting of bone: Progress and challenges. Journal of Tissue Engineering and Regenerative Medicine 13(6), pp. 925–945.

Monteiro N., Thrivikraman G., Athirasala A., Tahayeri A., Franca C.M., Ferracane J.L. & Bertassoni L.E. (2018) Photopolymerization of cell-laden gelatin methacryloyl hydrogels using a dental curing light for regenerative dentistry. Dental Materials 34(3), pp. 389–399.

Morgan F.L.C., Moroni L. & Baker M.B. (2020) Dynamic Bioinks to Advance Bioprinting. Advanced Healthcare Materials 9(15), p. 1901798.

Müller M., Öztürk E., Arlov Ø, Gatenholm P. & Zenobi-wong M. (2017) Alginate Sulfate-Nanocellulose Bioinks for Cartilage Bioprinting Applications. Annals of Biomedical Engineering 45(1), pp. 210–223.

Murphy S.V. & Atala A. (2014) 3D bioprinting of tissues and organs. Nature Biotechnology 32, pp. 773–785.

Nguyen D., Hägg D.A., Forsman A., Ekholm J., Nimkingratana P., Brantsing C., Kalogeropoulos T., Zaunz S., Concaro S., Brittberg M., Lindahl A., Gatenholm P., Enejder A. & Simonsson S. (2017) Cartilage Tissue Engineering by the 3D Bioprinting of iPS Cells in a Nanocellulose/Alginate Bioink. Scientific Reports 7(658).

O'Connell C.D., Zhang B., Onofrillo C., Duchi S., Blanchard R., Quigley A., Bourke J., Gambhir S., Kapsa R., Di Bella C., Choong P. & Wallace G.G. (2018) Tailoring the mechanical properties of gelatin methacryloyl hydrogels through manipulation of the photocrosslinking conditions. Soft Matter 14(11), pp. 2142–2151.

Office of the Surgeon General (US) (2004) Bone Health and Osteoporosis: A Report of the Surgeon General. The Frequency of Bone Disease. Rockville (MD): Office of the Surgeon General (US). Available at: https://www.ncbi.nlm.nih.gov/books/NBK45513/ (Accessed: October 18, 2021)

Ojansivu M., Rashad A., Ahlinder A., Massera J., Mishra A., Syverud K., Finne-Wistrand A., Miettinen S. & Mustafa K. (2019) Wood-based nanocellulose and bioactive glass modified gelatin-alginate bioinks for 3D bioprinting of bone cells. Biofabrication 11(3), p. 035010.

Ozbolat I.T., Moncal K.K. & Gudapati H. (2017) Evaluation of bioprinter technologies. Additive Manufacturing 13, pp. 179–200.

Pahoff S., Meinert C., Bas O., Nguyen L., Klein T.J. & Hutmacher D.W. (2019) Effect of gelatin source and photoinitiator type on chondrocyte redifferentiation in gelatin methacryloyl-based tissue-engineered cartilage constructs. Journal of Materials Chemistry B 7(10), pp. 1761–1772.

Parak A., Pradeep P., du Toit L.C., Kumar P., Choonara Y.E. & Pillay V. (2019) Functionalizing bioinks for 3D bioprinting applications. Drug Discovery Today 24(1), pp. 198–205.

Pawlina W. & Ross M.H. (2016) Histology: A Text and Atlas: With Correlated Cell and Molecular Biology. (7th ed.). Wolters Kluwer.

Pockwinse S.M., Rajgopal A., Young D.W., Mujeeb K.A., Nickerson J., Javed A., Redick S., Lian J.B., van Wijnen A.J., Stein J.L., Stein G.S. & Doxsey S.J. (2006) Microtubule-dependent nuclear-cytoplasmic shuttling of Runx2. Journal of Cellular Physiology 206(2), pp. 354–362.

Qu H., Fu H., Han Z. & Sun Y. (2019) Biomaterials for bone tissue engineering scaffolds: a review. RSC Advances 9(45), pp. 26252–26262.

Ramón-Azcón J., Ahadian S., Obregón R., Camci-Unal G., Ostrovidov S., Hosseini V., Kaji H., Ino K., Shiku H., Khademhosseini A. & Matsue T. (2012) Gelatin methacrylate as a promising hydrogel for 3D microscale organization and proliferation of dielectrophoretically patterned cells. Lab on a Chip 12(16), pp. 2959–2969.

Rea S.M., Best S.M. & Bonfield W. (2004) Bioactivity of ceramic-polymer composites with varied composition and surface topography. Journal of Materials Science: Materials in Medicine 15(9), pp. 997–1005.

Rezwan K., Chen Q.Z., Blaker J.J. & Boccaccini A.R. (2006) Biodegradable and bioactive porous polymer/inorganic composite scaffolds for bone tissue engineering. Biomaterials 27(18), pp. 3413–3431.

Ruijtenberg S. & van den Heuvel S. (2016) Coordinating cell proliferation and differentiation: Antagonism between cell cycle regulators and cell type-specific gene expression. Cell Cycle 15(2), pp. 196–212.

Rutkovskiy A., Stensløkken K. & Vaage I.J. (2016) Osteoblast Differentiation at a Glance. Medical Science Monitor Basic Research 22, pp. 95–106.

Ryabenkova Y., Pinnock A., Quadros P.A., Goodchild R.L., Möbus G., Crawford A., Hatton P.V. & Miller C.A. (2017) The relationship between particle morphology and rheological properties in injectable nano-hydroxyapatite bone graft substitutes. Materials Science and Engineering: C 75, pp. 1083–1090.

Saito T., Kimura S., Nishiyama Y. & Isogai A. (2007) Cellulose Nanofibers Prepared by TEMPO-Mediated Oxidation of Native Cellulose. Biomacromolecules 8(8), pp. 2485–2491.

Sawyer S.W., Shridhar S.V., Zhang K., Albrecht L.D., Filip A.B., Horton J.A. & Soman P. (2018) Perfusion directed 3D mineral formation within cell-laden hydrogels. Biofabrication 10(3), p. 035013.

Sheikh Z., Hamdan N., Ikeda Y., Grynpas M., Ganss B. & Glogauer M. (2017) Natural graft tissues and synthetic biomaterials for periodontal and alveolar bone reconstructive applications: a review. Biomaterials Research 21(9).

Stratesteffen H., Kopf M., Kreimendahl F., Blaeser A., Jockenhoevel S. & Fischer H. (2017) GelMA-collagen blends enable drop-on-demand 3D printablility and promote angiogenesis. Biofabrication 9(4), p. 045002.

Tigner T.J., Rajput S., Gaharwar A.K. & Alge D.L. (2020) Comparison of Photo Cross Linkable Gelatin Derivatives and Initiators for Three-Dimensional Extrusion Bioprinting. Biomacromolecules 21(2), pp. 454–463.

Tozzi G., De Mori A., Oliveira A. & Roldo M. (2016) Composite Hydrogels for Bone Regeneration. Materials 9(4), p. 267.

Turnbull G., Clarke J., Picard F., Riches P., Jia L., Han F., Li B. & Shu W. (2018) 3D bioactive composite scaffolds for bone tissue engineering. Bioactive Materials 3(3), pp. 278–314.

Urushibara A., Kodama S. & Yokoya A. (2014) Induction of genetic instability by transfer of a UV-A-irradiated chromosome. Mutation Research/Genetic Toxicology and Environmental Mutagenesis 766, pp. 29–34.

Vijayavenkataraman S., Yan W., Lu W.F., Wang C. & Fuh J.Y.H. (2018) 3D bioprinting of tissues and organs for regenerative medicine. Advanced Drug Delivery Reviews 132, pp. 296–332.

Wang H., Zhou L., Liao J., Tan Y., Ouyang K., Ning C., Ni G. & Tan G. (2014) Cell-laden photocrosslinked GelMA-DexMA copolymer hydrogels with tunable mechanical properties for tissue engineering. Journal of Materials Science - Materials in Medicine 25(9), pp. 2173–2183.

Wang K., Nune K.C. & Misra R.D.K. (2016) The functional response of alginate-gelatin-nanocrystalline cellulose injectable hydrogels toward delivery of cells and bioactive molecules. Acta Biomaterialia 36, pp. 143–151.

Wang X., Lu P., Song Y., Sun Y., Wang Y. & Wang Y. (2016) Nano hydroxyapatite particles promote osteogenesis in a three-dimensional bio-printing construct consisting of alginate/gelatin/hASCs. RSC Advances 6(8), pp. 6832–6842.

Wang X., Tolba E., Schröder H.C., Neufurth M., Feng Q., Diehl-Seifert B. & Müller W.E.G. (2014) Effect of Bioglass on Growth and Biomineralization of SaOS-2 Cells in Hydrogel after 3D Cell Bioprinting. Plos One 9(11), p. e112497.

Warriner A.H., Patkar N.M., Curtis J.R., Delzell E., Gary L., Kilgore M. & Saag K.G. (2011) Which Fractures Are Most Attributable to Osteoporosis? Journal of Clinical Epidemiology 64(1), pp. 46–53.

Wehrle M., Koch F., Zimmermann S., Koltay P., Zengerle R., Stark G.B., Strassburg S. & Finkenzeller G. (2019) Examination of Hydrogels and Mesenchymal Stem Cell Sources for Bioprinting of Artificial Osteogenic Tissues. Cellular and Molecular Bioengineering 12(6), pp. 583–597.

Williams C.G., Malik A.N., Kim T.K., Manson P.N. & Elisseeff J.H. (2005) Variable cytocompatibility of six cell lines with photoinitiators used for polymerizing hydrogels and cell encapsulation. Biomaterials 26(11), pp. 1211–1218.

Wüst S., Godla M.E., Müller R. & Hofmann S. (2014) Tunable hydrogel composite with two-step processing in combination with innovative hardware upgrade for cell-based three-dimensional bioprinting. Acta Biomaterialia 10(2), pp. 630–640.

Yin J., Yan M., Wang Y., Fu J. & Suo H. (2018) 3D Bioprinting of Low-Concentration Cell-Laden Gelatin Methacrylate (GelMA) Bioinks with a Two-Step Cross-linking Strategy. ACS Applied Materials & Interfaces 10(8), pp. 6849–6857.

Zhang B., Gao L., Gu L., Yang H., Luo Y. & Ma L. (2017) High-resolution 3D Bioprinting System for Fabricating Cell-laden Hydrogel Scaffolds with High Cellular Activities. Procedia CIRP 65, pp. 219–224.

Zhang Y.S., Yue K., Aleman J., Mollazadeh-moghaddam K., Bakht S.M., Yang J., Jia W., Dell'erba V., Assawes P., Shin S.R., Dokmeci M.R., Oklu R. & Khademhosseini A. (2017) 3D Bioprinting for Tissue and Organ Fabrication. Annals of Biomedical Engineering 45(1), pp. 148–163.

Zhou X., Castro N.J., Zhu W., Cui H., Aliabouzar M., Sarkar K. & Zhang L.G. (2016) Improved Human Bone Marrow Mesenchymal Stem Cell Osteogenesis in 3D Bioprinted Tissue Scaffolds with Low Intensity Pulsed Ultrasound Stimulation. Scientific Reports 6(1), p. 32876.